NKS-513
ISBN 978-87-7893-613-4

Electric Vehicle Batteries as Components of a Post Nuclear Detonation Radiological Environment (EVNUDET)

Harri Toivonen[1]
Mark Dowdall[2]
Sakari Ihantola[3]
Hannes Vainionpaa[4]
Gísli Jónsson[5]
Pernille Ahlmann Jensen[5]
Mikko Voutilainen[6]
Kari Perajarvi[6]
Henrik Ramebäck[7]

[1]HT Nuclear Oy, 05880 Hyvinkää, Finland
[2]Norwegian Radiation and Nuclear Safety Authority, 1361, Østerås, Norway
[3]Radis Technologies Oy, Finland
[4]Neutrongate Ltd., Sepänkatu 5H, Riihimäki, Finland
[5]Icelandic Radiation safety Authority, 105 Reykjavík, Iceland
[6]Radiation and Nuclear Safety Authority, 01370 Vantaa, Finland
[7]Swedish Defence Research Agency (FOI), 164 90 Stockholm, Sweden

April 2026

Abstract

EVNUDET focused on assessing radiological consequences of neutron activation in modern EV batteries and surrounding materials following a nuclear detonation. The study integrated Geant4 neutron-transport simulations, analytical activation calculations, and targeted irradiation experiments to validate models and quantify activation products, dose rates, and environmental impacts. Simulations assumed a thermal neutron fluence of 10^{12} n/cm². Activation is highly chemistry-dependent: NMC-811 and NCA chemistries produce substantial short-lived gamma-emitting isotopes, notably ^{56}Mn and ^{64}Cu, while long-lived isotopes such as ^{60}Co and ^{59}Fe occur at much lower activities. LFP batteries, lacking cobalt and nickel, generate minimal gamma activation but form ^{32}P, a strong beta emitter and the most significant long-term nuclide for this chemistry. Total induced activity in NMC/NCA packs reaches ~10^{9}–10^{10} Bq, whereas LFP packs are one to two orders of magnitude lower. Dose rates near activated packs are transient and localized: NMC/NCA surfaces may exhibit tens of mSv/h immediately post-exposure, while LFP remains far lower; at one meter, even high-cobalt chemistries typically fall below a few mSv/h. Activation of sodium-bearing soils and pavement dominates the radiation field in post-detonation environments. EV batteries can create localized short-lived gamma radiation fields, increasing exposure near the vehicle, but their overall contribution is minor compared to widespread activation of urban materials. Importantly, outside the vehicle, batteries do not present persistent radiological hazards.

Key words

Neutron activation, nuclear detonation, electric vehicle battery, dose rates

NKS-513
ISBN 978-87-7893-613-4
Electronic report, April 2026

NKS Secretariat
P.O. Box 49
DK - 4000 Roskilde, Denmark
Phone +45 4677 4041
www.nks.org
e-mail nks@nks.org

Electric Vehicle Batteries as Components of a Post Nuclear Detonation Radiological Environment (EVNUDET)

Final Report from the NKS-B EVNUDET activity (Contract: AFT/B(25)6)

Harri Toivonen[1]
Mark Dowdall[2]
Sakari Ihantola[3]
Hannes Vainionpaa[4]
Gísli Jónsson[5], Pernille Ahlmann Jensen[5]
Mikko Voutilainen[6], Kari Perajarvi[6]
Henrik Ramebäck[7]

[1] HT Nuclear Oy, 05880 Hyvinkää, Finland
[2] Norwegian Radiation and Nuclear Safety Authority, 1361, Østerås, Norway
[3] Radis Technologies Oy, Finland
[4] Neutrongate Ltd., Sepänkatu 5H, Riihimäki, Finland
[5] Icelandic Radiation safety Authority, 105 Reykjavík, Iceland
[6] Radiation and Nuclear Safety Authority, 01370 Vantaa, Finland
[7] Swedish Defence Research Agency (FOI), 164 90 Stockholm

Table of contents

Abstract

The EVNUDET study was focused on evaluation of the radiological consequences of neutron activation in modern electric-vehicle (EV) battery systems and selected surrounding environmental materials following a nuclear detonation. As contemporary cities contain large masses of lithium-ion batteries—particularly high-cobalt chemistries such as NMC-811 and NCA—understanding their activation behavior, resulting radiation fields, and relative contribution to post-detonation hazards is a critical gap in existing effects models. The work combined detailed Geant4 neutron-transport simulations, analytical activation calculations, and targeted irradiation experiments to validate modelling approaches and quantify activation products, dose rates, and environmental impacts.

A nominal thermal neutron fluence of 10^{12} n/cm² was used in the simulations. This neutron field does not refer to any nuclear detonation. Fast and epithermal neutrons are not included, and depending on the type of detonation, the neutron fluence can be essentially larger. However, to understand the number of events induced by thermal neutrons is useful to put in perspective the role of the batteries as an auxiliary radiation source. Battery activation results are strongly chemistry-dependent. NMC-811 and NCA produce significant quantities of short-lived gamma-emitting isotopes, particularly ^{56}Mn and ^{64}Cu. Long-lived isotopes such as ^{60}Co and ^{59}Fe occur but they have relatively small activities. LFP batteries generate far less gamma-emitting activation due to their negligible cobalt and nickel content. However, a strong beta emitter ^{32}P is formed, being the most important long-term nuclide of this battery type. Total induced activity in NMC/NCA packs reaches approximately 10^{9}–10^{10} Bq whereas LFP packs are one to two orders of magnitude lower. Dose rates near activated battery packs are transient and localized. Under conservative assumptions, NMC/NCA packs may exhibit surface dose rates of tens of mSv/h immediately after exposure, while LFP packs remain far lower. At one meter, even high-cobalt chemistries typically fall below a few mSv/h. Rapid decay of short-lived isotopes reduces dose rate by one to two orders of magnitude within 24 hours, and long-term radiation dose fields are dominated by small amounts of ^{60}Co.

Activation of urban materials, especially sodium-bearing soils and pavement, is the most dominating source of radiation in a post-detonation situation. Na-24 production in road surfaces generates high dose rates everywhere in the urban environment. EV batteries can produce significant short-lived gamma radiation fields, but their contribution is minor compared to the wide-spread activation of urban materials. However, in the vicinity of the batteries the radiation field is increased and therefore any response team approaching an EV must remain vigilant regarding increased external dose rate and additional hazards posed by damaged batteries, including contamination and potential beta particle emission. Overall, outside the vehicle, the batteries do not create persistent radiological hazards.

1. Introduction

The residual radiation environment after a nuclear detonation (hereafter NUDET) is composed primarily of neutron activated materials in the area within a few km of the detonation and, depending on the nature of the detonation, fission product fallout (hereafter FPF). For detonations that may be described as belonging to Regimes 1, 2 or 3 (fireball not touching ground, see Spriggs, et al. 2020), the former will be the primary source of residual radioactivity (see Appendix 1). For Regimes 4 – 6, the same may be assumed for impacted areas upwind of the detonation where there is little or no deposition of FPF. For either situation, areas outside of the zone where no survivors may be assumed will, in many cases, be amenable to rescue and other operations by emergency services. For the safe operation of such services, an understanding of the radiological environment in which they will be operating is of importance. Formulation of this understanding is, however, complicated by several factors including, but not limited to, those described below.

1. There are no historical analogues which may be employed. Previous works in relation to the nature of the neutron-induced radiological environment after a NUDET have been focused exclusively on Hiroshima and Nagasaki, neither of which represent a modern, urban environment in terms of the composition of the structures and materials present nor the nature of the urban landscape itself. Both factors have an important role to play in estimating the neutron-induced activity present. It should be noted that the primary dose contribution to survivors and first responders in a Regime 1,2 or 3 situation and for sub-areas of the impacted zone for Regimes 4,5 and 6 will be, as evidenced by Hiroshima and Nagasaki, due to neutron-induced activity and considerable uncertainty, has persisted around this contribution for the two concrete examples listed above.

2.The neutron-induced isotopes present are, and their occurrence within materials is, not the same as for FPF deposition. In-situ and field measurement are complicated, and the isotope assemblage can be complex. There is a lack of amenable tools and literature for a priori assessment of possible activation of the environment in the event of a NUDET.

3. The radiological environment due to neutron activation is, in probable contrast to that caused by FPF, likely to be extremely heterogenous both qualitatively and quantitatively with respect to the isotopes present as the materials which may contribute most due to neutron activation are not heterogeneously distributed in an urban landscape.

4. Unlike areas impacted by FPF which may not be physically impacted by the NUDET due to distance from the detonation, areas which are vulnerable to neutron activated contamination are likely to feature extensive physical damage due to blast and heat. As such, such areas will be the primary targets of first responders. An understanding of the radiological environment in which they will be expected to operate will be a key element in post-detonation response.

Discussions as to the neutron activation environment after a nuclear detonation typically tend to focus on Hiroshima and Nagasaki for which limited data exist. Data from nuclear weapons tests conducted by the nuclear weapons states is less available. Attempting to describe the potential residual radiation environment of a modern urban centre, based on data derived from Hiroshima or Nagasaki, is potentially fraught with problems for several reasons but primarily due to the differences between the constituents of a modern urban centre and those of Hiroshima or Nagasaki. The materials, construction techniques, and urban density of modern cities would

most probably lead to significantly different neutron activation patterns relative to either Hiroshima or Nagasaki. Construction materials of Japanese cities of the period typically included concrete with either low levels of steel reinforcement or none, in contrast to modern construction methods employing large amounts of steel reinforced concrete and high-strength concrete. The use the steel and high-strength concrete increases the potential for higher levels of both ^{24}Na and ^{60}Co in the modern urban environment. Steel compositions during the 1940s tended to be simple low carbon steels whereas modern steel formulations may include more Co, Mn and other elements, increasing the potential for isotopes of these elements being present in greater amounts post-detonation, in the modern city. Similarly, glass formations of the modern period differ significantly from the basic soda-lime glass of 1940s Japan with the potential for more ^{32}P being featured in the isotope suite for the modern city. The ubiquity of plastics, asphalt and electronics of all types in the modern city is in direct contrast to Hiroshima and Nagasaki and is accompanied by the potential for a wide number of activation products that may have been of little relevance in 1945.

On a general level, some broad assumptions can be made as to the nature of the neutron-induced environment based on the likelihood of interaction between an incident neutron and a target nucleus (capture cross section). The higher this value for any element, the greater the propensity for nuclei of that element to interact with a neutron and result in a radioactive isotope. Modern urban environments include a wide variety of materials with high cross sections, and which have the potential to constitute radiological hazards upon exposure to neutrons. Many of these materials are present in relatively small, discrete amounts such as in electronics and the radiological hazard posed is likely to be small. Some materials are present in larger amounts and in this regard electric vehicle batteries (hereafter EVBs) are probably the objects of most concern. Batteries for electric vehicles include large amounts (10's kg) of several materials with relatively high cross sections. As of 2022, for the purpose of example, Oslo and its immediate surroundings had approximately 180 000 registered electric vehicles (not including municipal vehicles) and the number of electric vehicles being registered in European cities is growing rapidly with the Nordic countries being clear leaders.

1.1 Electric Vehicle Batteries

Electric vehicle (EV) batteries are composed of many individual cells that store and deliver energy. The battery performance, energy density, manufacturing efficiency, and overall vehicle range is determined mostly by the size and format of these individual cells. While various cell formats are used across different manufacturers, the most adopted sizes are cylindrical 21700 cells and prismatic cells. Among cylindrical cells, the 21700 format (21 mm diameter, 70 mm height) is the most widely used in modern EVs. The 18650 format (18 mm diameter, 65 mm height) was previously dominant in the market but is now being phased out in favor of the 21700, which offers higher energy density and improved thermal management. Cylindrical cells are among the most widely used battery formats in electric vehicles due to their high energy density, reliability, and ease of manufacturing. Prismatic cells are also a common choice, and these cells are typically 148 x 91 x 26 mm, though the dimensions can vary depending on the application. Their rectangular shape allows for more efficient use of space in battery packs. The main advantages of prismatic cells include higher packaging efficiency and improved safety, but they require robust cooling systems to manage heat buildup. Pouch cells are another widely used format and offer a flexible form factor and high energy density but require additional structural support within the battery pack. Their size varies depending on the manufacturer and battery design, with typical dimensions being around 100 mm x 300 mm x 10 mm.

Cylindrical cells used in electric vehicle batteries utilize different lithium-ion chemistries, each offering a balance of energy density, safety, lifespan, and cost. The most common chemistries for 21700 cylindrical cells are known as Nickel Cobalt Aluminum (NCA), Nickel Manganese Cobalt (NMC), and Lithium Iron Phosphate (LFP).

1.2 Nickel Cobalt Aluminum (NCA)

NCA chemistry is widely used in 21700 and 18650 cells, this chemistry providing high energy density and long cycle life, making it ideal for maximizing driving range. However, NCA batteries require advanced battery management systems to ensure thermal stability due to their lower inherent safety compared to other chemistries. The cathode in NCA batteries consists of a layered oxide material made from nickel (Ni), cobalt (Co), aluminum (Al), and lithium (Li). The general chemical formula for the NCA cathode is:

$$LiNi_xCo_yAl_zO_2$$

where:

x (Nickel, ~80-90%) – enhances energy density and capacity
y (Cobalt, ~5-10%) – improves structural stability and electron conductivity
z (Aluminum, ~3-5%) – enhances thermal stability and reduces cobalt dependence

A common NCA composition used in EV batteries is $LiNi_{0.8}Co_{0.15}Al_{0.05}O_2$ (NCA 811), where Nickel (80%) dominates the mix, providing higher energy storage but requiring advanced safety mechanisms.

The anode in NCA batteries is typically made of graphite, sometimes with small additions of silicon to increase energy density. Some newer NCA batteries incorporate silicon (Si) anodes, increasing lithium storage capacity but requiring additional engineering to mitigate expansion-related degradation. For NCA type batteries, the cathode coating thickness is typically in the range 50–100 μm depending on manufacturer and application with anode coating thickness of, typically, 40–90 μm. Since NCA has a high nickel content (~80–90%), its cathode coating is relatively thick to support high energy density. However, it needs a balance between thickness and mechanical stability to avoid cracking. The Nickel Cobalt Aluminum Oxide (NCA) cathode is commonly represented by the formula:

$$LiNi_{0.8}Co_{0.15}Al_{0.05}O_2$$

For this formulation, the molar ratio of Ni, Co and Al is approximately 80:15:5 and the mass percentages of this formulation is Ni 49.9%, Co 9.2%, Al 1.4%, O 33.3% and Li 7.2%. The density of this composition is typically between 4.8 and 5 g/cm^3.

1.3 Nickel Manganese Cobalt (NMC)

NMC cells are common in various EV brands, as they offer a good balance of energy density, power output, and lifespan. This chemistry is used in both 21700 and 18650 formats. NMC batteries typically have different ratios of nickel, manganese, and cobalt (denoted as, e.g., NMC 811, NMC 622) to optimize performance and cost. Nickel Manganese Cobalt oxide (NMC) is

one of the most widely used lithium-ion battery chemistries in electric vehicles and different NMC formulations are available, such as NMC 111, NMC 532, NMC 622, and NMC 811, with varying compositions of nickel (Ni), manganese (Mn), and cobalt (Co) to optimize performance. The cathode in NMC batteries consists of a layered oxide material made from nickel, manganese, cobalt, and lithium. The general chemical formula for the NMC cathode is:

$$LiNi_xMn_yCo_zO_2$$

Different NMC compositions are categorized based on the Ni:Mn:Co ratio:

NMC 111 ($LiNi_{0.3}Mn_{0.3}Co_{0.3}O_2$) – early version with equal parts of Ni, Mn, and Co
NMC 532 ($LiNi_{0.5}Mn_{0.3}Co_{0.2}O_2$) – higher nickel content for improved capacity
NMC 622 ($LiNi_{0.6}Mn_{0.2}Co_{0.2}O_2$) – balances energy density and thermal stability
NMC 811 ($LiNi_{0.8}Mn_{0.1}Co_{0.1}O_2$) – high nickel content for maximum energy density

The trend in NMC chemistry is moving towards higher nickel and lower cobalt content (e.g., NMC 811) to improve energy capacity and reduce reliance on cobalt, which is expensive and ethically problematic. The anode in NMC batteries is typically graphite-based, similar to other lithium-ion chemistries. Some variations use silicon additives to increase capacity. Nickel Manganese Cobalt (NMC) batteries typically have cathode coating thickness of 60–120 µm and anode coating thickness of 40–100 µm depending on manufacturer and application.

The cathode thickness also depends on the NMC ratio (NMC 532, 622, 811). Higher nickel-content NMC (e.g., NMC 811) tends to have thicker coatings to maximize capacity. Nickel Manganese Cobalt (NMC) batteries are typically represented by the formula $LiNi_xMn_\gamma Co_zO_2$, where $x + y + z = 1$. A common variant is NMC 811, which has a composition of $LiNi_{0.8}Mn_{0.1}Co_{0.1}O_2$. The mass percentages for this formulation are Ni 48.2%, Mn 5.7%, Co 6.1%, O 32.9% and Li 7.1%. This material typically has density at room temperature and atmospheric pressure of between 4.5 and 5 g/cm^3.

1.4 Lithium Iron Phosphate (LFP)

LFP chemistry is increasingly popular and unlike NCA and NMC, LFP batteries have lower energy density but offer better thermal stability, longer lifespan, and lower costs. The chemistry is commonly used in prismatic and pouch formats but is now also available in cylindrical 4680 and 21700 cells for enhanced performance and safety. Lithium Iron Phosphate (LFP) batteries are a type of lithium-ion battery known for their high safety, long cycle life, and lower cost compared to Nickel-based chemistries like NMC (Nickel Manganese Cobalt) and NCA (Nickel Cobalt Aluminum). The cathode in LFP batteries consists of lithium iron phosphate, a stable and low-cost material with strong structural integrity. The chemical formula for the LFP cathode is:

$$LiFePO_4$$

LFP cathodes have no cobalt or nickel, making them more environmentally friendly and cost-effective than NMC and NCA cathodes. The iron (Fe) and phosphate (PO_4^{3-}) framework provide strong structural stability, reducing the risk of thermal runaway and improving battery lifespan. Like most lithium-ion batteries, LFP anodes are primarily composed of graphite. Lithium Iron Phosphate (LFP) batteries have typical cathode coating thickness of 80–150 µm

and anode coating thickness of 50–100 μm depending on manufacturer. LFP has lower electrical conductivity than NCA/NMC, requiring a thicker coating to ensure sufficient active material for energy storage. Since LFP cathodes have lower voltage and energy density than NCA/NMC, the anode coating is adjusted accordingly, typically being slightly thicker than in NCA/NMC cells. Lithium Iron Phosphate (LFP) has a relatively simple composition compared to NCA and NMC. The mass percentages of the elements are Li 4.4%, Fe 35.4%, P 19.6% and O 40.5%. Density is typically 3.6 to 3.8 g/cm^3.

For the simulations of the various battery types, the 21700-cell format was chosen due to simplicity in modelling and its being a very common cell format. The three compositions chosen were NCA, NMC 811 and LFP. The following mass abundances and densities were employed (see Table 1).

Chemistry	Nickel (Ni)	Cobalt (Co)	Manganese (Mn)	Lithium (Li)	Iron (Fe)	Phosphorus (P)	Oxygen (O)	Density g/cm^3
NCA	49.9%	9.6%	N/A	7.2%	N/A	N/A	33.3%	5
NMC 811	48.2%	6.1%	5.7%	7.1%	N/A	N/A	32.9%	5
LFP	N/A	N/A	N/A	4.4%	35.4%	19.6%	40.51%	3.8

Table 1. Compositions of the various chemistries employed in EVNUDET.

1.5 Neutron activation of electric vehicle batteries

In consideration of the immediate aftermath of a nuclear detonation, one of the most significant radiological phenomena is the flux of neutrons—both fast and thermal—released during the fission and fusion processes. The energy distribution of the flux varies depending on the type of detonation, distance to the target and its surroundings. Electric vehicle (EV) batteries, because of their material composition may be particularly susceptible to neutron activation which has potential implications for radiological safety of post-detonation rescue and recovery operations and radiological contamination of materials and the environment The primary active material in most EV batteries is lithium, typically in the form of lithium-ion compounds. Natural lithium consists of two stable isotopes: Lithium-6 (^{6}Li) with ~7.5% abundance and ^{7}Li with ~92.5% abundance. The isotope ^{6}Li has a high thermal neutron capture cross-section of ~940 barns and undergoes the following exothermic reaction:

$$^6\mathrm{Li} + n \rightarrow {}^3\mathrm{H} + {}^4\mathrm{He} + 4.78\ \mathrm{MeV}$$

The reaction above produces tritium, ^{3}H, a radioactive beta emitter with a half-life of 12.3 years. Tritium is a low-energy beta emitter, and in the context of EV batteries, tritium can diffuse through electrode and separator materials, potentially escaping into the environment or accumulating in confined battery enclosures. The occurrence of this isotope is of relatively minor radiological significance given its low energy and the probability of it being dispersed relatively rapidly to the atmosphere.

Though less reactive, ^{7}Li can also undergo neutron capture:

$$^7\mathrm{Li} + n \rightarrow {}^8\mathrm{Li}$$

^{8}Li is unstable and decays very rapidly via beta emission with a half-life of 0.84 seconds to form ^{8}Be which also decays very rapidly and as such, the potential impacts of the formation of these two isotopes is very low. Activation of metals may occur as modern EV batteries contain amounts of transition metals with significant neutron activation potential.

	Reaction	Half-life	σ, barn	*p*	Photon emission energy and intensity	Remark
1	^{64}Ni(n,γ)^{65}Ni	2.518 h	1.63	0.00926	1481.8 keV, 23.59 %	39.2 g of Ni per cell Low production rate due to abundance of 0.93%
2	^{55}Mn(n,γ)^{56}Mn	2.579 h	13.36	1	846.8 keV, 98.85 %	4.9 g of Mn per cell
3	^{59}Co(n,γ)^{60}Co	1925.3 d	37.18/2	1	1173.3 keV, 99.85 % 1332.5 keV, 99.98%	4.9 g of Co per cell About equal number of isomers formed initially
	^{59}Co(n,γ)^{60m}Co	10.47 min	37.18/2	1	1332.5 keV, 0.25 %	See Appendix 9 for modelling the time behaviour
	Auxiliary materials					
4	^{63}Cu(n,γ)^{64}Cu	12.70 h	4.50	0.69174	511.0 keV, 35 %	≈ 1.4 to 2.1 g of Cu per cell
5	^{65}Cu(n,γ)^{66}Cu	5.120 min	2.17	0.3083	1039.2 keV, 9.23 %	^{64}Cu decays by β- and β+
6	^{27}Al(n,γ)^{28}Al	2.245 min	0.231	1	1778.9 keV, 100 %	≈ 0.7 to 1.4 g of Al per cell Short half-life
7	^{58}Fe(n,γ)^{59}Fe	44.49 d	1.32	0.0585	1099.2, 56.5 %	Structures outside the battery may be more important
	Other nuclides of interest: environment, concrete, salt, LFP batteries, etc					
8	^{46}Ca(n, γ)^{47}Ca	4.536 d	0.74	0.4E-4	1297.1 keV, 67 %	Decay product ^{47}Sc is a gamma emitter Ca is part of concrete.
9	^{23}Na(n, γ)^{24}Na	14.96 h	0.525	1	1368.6 keV, 99.99 % 2754.0 keV, 99.88 %	Also produced by fast neutrons from Al
10	^{31}P(n, γ)^{32}P	14.27 d	0.166	1	No photon emission	Strong beta emitter, 1.7 MeV max; important in LFP battery, together with item 7

Table 2. Thermal neutron interactions in NCM batteries, σ = thermal neutron cross section, p = abundance of source isotope.

Cobalt-59, the only stable isotope of cobalt, has a neutron capture cross-section of ~37 barns and forms ^{60}Co as follows:

$$^{59}\mathrm{Co} + n \rightarrow {}^{60}\mathrm{Co}$$

Cobalt-60 is a strong gamma emitter (1.17 and 1.33 MeV) with a half-life of 5.27 years.

The formation of the metastable isomer ^{60m}Co is potentially a significant aspect of neutron activation in cobalt-containing materials. Cobalt-60m, an excited state of the same nucleus with a different energy level and half-life, it is produced via neutron capture on stable ^{59}Co:

$$^{59}\mathrm{Co} + n \rightarrow {}^{60m}\mathrm{Co} \rightarrow {}^{60}\mathrm{Co} + \gamma$$

This reaction can proceed directly to the metastable state ^{60m}Co or to the ground state ^{60}Co, depending on the energy of the incident neutron and the nuclear reaction pathway. Cobalt-60m has a half-life of approximately 10.5 minutes and decays via isomeric transition (IT) to the ground state of ^{60}Co, emitting gamma radiation in the process (see Appendix 9).

Nickel-58 can capture neutrons to form ^{59}Ni, a long-lived beta plus emitter (half-life ~76,000 years). However, it does not cause any significant radiation hazard due to its long half-life. A beta minus emitter ^{65}Ni, emitting gamma radiation, is formed in reaction ^{64}Ni(n, γ)^{65}Ni.

Manganese-55 can form ^{56}Mn, which decays with a half-life of 2.6 hours and emitting both beta and gamma radiation. Both these isotopes contribute to both short-term radiation exposures in the vicinity of the battery and long-term contamination, particularly in densely packed battery modules. EV batteries also include significant amounts of structural metals (aluminum, copper, steel) and electronic components (semiconductors, circuit boards) that are also susceptible to neutron activation. Aluminium-27 captures neutrons to form ^{28}Al, a beta emitter with a half-life of 2.24 minutes. Copper-63 can form ^{64}Cu, which decays via both beta-minus and beta-plus emission. Table 2 is a summary of the basic nuclear reactions and related critical information of NCM batteries irradiated in a thermal neutron flux (IAEA data base, Isotope Browser). While many of these isotopes are short-lived, they can potentially produce radiation fields that may pose exposure risks during emergency response or to survivors. Depending on the composition of the battery which has been irradiated, there is the potential for these radiation fields to persist over days and in the worst instances, a week.

2 Methodology

All simulations were conducted using Geant4 (Agostinelli et al., 2003) and the SWORD7 interface (Duvall, 2019) using reference physics lists. The QGSP_BIC_HP reference physics list was the standard physics package used. QGSP (Quark-Gluon String Precompound) applies to protons and neutrons with energies from 0 to 10 GeV. The HP (High Precision) neutron data is valid from 0 – 20 MeV and applies only to neutrons, superseding the BIC model, and handling elastic, inelastic, capture and fission interactions of neutrons and isotopes. Material compositions and physical data where relevant were drawn from Detwiler et al. (2021).

2.1 Cell and battery geometry

The chosen cell type, 21700, consists of a cylinder of 21 mm diameter and 70 mm height. The outer casings of such cells are typically constructed from steel or aluminum and are typically 0.22 – 0.34 mm thick being slightly thicker on the base. Anodes in such cells are typically graphite based with the cathode being comprised of the relevant material for the specific battery type. These coatings mounted on foils which are then rolled to form the cylindrical cell. For the purpose of this work two cell models were devised. The first cell model was intended to represent a conventional cell construction and used data derived from Quinn et al. (2018), Ank et al. (2024) and Kovachev et al. (2019). This model consisted of an outer aluminum can of 0.25 mm lined with a polyethylene layer of 0.2 mm. This was then followed by a series of concentric layers of the cathode foil support (Al, 0.015 mm), the cathode active layer (battery chemistry material, 0.135 mm), a separatory foil (polyethylene, 0.02 mm), the anode foil support (Cu, 0.01 mm), the anode active layer (porous graphite, 0.08 mm) followed by a separatory foil (polyethylene, 0.02 mm). This sequence was repeated until a final air volume with a radius of 0.00955 mm was reached. Base plates and upper caps were not included. Electrolytic gels or liquids were omitted. The second cell model consisted of the same aluminum external can and inner air volume but the volume between was filled with a homogenous material. This material was comprised of the same masses of each element contained in the cathode and anode foils and active layers of the first representation in addition to the separatory layers and can liner. In this manner both geometries contained the same number of atoms of each element for the volume between the external can and inner air volume.
Table 3. Number of atoms produced for comparison of Type 1 and Type 2 cell geometries in identical thermal neutron fluxes.

Isotope	Type 2	Type 1	Ratio
^{28}Al	89	84	1.06
^{8}Be	14	15	0.933
^{60}Co	1681	1456	1.155
^{64}Cu	249	236	1.055
^{66}Cu	48	53	0.906
^{56}F	553	552	1.002
^{56}Mn	553	552	1.002
^{60}Ni	1681	1456	1.155
^{28}Si	89	84	1.06
^{66}Zn	48	53	0.906

Table 3. Comparison of Type 1 and Type 2 cell geometries in terms of induced activity on exposure to identical neutron fluxes.

Elements used in both geometries were described using relevant isotopic compositions. For this study, the concentric layer geometry was designated Type 1 and the homogenous geometry as Type 2 (see Figure 1). The two geometries were tested for equivalency using flat 10 x 10 arrays of each geometry type using each of three chemistries. These arrays were exposed to simulated neutron beams (100 n/cm^2) incident normal to the top surface of the area and at a 45^o incident angle. The number of atoms generated in each array was then compared (see Table 3). Due to the significantly increased computational overhead experienced in using the Type 1 geometry and the good agreement between the two in terms of the response to incident neutrons, the Type 2 geometry was selected as the base unit for further work.

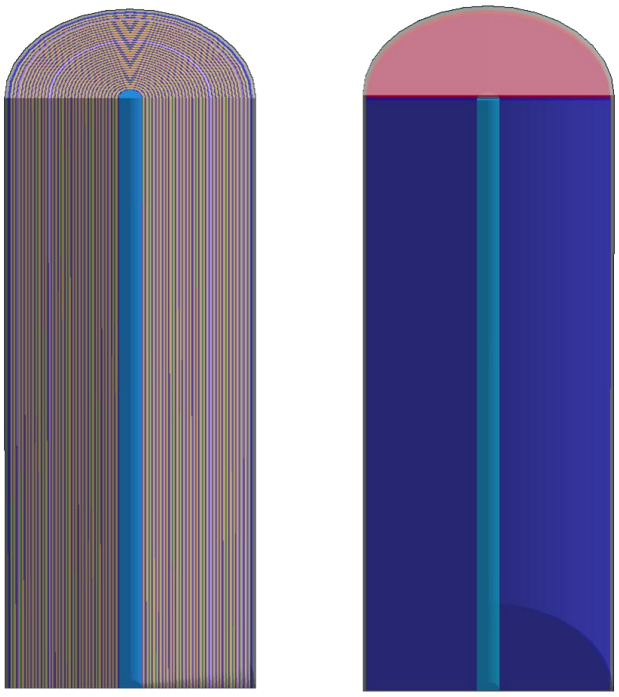

Figure 1. Schematics of Type 1 (left) and Type 2 (right) cell geometries.

The Type 2 geometry for a single cell was used to construct an array of 50 x 80 individual cells arranged without offsets between cells on any dimension. This array was then used in all subsequent simulations and analyses. Ancillary structures (casings, cooling, electrical etc.) typically found in production EV battery systems were not included. EV batteries may be present in a variety of configurations, but the single layer flat arrangement was selected as a useful, easy to handle simulation model (see Figure 2).

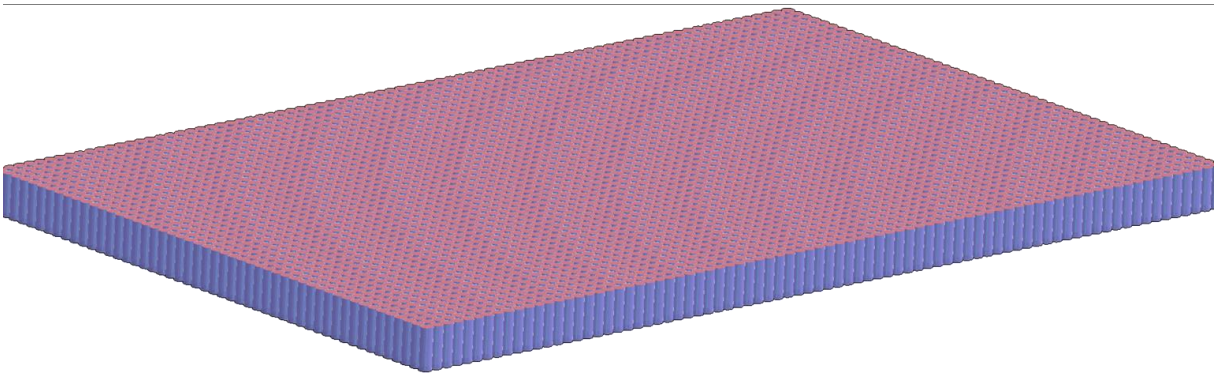

Figure 2. Schematic of the 50 x 80 battery pack geometry.

2.2 Simple Estimation of Induced Activities and Related Problems

For the estimation of the amount of an isotope that may be generated in an element due to irradiation with neutrons, the following parameters are needed:

- The mass of the target element (m) in grams
- The neutron energy (En) as either eV or MeV which determines cross-section
- The neutron fluence (Φ) in n/cm² or an integrated flux over time $\Phi=\phi \cdot t$, where ϕ is the neutron flux in n/cm²/s and t is the irradiation time in seconds
- The isotopic composition of the material being exposed
- The cross-section (σ) for the reaction at neutron energy En in barns 10^{-24} cm²
- The half-life ($t_{1/2}$) of the product isotope in seconds.

In this calculation, the number of nuclei in the target, N_T is determined using:

$$N_T = (m \cdot N_A)/A$$

where N_A is Avogadros number and A is the molar mass (g/mol).

The reaction is then chosen and the relevant cross section, σ, chosen from appropriate nuclear data sources. The rate of the reaction can then be determined using:

$$R = \phi \cdot \sigma \cdot N_T$$

The maximum activity attained can be determined by using:

$$A_{\max} = R \cdot (1 - e^{-\lambda t})$$

where λ is the decay constant and t is the time for irradiation is seconds.

The activity at a certain time after irradiation ceases can be determined by:

$$A = A_{\max} \cdot e^{-\lambda t(\mathrm{p})}$$

where *t(p)* is the time in seconds after exposure to the neutrons ceases.

These calculations can be modified to include targeted materials where many isotopes are involved (in which case the activities are simply summed) and for threshold reactions where only neutrons exceeding a certain energy will be included.

These types of calculations are often featured in various types of calculators and simple tools but are vulnerable to a number of problems in dealing with practical examples. In particular, the area exposed or the thickness of the samples being irradiated do not feature in the calculation primarily because neutron fluences are treated as surface quantities in which there is an implicit assumption that there is unform exposure of the samples front (or any) surface. As fluence is area independent, typical calculations utilize :

$$\Phi = \phi \cdot t$$

which is normalized per unit area and the total number of reactions with the neutron's scales with the number of nuclei exposed to the neutrons. In this way the mass of the sample is already

accounted for in the calculation and therefore volume. Calculations of these type however assume full penetration of the sample by the neutrons with no significant attenuation of the neutrons with depth. It is obviously therefore a problem if the sample is thick enough to attenuate neutrons to any significant degree. If that is the case, it would then be necessary to account for variations of the fluence with depth in the sample. Thickness can only be ignored when the samples are either very thin or very small, where the sample materials are low atomic number materials and where the energy of the neutrons is very high.

The use of the simple mathematical expressions as outlined in this section for estimation of activation due to neutron fluxes is only moderately adequate in terms of accuracy due to the range of assumptions necessary. Such calculations are acceptable in situations of low complexity – one dimensional homogenous material with limited physics processes considered and where energy resolution of the incident neutrons is approximate. For real world applications involving relatively complex geometries and materials and where more is required than a simple estimate, Monte Carlo applications offer significant benefits, the downside being the extensive computational requirements.

3 Analytical functions compared with Geant4

Results of calculations using functions of the type as described in Section 2 are compared with Geant4 simulations in Figure 3. The results are very similar to each other in all cases (Li, Co, Mn, Cu), with, taking cobalt as an example, the ratio of atoms formed being 1.04 (foil of 0.5 mm) for the two methods.

Another means to compare the two approaches is to utilize neutron reactions in Co and Li.

		Cobalt	Lithium
Atomic weight	A	58.933	6.941
Abundance (%)	y	100	7.59
Cross-section (barn)	σ	37.18	940
Density (g/cm^3)	ρ	8.834	0.534

Table 4. Nuclear data for cobalt and lithium

The ratio of ^{60}Co atoms to ^{3}H atoms formed in thermal neutron flux per unit mass is 0.0613.

This means that in a battery, the neutron reactions in lithium dominate over cobalt and other atoms. However, if the comparison is made per unit volume, then the ratio is 1.015. Therefore, in Geant4 simulations with targets of equal dimensions – foils and cubes – it can be expected to produce about the same number of ^{60}Co and ^{3}H events (Figure 3). It is also interesting to observe that in a small target of 1 cm^3 almost all thermal neutrons hitting the Li or Co target will result in a nuclear reaction.

Irradiation of cobalt produces ^{60m}Co and ^{60}Co atoms and the former constitutes a very useful measurement parameter. Due to the short half-life of 10.47 min, initially ^{60m}Co emits many more photons than ^{60}Co with a half-life of 5.27 y. Manganese is another useful material for neutron studies such as these with a high cross section and high-energy photons (1810 keV,

yield 26.9 %) which are useful from measurement point of view (due to low attenuation in volumetric samples). Copper may also be useful to characterize the neutron flux from a neutron generator, the Cu curve in Figure 3 being a straight line which means that a 1 mm foil with an area of 1 cm^2 and a cube of 1 cm^3 should give ^{64}Cu atoms in a ratio of 1:10. The deviation of the photon counts from the ratio of 0.1 refers to the attenuation in the cube and to a different geometry (important when the source is near detector). This ratio is useful to check the efficiency of the counting system.

The (n, γ) reaction in ^{63}Cu yields ^{64}Cu which decays by β+ resulting in two 511 keV photons (yield 35.04 %, half-life12.7 h). Coincidence counting would give the activity without any efficiency calibration. The challenge however may be the low activity of the samples.

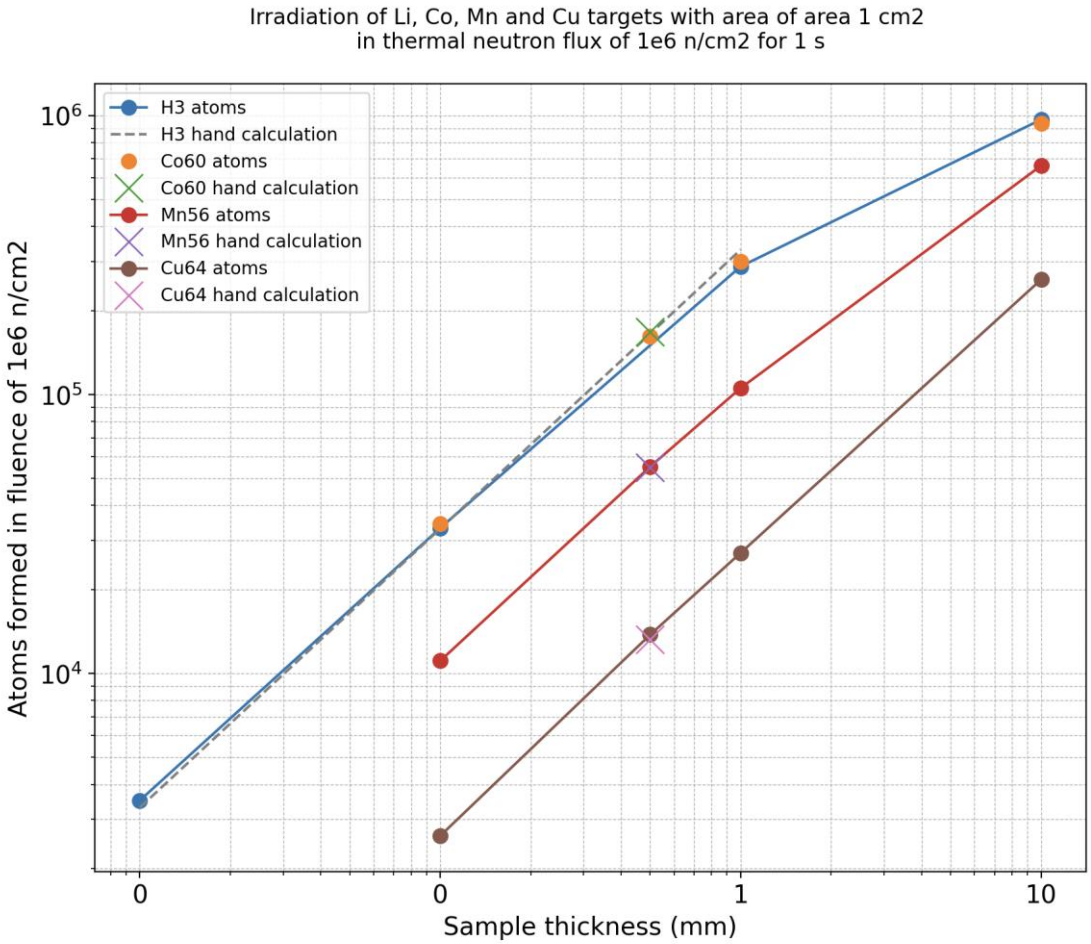

Figure 3. Simulation of irradiation of target atoms in thermal neutron flux.

3.1 Distribution of neutron absorption events in small cubic volumes of Co, Mn and Cu

When a beam of neutrons penetrates a thin sample, the flux is attenuated exponentially. For a volumetric sample the situation is slightly different, because the scattered neutrons can also result in neutron absorption events. Nevertheless, the mean free path is the key variable to estimate the attenuation of a neutron beam in material. In Co, Mn, and Cu the mean free paths of thermal neutrons are 0.30 cm, 0.91 cm and 3.11 cm, respectively. Therefore, in a cube of 1 cm^3 the neutron interactions take place near the surface upon which the neutrons are incident

for cobalt whereas in copper the neutron interactions take place uniformly all over the cube. The following is a quantitative appraisal of these phenomena. Cobalt, manganese and copper cubes with a volume of 1cm^3 were irradiated in a simulated thermal neutron flux. Figures 4, 5 and 6 show the distribution of atoms formed as a result of 1000 neutron absorption events. As expected, the Co events take place near the incident surface whereas Mn and Cu events are more evenly distributed throughout the volume. If such cubes are surrounded by polyethylene (PE), the distribution of atoms produced by neutrons is more even. Figure 7 shows the case for a Co cube surrounded with 3 cm PE. In front of the target, the PE functions as a radiation shield scattering neutrons out from the beam. The other parts of the PE increase neutron-induced events inside the cube making the interaction distribution more even.

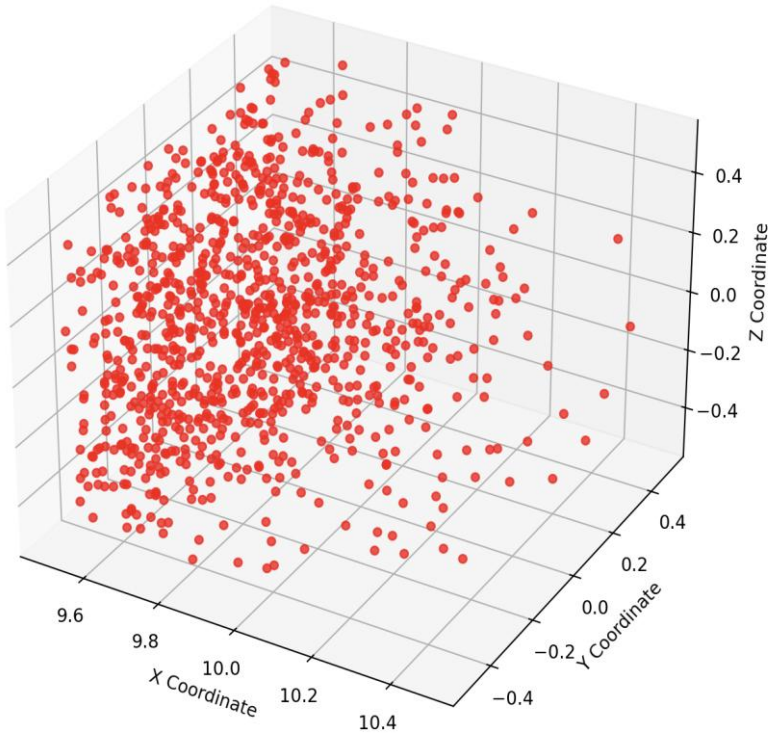

Figure 4. Distribution of 1000 ^{60}Co atoms in a 1 cm^3 cobalt cube when irradiated in a thermal neutron beam incident from the x direction.

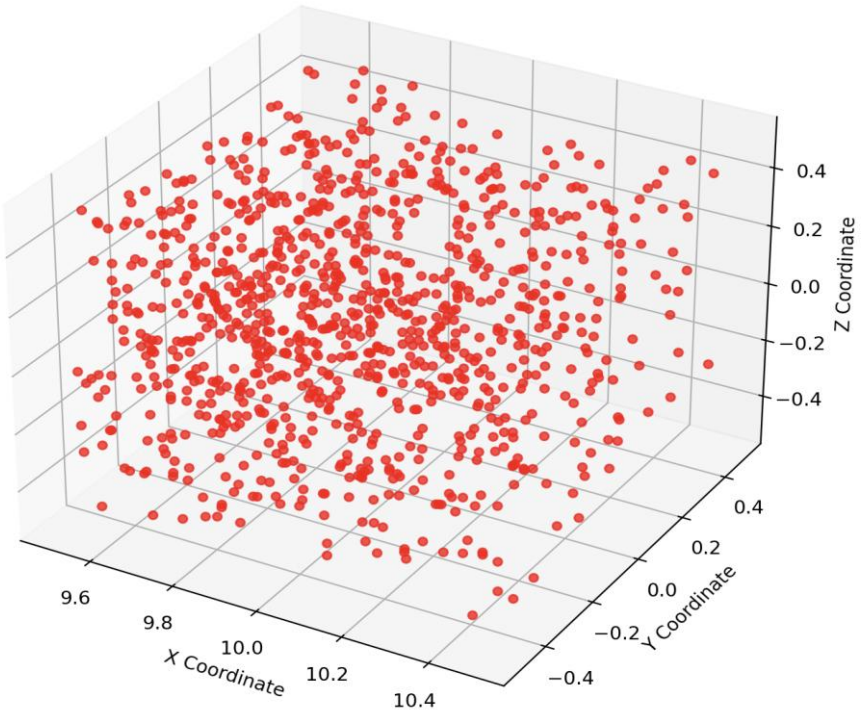

Figure 5. Distribution of 1000 ^{56}Mn atoms in a 1 cm^3 manganese cube when irradiated in a thermal neutron beam incident from the x direction.

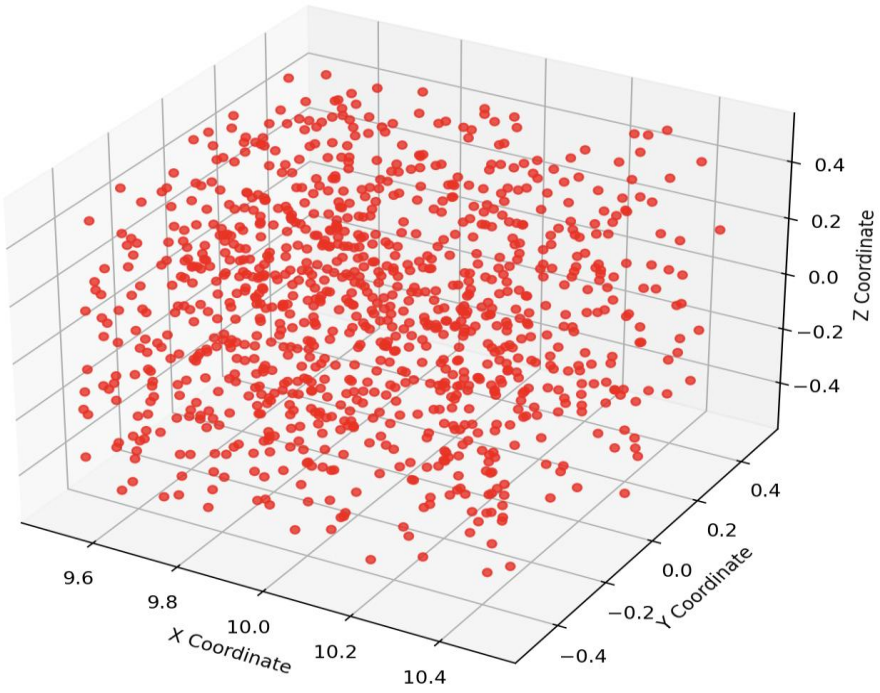

Figure 6. Distribution of 1000 ^{64}Cu atoms in a 1 cm^3 copper cube when irradiated in a thermal neutron beam incident from the x direction.

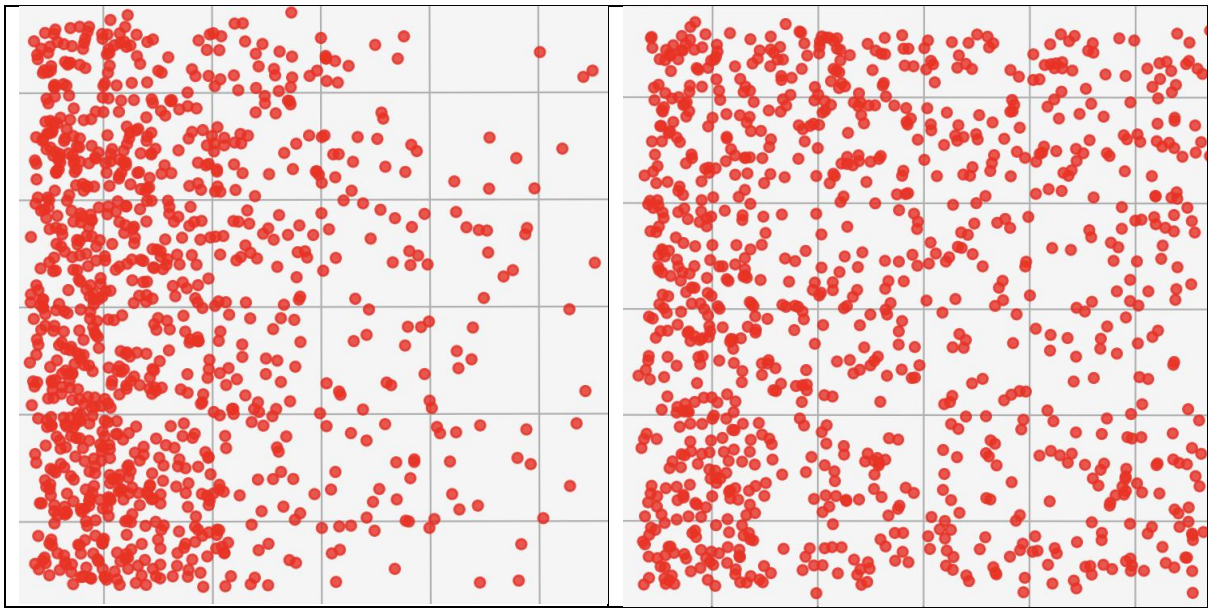

Figure 7. Top view of distribution of 1000 ^{60}Co atoms in a 1 cm^3 cube when irradiated in a thermal neutron beam incident from the x direction. (Left) bare cube, (Right) cube surrounded with 3 cm PE.

4 Geant4 compared with empirical data

Work was conducted to compare Geant4 results with a neutron activation analysis method for measuring thermal neutron flux using indium monitor foils and sample activation. The experimental setup consisted of a NeutronGate *nJenni* pumped neutron generator, in which deuterium ions are accelerated onto an aluminum target, producing neutrons via the d(d,n)^{3}He fusion reaction with a nominal energy of approximately 2.5 MeV. The irradiation configuration is shown in Fig. 8a. The neutron beam was thermalized by placing 60 mm of mineral oil between the neutron source and the sample. In addition, the sample was surrounded by moderating material to ensure efficient neutron slowing and to provide a nearly isotropic thermal neutron field at the sample location. An indium monitor foil was used to measure the thermal neutron flux and was positioned at the same location as the sample by taping it at the interface between two PETG disks within the sample holder, see Fig. 8b. After irradiation, the sample was transferred to the counting configuration shown in Fig. 8a (bottom). During counting, a 2 mm thick PETG layer separated the sample and indium foil from the HPGe detector endcap. The transfer from the irradiation position to the detector was performed by directly placing the same sample holder over the detector endcap, requiring approximately 5–10 seconds. This rapid transfer allowed the measurement of radionuclides with relatively short half-lives without the need for a pneumatic rabbit system and replication of the same counting geometry for all measurements. The experimental setup consisted of 10×10×10 mm³ sample cubes mounted on 3D-printed holders for consistent positioning during irradiation and counting phases (see Figure 8). Neutron flux was determined through the ^{115}In *(n,γ)* ^{116m1}In reaction, monitoring the 1097 keV gamma peak, while sample activation was measured using the ^{59}Co *(n,γ)* ^{60m1}Co reaction at 1332.49 keV. High-purity germanium (HPGe) detector efficiency was

calibrated using ^{152}Eu sources and validated through Monte Carlo simulations. The measured thermal neutron flux was estimated at 3.28×10^4 n/(s·cm²). Key uncertainty sources included neutron energy spectrum assumptions, detector efficiency calibration discrepancies, and neutron generator performance limitations. -The sample holder was made from 3D-printed PETG material ensuring reproducible positioning, the monitor foils being $10\times25.4\times0.0051$ mm³ indium foils positioned alongside the sample cube and the sample materials were cobalt, aluminum and copper $10\times10\times10$ mm³ cubes.

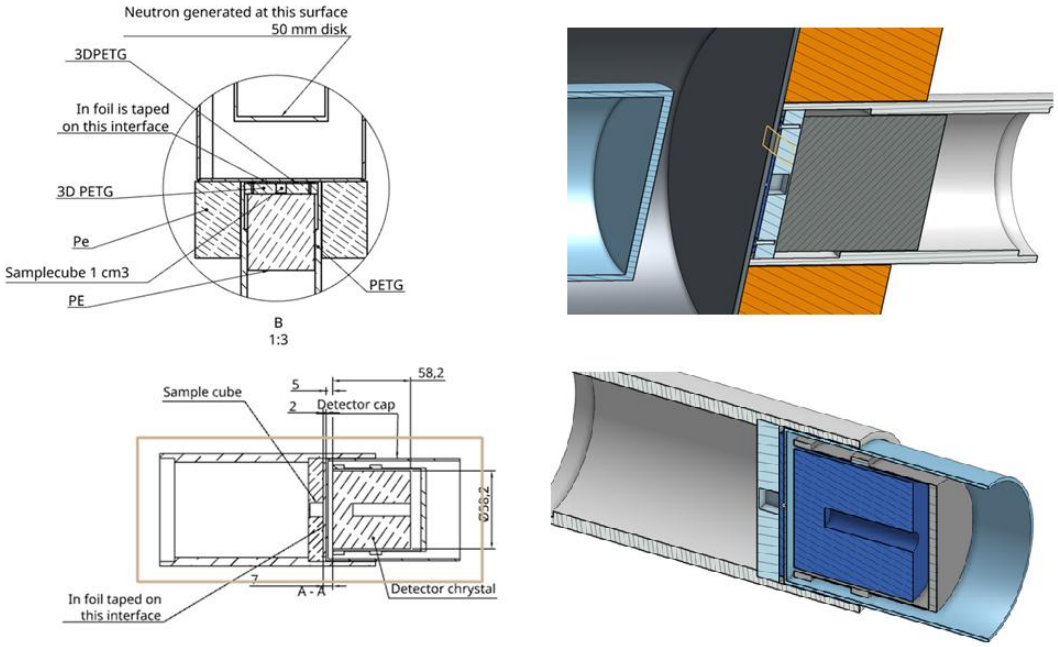

Figure 8a. Top: irradiation geometry. The sample and indium foil are surrounded by moderator material, providing a relatively uniform thermal neutron flux from all directions. Bottom: counting configuration. There is an approximate 7 mm gap between the HPGe detector crystal and the front face of the sample.

Figure 8b. Sample holder and positioning of indium foil.

The irradiation geometry consisted of the sample cube and indium foil mounted on the same holder with an 80 mm polyethylene moderator surrounding and behind the sample and continuous neutron beam irradiation. Between the neutron source and sample there was 60 mm of mineral oil that acting as the main moderator and the transfer time from irradiation to counting: 20-60 seconds.

The thermal neutron flux was determined using the indium activation via the ^{115}In *(n,γ)* ^{116m1}In reaction. The 1097 keV peak was chosen for thermal neutron flux monitoring. Indium has a number of activation peaks; note that the In peak at 1293 keV has a competing activation route with a 14 s half-life. For that reason, the 1097 keV peak was used. Indium also has a peak at 336 keV that can be used to measure neutrons with energies >500 keV.

The following constants are used for all measurements:

- Indium foil mass: $m_{foil} = 9.42 \times 10^{-2}$ g
- Indium molar mass: $M_{In} = 1.14 \times 10^{2}$ g/mol
- Avogadro's number: $N_A = 6.022 \times 10^{23}$ mol^{-1}
- In-115 abundance: $Ab_{In115} = 95.71\%$
- In-116m1 half-life: $T_{h,In} = 3260$ s
- Indium peak energy: $E_{In} = 1097.00$ keV
- 1097 keV peak intensity: $I_{In1097} = 58.5\%$

- Thermal capture cross-section: $\sigma_{In116m1} = 149 \times 10^{-24}\ \mathrm{cm}^2$

The number of ^{115}In atoms in the monitor foil was calculated as:

$$N_{In115} = \frac{m_{foil}}{M_{In}} \times N_A \times Ab_{In115}$$

$$N_{In115} = \frac{9.42 \times 10^{-2}}{1.14 \times 10^{2}} \times 6.022 \times 10^{23} \times 0.9571 = 1.60 \times 10^{20}\ \mathrm{atoms}$$

The ^{116m1}In decay constant is:

$$\lambda_{In} = \frac{\ln(2)}{T_{h,In}} = \frac{\ln(2)}{3260} = 2.12 \times 10^{-4}\ \mathrm{s}^{-1}$$

Number of ^{116m1}In decays counted during measurement time T_c**:**

$$dN_{In116m1} = \frac{A_{In}}{Ef_{foil}(1097) \times I_{In1097} \times (1 - Dt)}$$

where:

- A_{In} = measured peak area at 1097 keV
- Dt = dead time correction factor
- Ef_{foil} = detector efficiency at 1097 keV

The number of ^{116m1}In atoms at the start of counting:

$$N_{In116m1} = \frac{dN_{In116m1}}{1 - e^{-\lambda_{In} \times T_c}}$$

Thermal neutron flux calculation:

$$F_t = \frac{\lambda_{In} \times N_{In116m1}}{N_{In115} \times \sigma_{In116m1} \times (1 - e^{-\lambda_{In} \times T_{irr}}) \times e^{-\lambda_{In} \times T_w}}$$

where:

- T_{irr} = irradiation time
- T_w = waiting time between end of irradiation and start of counting

For sample activation via thermal neutrons, the sample-specific decay constant is calculated:

$$\lambda_s = \frac{\ln(2)}{T_{h,s}}$$

where $T_{h,s}$ is the half-life of the activated sample isotope.

The energy dependent detector efficiency for the sample cube geometry is calculated as:

$$Ef_{cube}(E_s) = 27.58 \times E_s^{-1.173}$$

where E_s is the sample peak energy in keV.

The number of sample decays counted during measurement time is yielded by:

$$dN_{sample} = \frac{A_s}{Ef_{cube}(E_s) \times I_s \times (1 - Dt)}$$

where:

- A_s = measured sample peak area
- I_s = gamma-ray intensity per decay for the sample peak

The activity at the end of irradiation is provided by:

$$Ac_{sample} = \frac{\lambda_s \times dN_{sample}}{(e^{-\lambda_s \times T_c} - 1) \times e^{-\lambda_s \times T_w}}$$

The activation setup was modelled in Geant4 as depicted in Figure 9. The neutron beam of 2.4 MeV was modelled as a uniform beam shooting down from the lower surface of the beam plate into the bath of mineral oil. The sample holder, sample and the position and size of the indium foil were as described earlier.

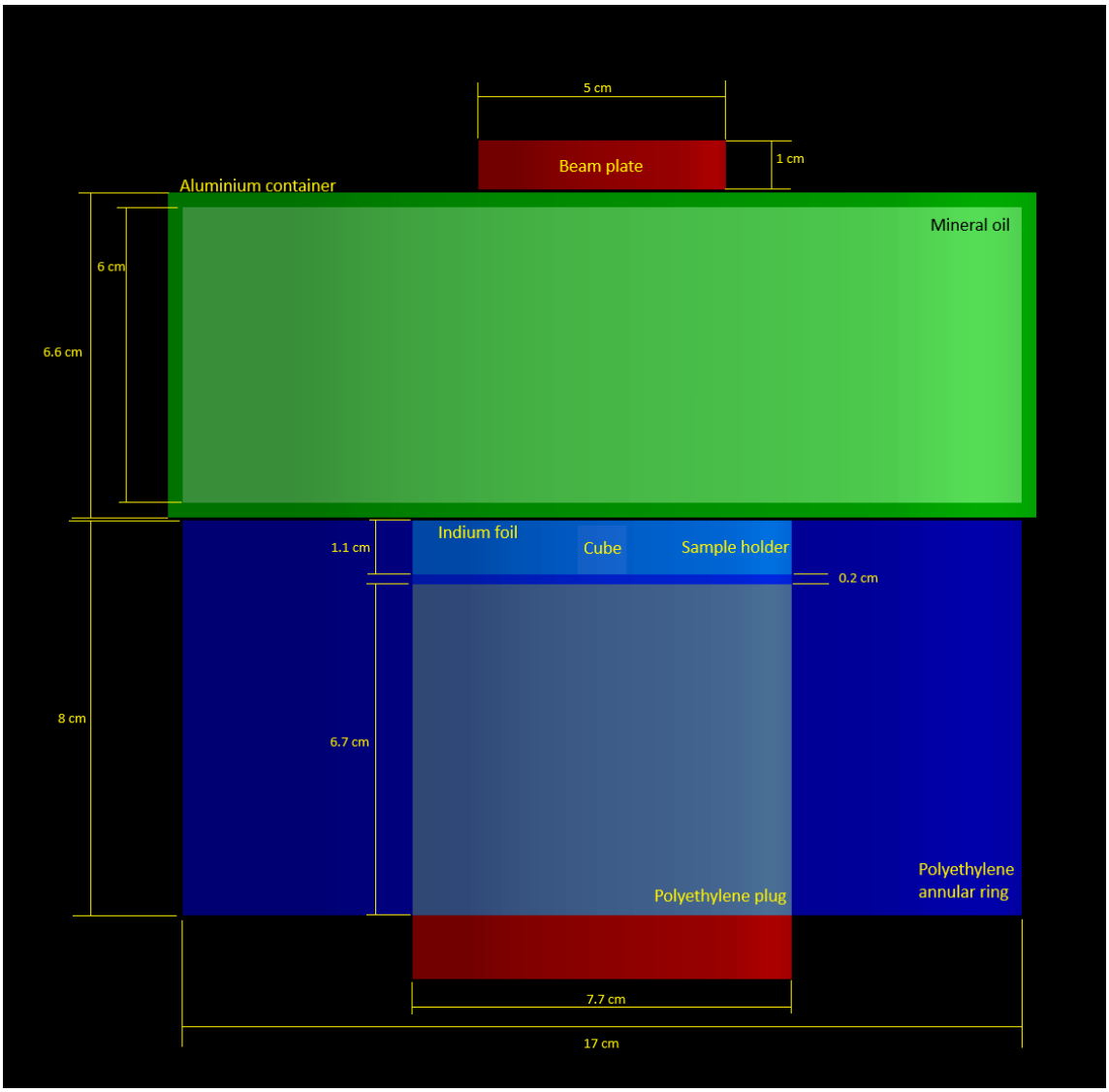

Figure 9. Geant4 geometry model of the sample activation setup.

Activities generated within the foil and the sample cube were calculated from output data as described earlier. Activities were also estimated using the analytical functions as detailed earlier in the report.

Atom ratio	Experiment	Geant4	Analytical function*
^{60m} Co/^{116m} In	20.6	9.21	22.1
^{66}Cu/^{116m} In	0.447	0.785	0.732
^{28}Al/^{116m} In	0.0948	0.203	0.183

(*) assuming constant neutron flux all over the target (no attenuation)

Table 5. Comparison of atom ratios for samples cubes for experimental data, Geant4 simulations and analytical functions.

The experimental results and simulations with Geant4 differ by a factor of approximately 2 for the three sample cubes (see Table 5). For Cu and Al, the Geant4 and analytical function results differ by less than 10 %. This is largely expected as the neutron flux is almost constant within the cubes. For Co, the Geant4 simulation gives essentially smaller production of ^{60m}Co atoms (by a factor of 2.4) as compared with analytical functions. The reason for this observation is the attenuation of the neutron flux inside the cube.

5 Dose rate calculations

For estimation of dose rates due to activation isotopes in the battery packs post-irradiation, two geometries were employed. As it would be impractical to distribute the isotopes within the battery pack geometry in a manner in accordance with the precise locations as indicated by the activation simulation, two "extreme" cases formed the basis of these geometries. In both geometries, the battery pack was considered as a monolithic form of the battery pack with the same dimensions and composed of the relevant chemistry material: NCM811, NCA and LFP. In the first case, irradiation was assumed to have induced all the activity within the outermost 1 cm layer of 5 sides of the geometry (the side that would be facing the ground was omitted). This was designated as Case 1. The second geometry, Case 2, considered the battery pack as a unform mass of the material with the induced activity dispersed homogeneously within that mass. In this way, two extreme cases were represented – Case 1 representing potentially the highest dose rate, and Case 2 the lowest.

To estimate the dose rate, a 1 kg spherical mass of a tissue equivalent plastic material (see Table 6) was positioned either centrally above the largest surface of the Case 1 and Case 2 geometries or at 1 m distance from this surface.

Element	Carbon (C)	Chlorine(Cl)	Hydrogen (H)	Magnesium (Mg)	Nitrogen (N)	Oxygen (O)
Mass fraction	0.583	0.0009	0.0812	0.1303	0.0178	0.186

Table 6. Mass fraction composition of tissue equivalent plastic.

The first instance being indicative of a person sitting in the vehicle and the second being indicative of a person standing in the vicinity of the vehicle. 1 MBq of each isotope (depending on the chemistry involved) was then distributed either within the outermost 1 cm layer of the battery mass (Case 1) or homogenously in the entire battery mass (Case 2). The energy deposited in the 1 kg mass of material was then tallied and this served as a dose conversion coefficient for the geometry. Dose rates were then determined for the total activities determined to be induced in the battery packs for both Cases.

Dose rate contributions were divided into two components – those derived from direct gamma emissions from the isotopes in question and those derived from Bremsstrahlung arising from the presence of beta emitting isotopes in the battery packs (see Appendices 6,7,8). Dose conversion coefficients were derived separately for each contribution. Total dose rates were the sum of the two components. Isotopes for which either contribution would be negligible were omitted.

6 Results

6.1 Activities Induced in Battery Packs

Estimates of activities induced in the 50 x 80 array by 0.025 eV neutrons were derived using incident beams of 100 n/cm^2 and extrapolation to the higher flux for which results are reported in Figs. 10, 11 and 12. Full tabulated data are found in Appendix 3.

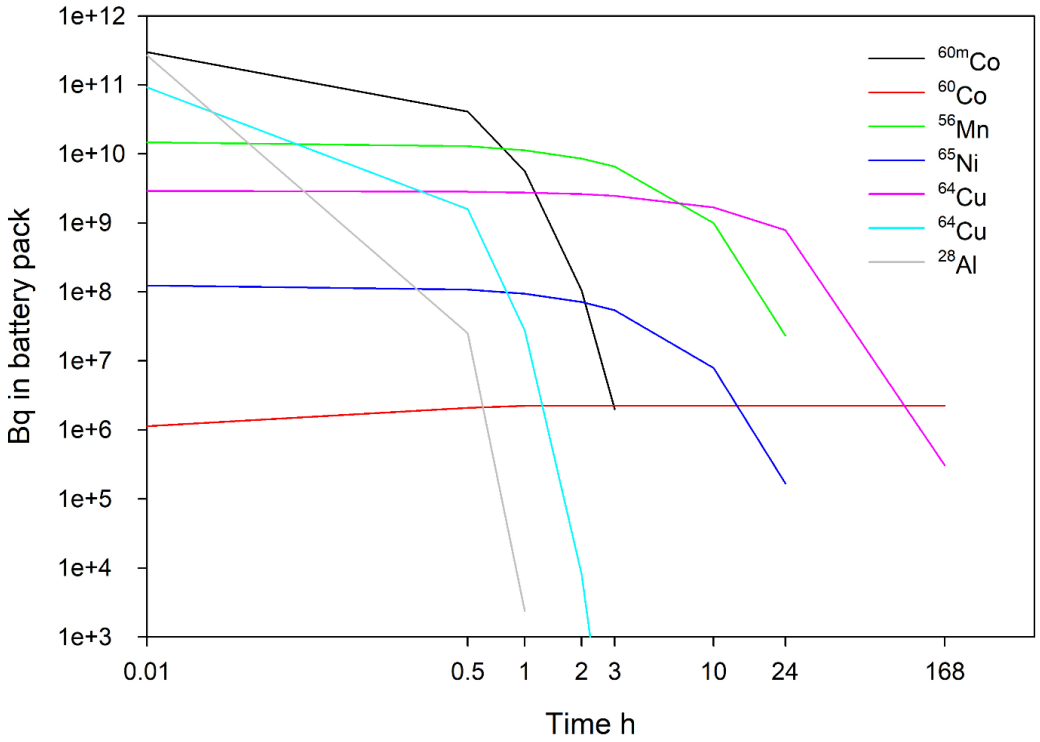

Figure 10. Activities induced in a 4000 cell array composed of NCM811 cells for an incident flux of 1x10^{12} n/cm^2.

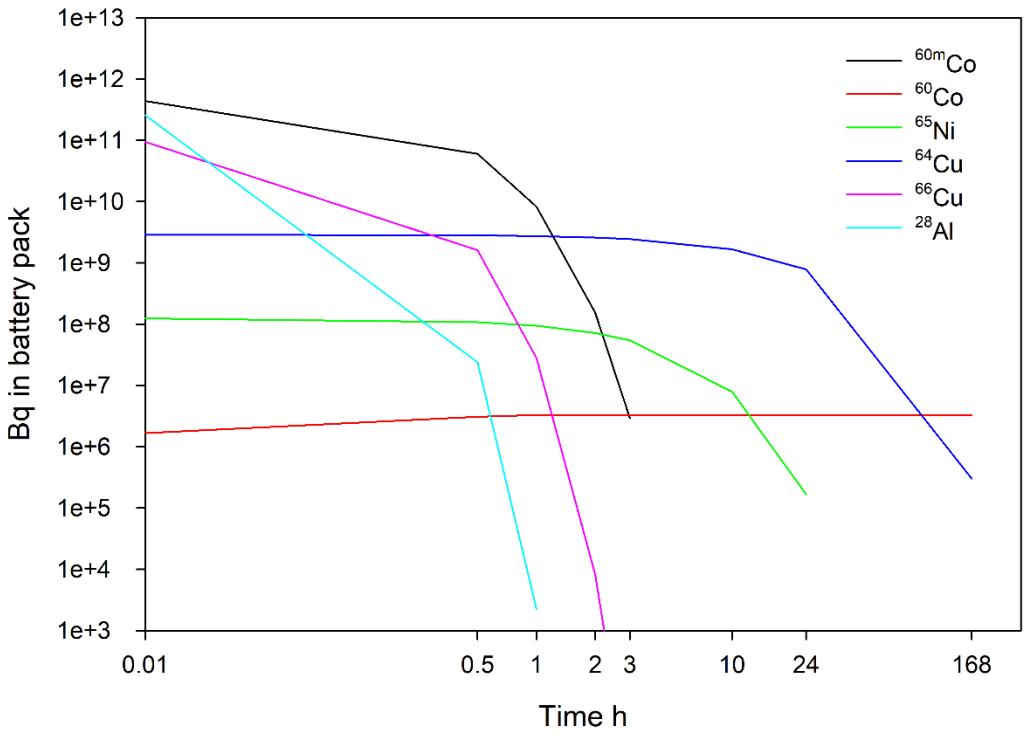

Figure 11. Activities induced in a 4000 cell array composed of NCA cells for an incident flux of $1x10^{12}$ n/cm^2.

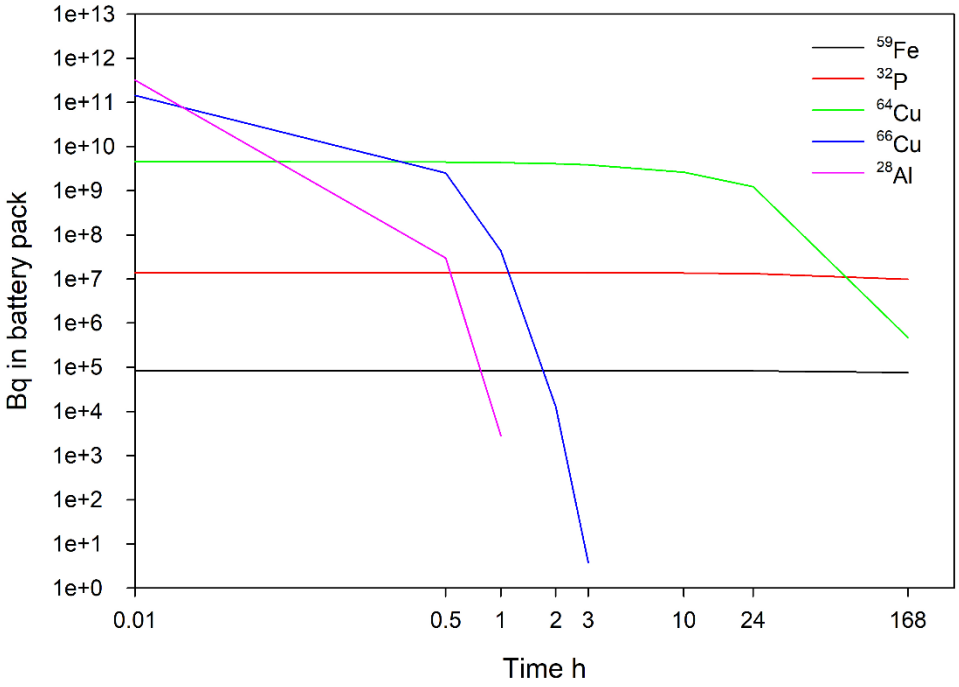

Figure 12. Activities induced in a 4000 cell array composed of LFP cells for an incident flux of $1x10^{12}$ n/cm^2.

6.2 Dose rates due to Activities Induced in Battery Packs

Estimated dose rates on the surface of the battery packs are presented in Figs. 13 -15. Only the simulated case 1 – activity within the 1 cm top layer of the battery – is plotted for each battery type. All nuclide-specific results for all simulated cases are in a tabulated form in Appendix 4. Bremsstrahlung is included only for the most important nuclide ^{32}P (LFP). The dose conversion factors of all high-energy beta emitters via Bremsstrahlung are tabulated in Appendix 8.

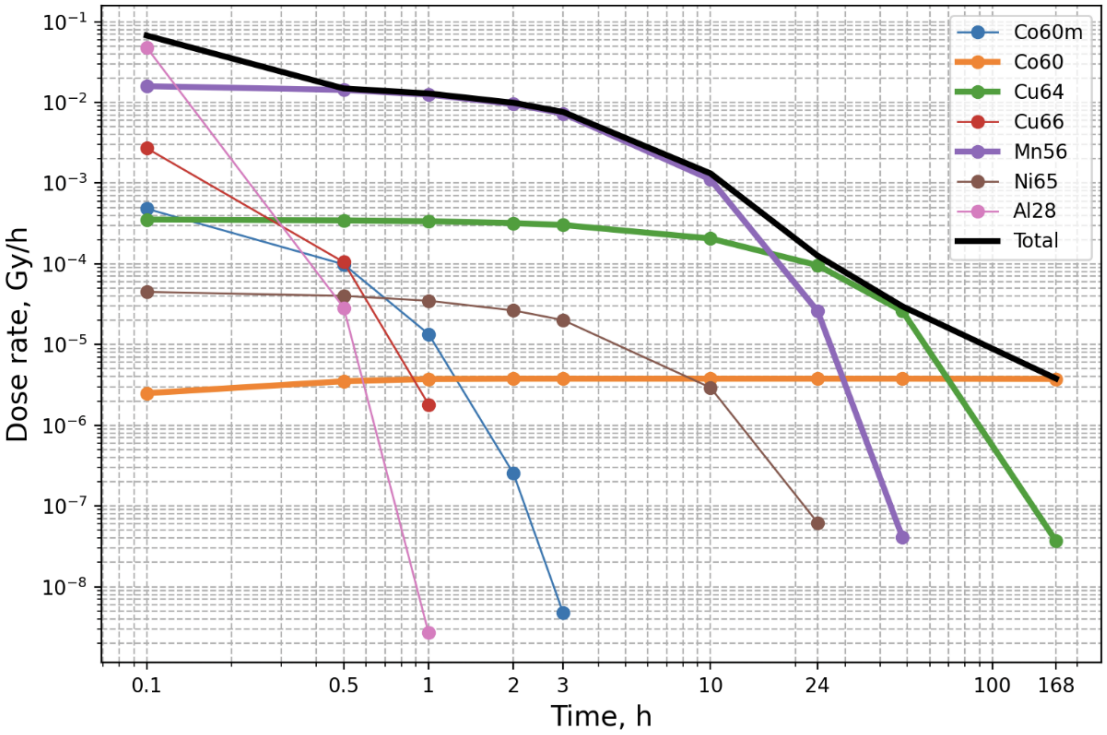

Figure 13. Dose rate from gamma emitters on the surface of the NCM battery (case 1) when exposed to thermal neutron fluence of 10^{12} n/cm2

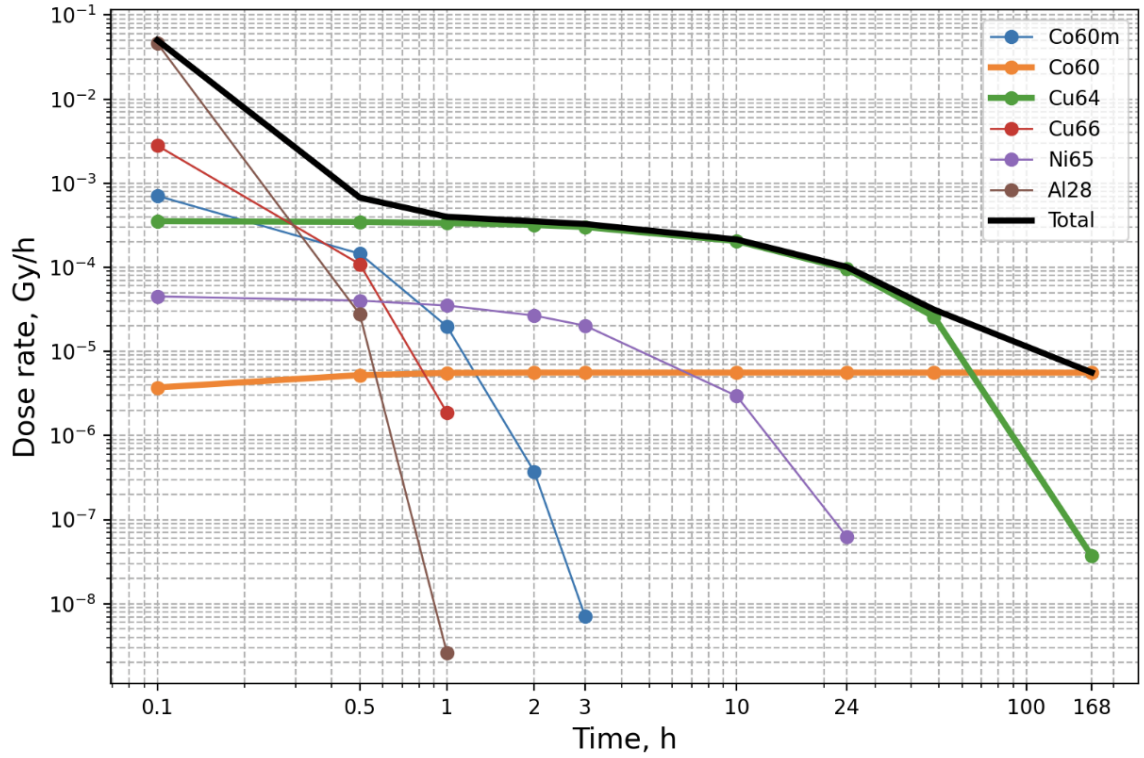

Figure 14. Dose rate from gamma emitters on the surface of the NCA battery (case 1) when exposed to thermal neutron fluence of 10^{12} n/cm2

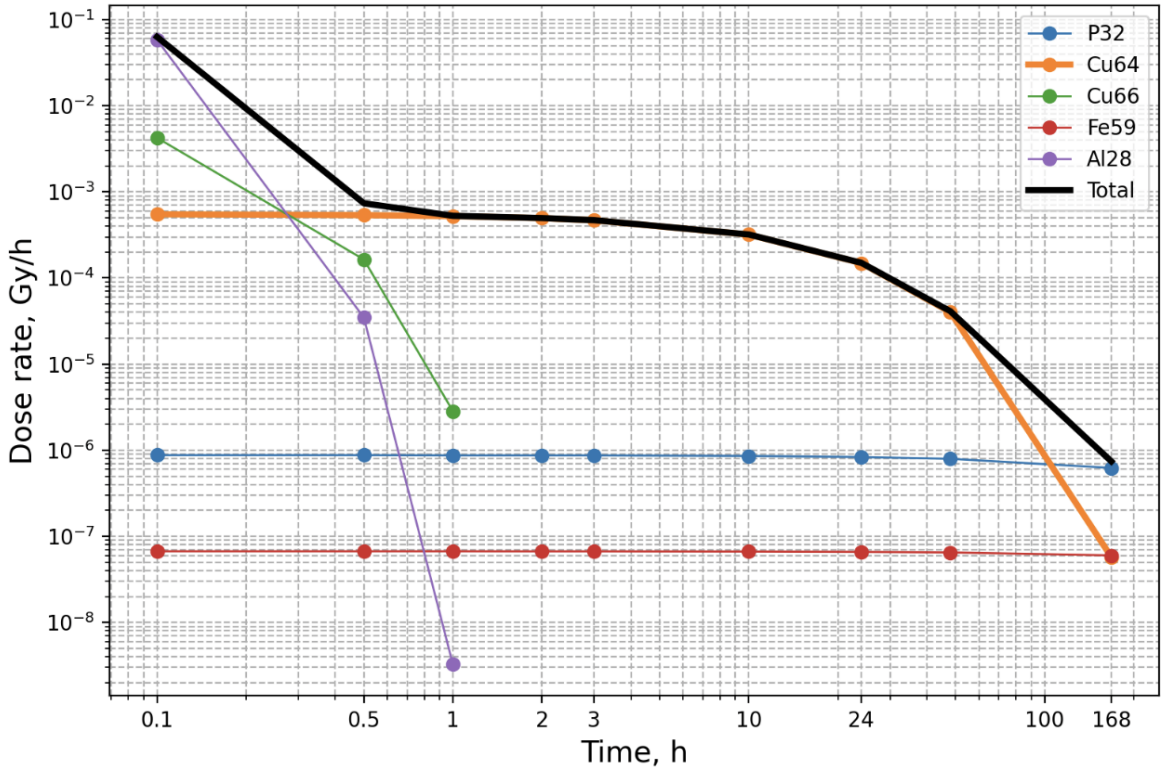

Figure 15. Dose rate from gamma emitters on the surface of the LFP battery (case 1) when exposed to thermal neutron fluence of 10^{12} n/cm2. ^{32}P refers to Bremsstrahlung solely.

6.3 Activities and dose rates induced in underlying pavement/road

To contextualize the induced activity in the battery packs, estimates were made of the activity potentially induced in a simple model of the underlying road surface. This model was constructed by representing the underlying surface as a 10 cm layer of asphalt overlying a 40 cm layer of compacted sand. A 5 m radius disk of these two substrates was then exposed to a centrally positioned 1 m^2 beam of 0.025 eV neutrons shooting directly down into the substrate (see Appendix 5). The induced activity in the substrate was then determined as previously. The main constituent of the substrate model contributing most to the overall dose rates above the substrate was Na in the underlying sand layer so three models were devised varying in the levels of Na in this material – 0.3 %, 1.7 % and 3 %. Activity estimates were then scaled to the same thermal neutron fluence as for the battery models – 10^{12} n/cm^2. Results are presented in Tables 7,8 and 9.

Isotope	0 h	0.5 h	1 h	2 h	3 h	10 h	24 h	48 h	168 h
^{24}Na	$1.6x10^8$	$1.5x10^8$	$1.5x10^8$	$1.4x10^8$	$1.4x10^8$	$9.9x10^7$	$5.2x10^7$	$1.7x10^7$	$6.6x10^4$
^{28}Al	$2.9x10^{10}$	$2.7x10^6$	$2.5x10^2$	-	-	-	-	-	-
^{52}V	$1.7x10^{10}$	$6.4x10^7$	$2.5x10^5$	$3.7x10^0$	-	-	-	-	-

Table 7. Activity estimates (Bq/m^2) for the asphalt – sand substrate with 3 % Na in the sand. Neutron fluence of 10^{12} n/cm^2, 0.025 eV.

Isotope	0 h	0.5 h	1 h	2 h	3 h	10 h	24 h	48 h	168 h
^{24}Na	$1.3x10^8$	$1.3x10^8$	$1.3x10^8$	$1.2x10^8$	$1.2x10^8$	$8.3x10^7$	$4.3x10^7$	$1.4x10^7$	$5.5x10^4$
^{28}Al	$4.2x10^{10}$	$3.9x10^6$	$3.6x10^2$	-	-	-	-	-	-
^{52}V	$1.6x10^{10}$	$6.1x10^7$	$2.4x10^5$	$3.5x10^0$	-	-	-	-	-

Table 8. Activity estimates (Bq/m^2) for the asphalt – sand substrate with 1.7 % Na in the sand. Neutron fluence of 10^{12} n/cm^2, 0.025 eV.

Isotope	0 h	0.5 h	1 h	2 h	3 h	10 h	24 h	48 h	168 h
^{24}Na	$1.9x10^7$	$1.9x10^7$	$1.8x10^7$	$1.8x10^7$	$1.7x10^7$	$1.2x10^7$	$6.4x10^6$	$2.1x10^6$	$8.0x10^3$
^{28}Al	$3.9x10^{10}$	$3.7x10^6$	$3.5x10^2$	-	-	-	-	-	-
^{52}V	$1.6x10^{10}$	$6.2x10^7$	$2.4x10^5$	$3.6x10^0$	-	-	-	-	-

Table 9. Activity estimates (Bq/m^2) for the asphalt – sand substrate with 0.3 % Na in the sand. Neutron fluence of 10^{12} n/cm^2, 0.025 eV.

Tables 7 - 9 show that ^{24}Na has the most significant activity in the road between 1 – 168 hours after the blast. Therefore, the dose rate analysis is made only for ^{24}Na using activities in Table 8 referring to Na concentration of 1.7 % in sand (PNNL material, type 306). The dose rate conversion factor in this road geometry is $8.01x10^{-13}$ Gy/h per Bq/m^2 (Appendix 5). The dose rate results are shown in Figures 25 and 26.

The dose rate estimate for the road has a large uncertainty by a factor of 5 – 10 depending on the road structure and sodium content. The sodium concentration can vary by a factor of 10 and photons of ^{24}Na are less attenuated in the roads where the sand is near the surface compared to the sand deeper under a thick layer of asphalt (10 cm).

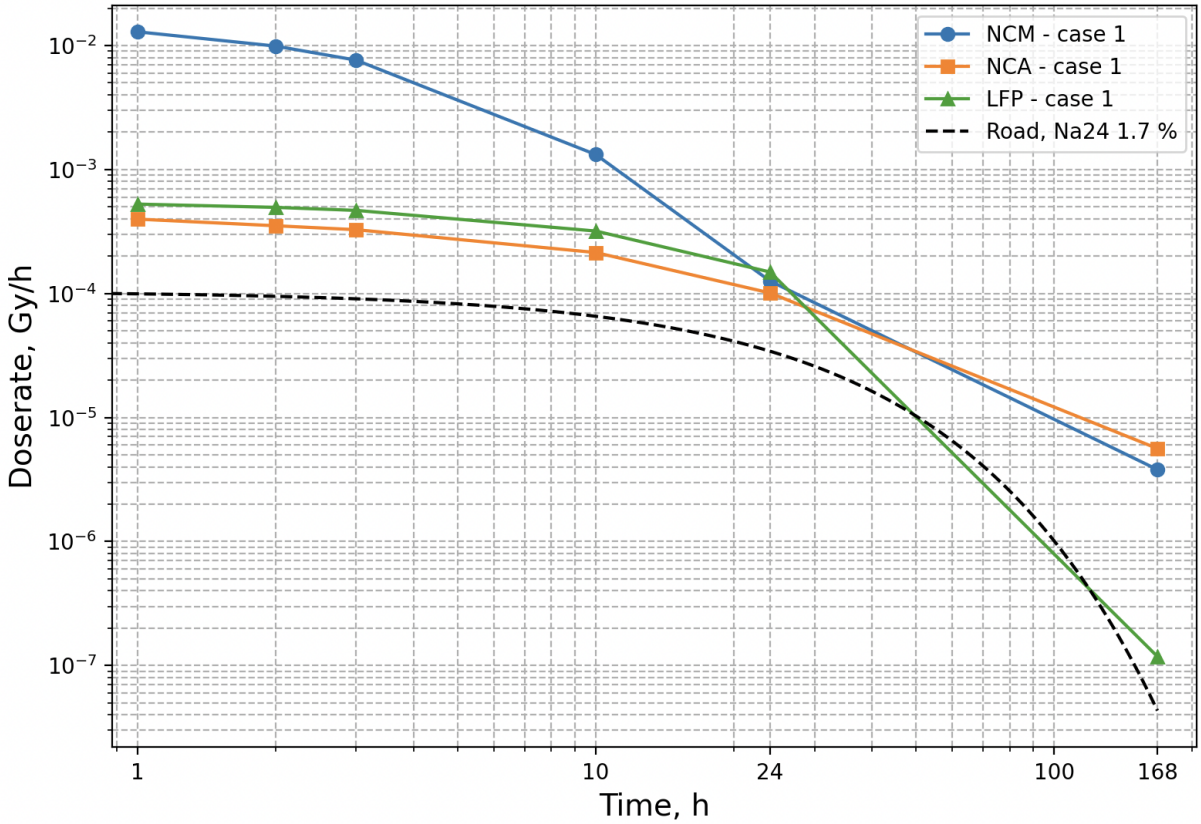

Figure 16. Dose rates on the battery surface and on the road 1 m above the ground level (case 1 for battery activities). Dose rate on the road has very large uncertainties (see text).

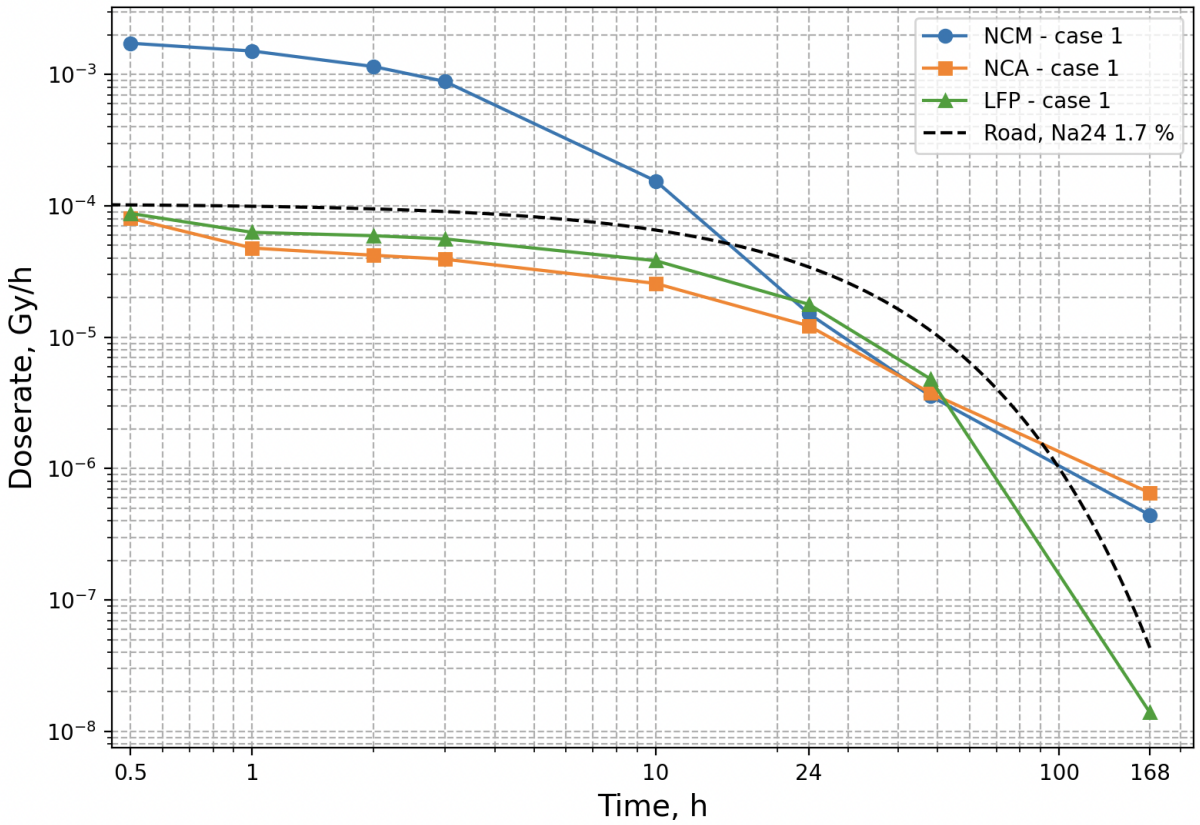

Figure 17. Dose rates 1 m from the battery surface and on the road 1 m above the ground level (case 1 for battery activities). Dose rate on the road has very large uncertainties (see text).

7. Gamma spectra

Gamma spectra were simulated for the activated batteries for the purpose of ascertaining the capacity of typical first responder detectors to identify the activation isotopes present in each case. For the spectra – only Case 1 was considered as qualitatively the spectra will be the same as for Case 2. A 3" NaI, a 1.5" LaBr and an approximately 40% HPGe were suspended face down 1 m above the largest surface of the battery pack (similar to being placed on the roof of a car). All detectors were simulated as having typical housings, electronics and other features present. For each of the three chemistries (which vary in terms of what isotopes are present) spectra were recorded for the 1-hour post irradiation point and the 24-hour post detonation point. 1-hour was chosen as it gives the most activity and isotopes without being too extreme and 24 hours was chosen as this is probably a point at which measurements in the field would be safe/possible/plausible. Certain modifications were made to the LFP spectra for practical reasons and these are detailed in Table 10 . The spectra were recorded for a little longer for the 24-hour time point. In addition, "calibration" spectra were devised for each chemistry type. These consisting of 1 MBq each of the following isotopes, distributed in exactly the same manner as for the activation isotopes. Am-241, Cd-109, Co-57, Co-60, Cs-137 and Na-22. The spectra were all accrued over the energy range 10-3500 keV with total channels varying between detector types. All spectra were developed with a "resolution" and a "no resolution" version. In all cases, the "resolution" versions had a simple resolution function applied. Effects such as summation and similar were not accounted for. Bremsstrahlung was not included

despite the fact that this would likely be a prominent feature for at least one of the battery chemistries.

	NCM811		NCA		LFP	
Isotope	1h	24 h	1h	24 h	1h	24 h
^{60m}Co	5.6x10^{9}	-	8.3x10^{9}	-	-	-
^{60}Co	2.2x10^{6}	2.2x10^{6}	3.3x10^{6}	3.3x10^{6}	-	-
^{56}Mn	1.1x10^{10}	2.3x10^{7}	-	-	-	-
^{65}Ni	9.4x10^{7}	1.7x10^{5}	9.4x10^{7}	1.7x10^{5}	-	-
^{64}Cu	2.8x10^{9}	7.9x10^{8}	2.7x10^{9}	7.8x10^{8}	4.4x10^{9}	2.6x10^{9}
^{66}Cu	2.7x10^{7}	-	2.8x10^{7}	-	2.5x10^{9}	-
^{59}Fe	-	-	-	-	8.5x10^{4}	8.3x10^{4}
^{28}Al	2.4x10^{3}	-	2.3x10^{3}	-	3.0x10^{7}	

Table 10. Activities induced in 4000-cell arrays composed of NCM811, NCA and LFP cells for an incident flux of 1x10^{12} n/cm^{2}.

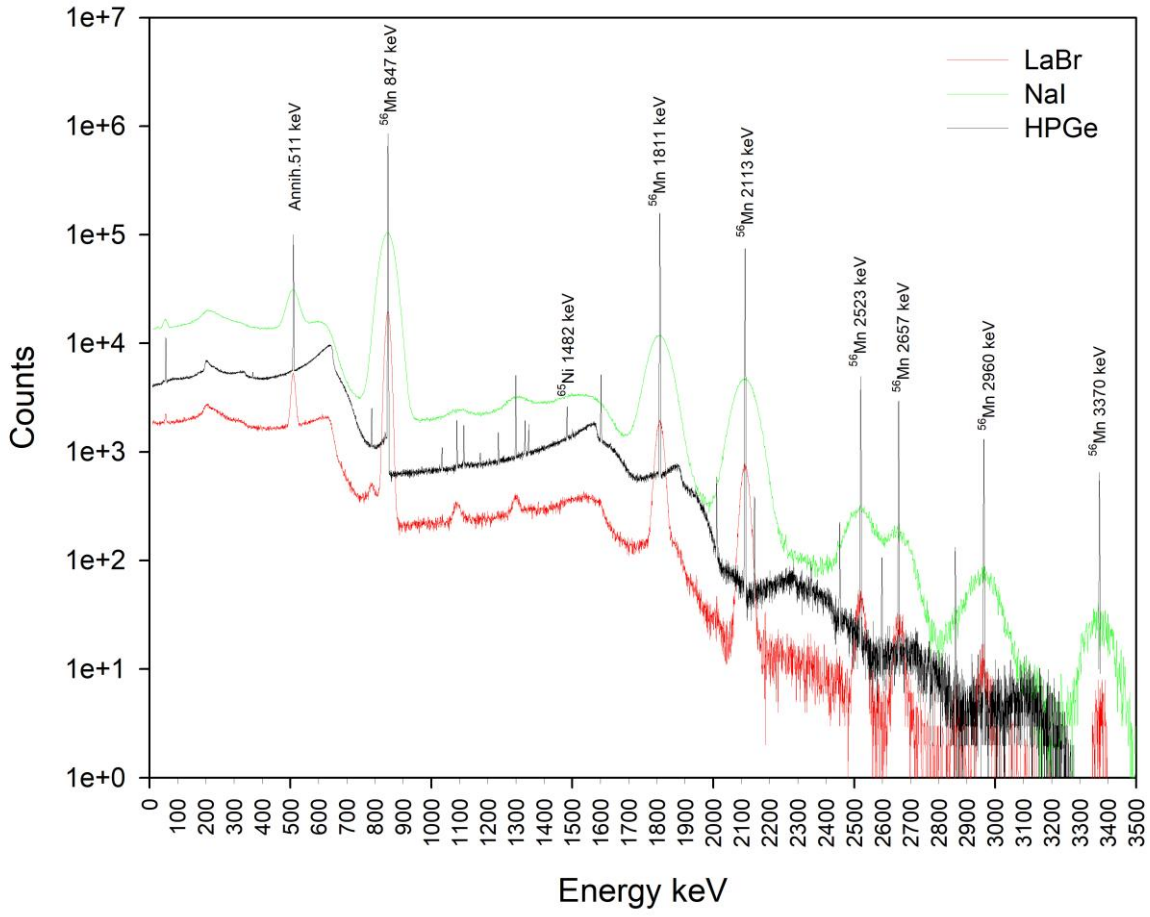

Figure 18. NCM-811 1 hour post activation spectra at 1 m distance for the three detector types. Live time 3 s.

8. Discussion

Across all three battery chemistries (NMC-811, NCA, LFP) studied as part of EVNUDET, neutron activation produced broadly similar families of isotopes, but at very different activity levels. Short-lived high-intensity gamma emitters dominate the initial activity: ^{56}Mn ($t_{½}$ = 2.6 h) is the major initial contributor for NMC/NCA battery types with very intense but short-lived contributions during the first few minutes from ^{28}Al ($t_{½}$ = 2.25 min). Longer-lived isotopes occurred in smaller quantities: ^{60}Co ($t_{½}$ = 5.27 y) being the primary long-term contributor followed by ^{59}Fe ($t_{½}$ = 44.5 d) and ^{32}P ($t_{½}$ = 14.3 d) being relevant for LFP only. During the first day NMC-811 packs produce the highest overall activity. After one week cobalt dominates the activity in NMC-811 and NCA packs. LFP batteries produce substantially less gamma-emitting isotopes on activation, lacking cobalt and nickel and being dominated largely by ^{32}P.

For a neutron fluence of 1×10^{12} n/cm², total gamma-relevant activity generated in all battery packs was of the order of $\sim10^{9}$–10^{10} Bq at the time of 24 hours. The most relevant nuclides are ^{64}Cu and ^{56}Mn (NCM-811 only). Long term activity (> 1 week) is dominated by ^{60}Co in NCM-811 and NCA and by ^{32}P in LFP.

High-energy beta emitters emit Bremsstrahlung, the yield being a few percent of total energy available for the beta decay. In a thermal neutron event irradiating NCM, NCA and LFP batteries, high-energy beta emitters, ^{28}Al, ^{65}Ni, ^{66}Cu, and ^{32}P, are formed. Aluminium-28 is the strongest gamma emitter during the first half an hour after the event, and its Bremsstrahlung may increase doserate by 20 %. Nickel-65 is not an important nuclide from the dose point of view. Bremsstrahlung of ^{66}Cu is stronger than its gamma radiation but the sum doserate of ^{66}Cu is not a significant factor as compared with the total doserate of the gamma emitters in the batteries. The Bremsstrahlung of ^{32}P is fully dominating the long-term doserate in LFP batteries.

An objective of the EVNUDET project was to evaluate how accurately Geant4 Monte Carlo simulations reproduce real-world neutron activation in materials relevant to EV battery systems. The study therefore conducted controlled activation experiments using metal cubes and indium monitor foils, and directly compared experimental activation ratios to both Geant4 simulation outputs and analytical activation functions (classical activation equations assuming uniform flux). This comparison served three purposes: to determine whether Geant4 correctly modelled neutron attenuation inside thick or high-cross-section materials, to validate the simulation framework used in the full EV battery activation modelling and to identify conditions where simplified analytical methods break down. The experiment used a 10×10×10 mm³ cube of one of three metals: Co, Cu and Al. An indium foil was mounted adjacent to the cube to serve as a neutron flux monitor via the reaction:

$$^{115}\mathrm{In}(n,\gamma)^{116\mathrm{m}}\mathrm{In}$$

The setup included 60 mm of mineral oil in front of the sample as a major neutron moderator with 80 mm polyethylene (PE) around and behind the sample. Samples were irradiated with a continuous neutron beam (nominal 2.4 MeV) using a neutron generator manufactured by Neutron Gate Ltd. Flux determination (via indium foil) was quantified using the known foil mass and the 1097 keV gamma line. Cube activation was quantified from gamma peaks of: $^{60\mathrm{m}}$Co for cobalt, ^{66}Cu for copper and ^{28}Al for aluminum. All computations accounted for counting period, detector efficiency, gamma intensity and half-life corrections. Rather than comparing absolute activity, the study used atom ratios. The Geant4 model included a full 3D geometry of cube, foil, oil, PE and sample holder with the neutron beam directed vertically

downward through oil layer. Activation was tallied using the HP neutron cross-section library with activity computed from isotope yields and decay constants. The simulations therefore capture neutron moderation, scattering, absorption, in-material attenuation and self-shielding and angular distributions of secondary radiation, all of which are absent in analytical methods. The analytical approach uses the standard activation equation with the following assumptions: uniform flux through entire sample volume, no neutron attenuation within the cube, no scattering effects and a monoenergetic thermal flux. These assumptions become invalid for high-cross-section materials (e.g., cobalt), non-uniform energy spectra, moderated beams with strong edge gradients and volumetric samples.

For Co, Geant4 predicts essentially lower ^{60m}Co production (by a factor of 2.4) than the experiment or analytical model. The most likely reason is severe neutron attenuation inside a cube of cobalt, which has a high thermal (n,γ) cross-section and very short mean free path (~0.30 cm for thermal neutrons). The analytical method overestimates activity because it assumes uniform flux whereas Geant4 is correctly modelling self-shielding, producing lower activation. The experimental result underestimates the activity because the gamma efficiency calibration of the sample geometry did not account for the uneven distribution of activated atoms. For cobalt, geometric and spectral effects dominate, and simple formulas fail. For Cu there is good agreement between Geant4, experiment and analytical methods with differences between methods being < 10–20%. Copper has a moderate neutron cross-section and longer mean free path (~3.11 cm). The flux inside the cube is therefore close to uniform and the analytical model is nearly valid. Geant4 slightly overpredicts activation with the experimental data lying between Geant4 and analytical results. It appears therefore that copper activation is predictable using both Monte Carlo and classical formulas. For Al there is also close agreement as Al has very low activation cross-section and most activation occurs near the surface, but attenuation is minimal. Differences between methods are small and consistent with analytical and Geant4 agreeing within ~10%, while experimental data is slightly lower.

A general conclusion is that Monte Carlo methods are essential for materials with high cross-sections or small mean free path; realistic dose predictions for EV batteries (which contain cobalt) require Monte Carlo transport. Analytical activation equations are acceptable for low-Z, low-cross-section materials such as aluminum and copper activation being predicted well with simple formulas. Experimental results validate the physical trends in Geant4. Even when magnitudes differ, Geant4 correctly predicts which materials have strong attenuation, the depth-dependence of reaction density and the overall ranking of materials by activation yield and isotopic composition of activation products.

Urban environments are composed of various materials that can be activated following a nuclear detonation. Structures such as concrete buildings and asphalt roads contain significant quantities of ^{23}Na, which is converted to ^{24}Na during a NUDET event. This study specifically examines asphalt roads where vehicles are parked, with the aim of assessing the dose rate produced by ^{24}Na in the road compared to the dose rate from vehicle batteries.

The sodium content within the road material plays a critical role; while asphalt itself contains minimal sodium, sand may exhibit a broad range of concentrations (0.3–3%). From an emergency response perspective, radiation exposure is primarily influenced by the surrounding urban infrastructure. However, when approaching an electric vehicle, responders may encounter elevated dose rates due to activation of battery materials. It is likely that rescue operations will not be feasible within the first day post-NUDET, allowing for substantial decay

of nuclides within the batteries and rendering their contribution to dose rate comparable to ambient urban exposure. Nevertheless, rescue teams must remain vigilant regarding additional hazards posed by damaged batteries, including contamination and potential beta particle emission.

9. References

Agostinelli, S., Allison, J., Amako, K.A., Apostolakis, J., Araujo, H., Arce, P., Asai, M.,Axen, D., Banerjee, S., Barrand, G.J.N.I., Behner, F., 2003. GEANT4—a simulationtoolkit. Nucl. Instrum. Methods Phys. Res. 506 (3), 250–303. https://doi.org/10.1016/S0168-9002(03)01368-8

Ank, M., Sommer, A., Abo Gamra, K., Schöberl, J., Leeb, M., Schachtl, J., Streidel, N., Stock, S., Schreiber, M., Bilfinger, P., Allgäuer, C., Rosner, P., Hagemeister, J., Rößle, M., Daub, R., Lienkamp, M. 2023. Lithium-Ion Cells in Automotive Applications: Tesla 4680 Cylindrical Cell Teardown and Characterization. Journal of The Electrochemical Society. http://dx.doi.org/10.1149/1945-7111/ad14d0.

Detwiler R.S., R.J. McConn, T.F. Grimes, S.A. Upton, and E.J. Engel. 2021. Compendium of Material Composition Data for Radiation Transport Modeling,.Rev 2. Richland, WA: Pacific Northwest National Laboratory. http://www.pnnl.gov/main/publications/external/technical_reports/PNNL-15870Rev2.pdf

Duvall, W., Philips, B., Hutcheson, A., Cordes, R.J., Hartsell, J., Strickman, M., 2019.Improving radiation transport simulation capabilities for nuclear threat detection using SWORD. In: 2019 IEEE International Symposium on Technologies for Homeland Security (HST), pp. 1–6. https://doi.org/10.1109/HST47167.2019.9032903

Kovachev, G., Schröttner, H., Gstrein, G., Aiello, L., Hanzu, I., Wilkening, M., Foitzik, A., Wellm, M., Sinz, W., Ellersdorfer, C. 2019. Analytical Dissection of an Automotive Li-Ion Pouch Cell. Batteries. 5/67. http://dx.doi.org/10.3390/batteries5040067

Quinn, J., Waldmann, T., Richter, K., Kasper, M., Wohlfahrt-Mehrens, M. 2018. Energy Density of Cylindrical Li-Ion Cells: A Comparison of Commercial 18650 to the 21700 Cells. Journal of The Electrochemical Society, 165. A3284-A3291. http://dx.doi.org/10.1149/2.0281814jes

Spriggs, D. et al. 2020. Fallout Cloud Regimes, LLNL-JRNL-813959: https://www.osti.gov/servlets/purl/1771428

APPENDIX 1

Generation of Neutrons in a Nuclear Detonation

Nuclear detonation generates a large number of neutrons through several physical processes associated with both fission and fusion reactions during the generation which play a critical role in maintaining the chain reaction in a fission device and initiating fusion reactions in a thermonuclear device. In addition, the generated neutrons also contribute to secondary effects which include, and of most relevance to this study, neutron activation.

In a fission device, neutrons are primarily generated when heavy atomic nuclei such as ^{235}U or ^{239}Pu, undergo fission. Each fission event produces two to three neutrons, which can subsequently induce further fission reactions and in this manner sustain the chain reaction.

The number of neutrons released per fission event is depends on the fissile material involved:

- for ^{235}U approximately 2.4 neutrons are generated per fission event
- for ^{239}Pu: approximately 2.9 neutrons are generated per fission event

These prompt neutrons are generated almost instantaneously and are those that propagate the fission chain reaction.

For thermonuclear devices, neutron generation is significantly augmented by fusion reactions where the intense heat and pressure caused by the primary fission explosion ignites the fusion fuel, typically consisting of ^{2}H (deuterium) and ^{3}H (tritium), with the fusion reactions that generate neutrons being:

- Deuterium-tritium ($D + T$) fusion:
- Deuterium-deuterium ($D + D$) fusion:

This former generates high-energy 14.1 MeV neutrons which contribute to the explosion's yield and the latter $D + D$ reaction generates fewer neutrons as compared to $D + T$ fusion but still contributes to the total neutron generation. These fusion generated neutrons function to increase the efficiency of the detonation by inducing further fission in the surrounding ^{238}U tamper material and contribute to the radiological effects of the detonation by causing neutron activation in nearby materials.

The quantity of neutrons generated per kiloton (kt) depends on the type of device (fission or fusion), its efficiency, and the specific nuclear reactions involved. A 1 kt fission device releases $\approx 4.18 \times 10^{12}$ J of energy which is equivalent to $\approx 2.61 \times 10^{25}$ MeV. If it assumed that each fission event releases ≈ 180 MeV, then 1 kt corresponds to 1.45×10^{23} fission events. For a ^{239}Pu based device (≈ 2.9 neutrons per fission), this corresponds to $\approx 4.2 \times 10^{23}$ neutrons. As ^{235}U results in fewer neutrons, this value would be slightly less for a ^{235}U device.

For fusion (thermonuclear) weapons, the secondary stage of the weapon contains fuel for the fusion reaction and is usually a blend of deuterium (D) and tritium (T) or lithium deuteride (LiD). These fuels undergo reactions such as:

D-T Fusion (the main reaction in thermonuclear weapons):

$$D+T \rightarrow {}^{4}He+n+17.6\ MeV$$

Each reaction of this type releases 1 neutron with energies of 14.1 MeV which are higher than those resulting from fission processes. For weapons using lithium deuteride (LiD) as a fuel, fast neutrons from the fission process cause lithium-6 to produce tritium:

$$^{6}Li+n \rightarrow T+{}^{4}He$$

This generated tritium then participates in $D + T$ fusion reactions resulting in the release of even more neutrons (1 per reaction). The neutron yield from the fusion reactions would then come in addition to the neutrons generated by the initiating fission process. The fission process of the primary stage generates ≈ 4.2×10^{23} n/kt for ^{239}Pu or ≈ 3.5×10^{23} n/k for ^{235}U.

The fusion processes of the secondary stage, which are the dominant ones in a fusion based device result in the following neutron yields:

$D + T \rightarrow {}^{4}He\ (3.5\ MeV) + n\ (14.1\ MeV) \rightarrow$ 1 neutron per fusion

$D + D \rightarrow {}^{3}He\ (0.82\ MeV) + n\ (2.45\ MeV) \rightarrow \approx$ 0.5 neutrons per fusion

$D + D \rightarrow T\ (1.01\ MeV) + p\ (3.02\ MeV) \rightarrow$ no neutrons

$T + D \rightarrow$ essentially the same as D-T, 1 neutron per fusion

Efficient device designs rely on $D + T$ fusion resulting in 1 14.1 MeV neutron per reaction.

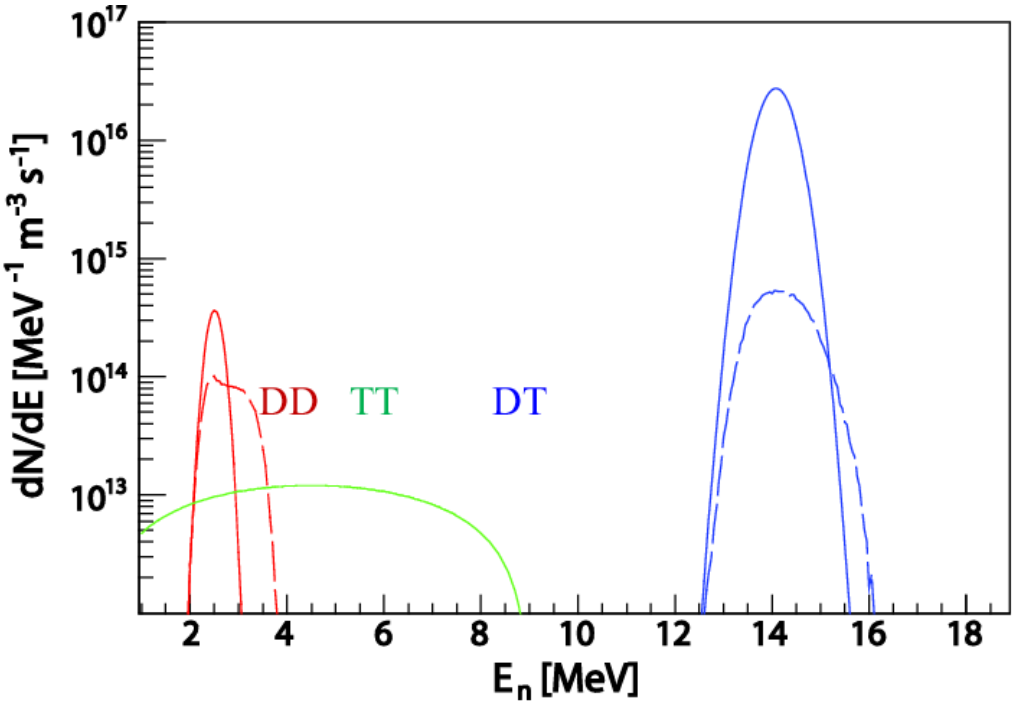

Figure A1.1 Fusion processes of the secondary stage and energies.

In the tertiary stage of a fusion device, the fast fusion neutrons can induce fission in a ^{238}U tamper resulting in additional neutron generation (≈2.4 per fission).

If it assumed that the entire 1 kt results from $D + T$ reactions and that the 1 kt corresponds to ≈ 4.2 x 10^{12} J, if each $D + T$ fusion reaction results in 17.6 MeV (where 3.5 MeV goes to ^{4}He and 14.1 MeV to the neutron), then the number of $D + T$ fusion reactions per kt would be ≈ 4.2 x 10^{12} J/(17.6 MeV x 1.602 x 10^{-13} J/MeV) = ≈1.48 x 10^{24} n/kt for the D-T fusion reactions alone. To this would have to be added neutrons generated by the fission of the primary (either ^{235}U or ^{239}Pu based) and neutrons generated by fission processes initiated in the ^{238}U tamper.

Based on similar calculations the neutron yields for the Fat Man (^{239}Pu) and Little Boy (^{235}U) devices can be estimated as being of the order of ≈ 8.8 x 10^{24} neutrons and ≈ 5.3 x 10^{24} neutrons respectively. Had both these devices been fusion devices, it could be estimated that the neutron yield would have been ≈4 – 10 times greater.

The nature of the neutrons generated by the two device types differs substantially depending on whether or not the device is fission or fusion based. For fission weapons where the neutrons are generated by the fission of nuclei of ^{239}Pu or ^{235}U, the prompt neutrons (comprising ≈99% of all neutrons produced) have a peak energy in the range ≈ 1 – 2 MeV with an average of 2 MeV. The spectrum is a Watt spectrum which peaks at ≈ 0.7 MeV and falls away exponentially in energy with a high energy "tail" exceeding 10 MeV (≈ 0.1 %). Delayed neutrons which are generated after the prompt neutrons and comprise ≈ 1% of all neutrons produced typically have an energy of ≈ 0.25 – 0.6 MeV. For fusion-based devices, the neutrons are released by $D + T$ fusion reaction and have a peak energy of 14.1 MeV with the less common $D + D$ reaction generating neutrons with an energy of ≈ 2.45 MeV. Neutrons generated by the tertiary stage are fission neutrons with a similar spectrum to those generated in a fission device. There are no delayed neutrons in a fusion reaction. Neutrons generated by fusion reactions are radiologically more injurious due to their energy and harder to shield against.

The nature of the differences between the neutrons generated by fusion and fission reactions have implications for neutron activation of materials in the environment. Fission neutrons have lower energy and thermal/epithermal neutrons (in the range of <1 eV to 1 keV) undergo capture reactions (n,γ) to form radioactive isotopes. As an example:

$$^{59}Co + n \rightarrow {}^{60}Co$$

Fast neutrons (1 keV – 10 MeV) activate materials through inelastic scattering processes.

$$^{63}Cu + n \rightarrow {}^{64}Cu$$

Fusion generated neutrons are dominated by high energy reactions, knocking out extra neutrons or exciting atomic nuclei generating unstable isotopes.

$$^{27}Al + n \rightarrow {}^{26}Al + 2n$$

Metals may undergo spallation where 14 MeV neutrons break nuclei and generate fragments or secondary activation such as the generation of tritium in lithium.

$$^{6}Li + n \rightarrow {}^{3}H + {}^{4}He$$

Fission generated neutrons will, in terms of their reactions with metals, be dominated primarily by thermal neutron capture reactions generating isotopes such as ^{55}Fe, ^{60}Co, ^{24}Na and ^{56}Mn. Fusion generated neutrons will cause high energy transmutations such as ^{27}Mg from ^{27}Al, ^{16}N from ^{16}O and ^{56}Mn from ^{56}Fe. In general, isotopes generated by fusion neutrons tend to decay relatively quickly while those generated by fission neutrons may be longer lived. The suite of isotopes generated by fusion neutrons may be greater than that for fusion neutrons.

Neutron fluences (in terms of total neutrons per cm^2) differ between fusion and fission devices and how that fluence behaves over distance is determined by the inverse square law and how the neutrons interact with the atmosphere. For a device such as Fat Man, the total generation of neutrons was $\approx 8.8 \times 10^{24}$ neutrons and the fluence at a distance of 1000 m would have been of the order $\approx 10^{14}$ $n/cm^2/s$ for the initial flux with a time integrated fluence at 1000 m of $\approx 10^{15}$ n/cm^2. For large thermonuclear weapons (1 Mt), this fluence would have been of the order of $\approx 10^{17}$ n/cm^2 at the same distance. This reduction in fluence as a function of distance from the detonation is due to the effects of the inverse square law and absorption and scattering of the neutrons in the atmosphere. The mean free path of neutrons in the energy range 1 – 14 MeV is of the order of 200 – 500 m depending on the atmospheric properties.
Neutron fluence for fission weapons can be estimated by:

$$\Phi(r) \approx (\Phi_0 \cdot e^{-r/\lambda})/\, r^2$$

where Φ_0 is the fluence ($\approx 10^{15}$ n/cm^2 at 1 km for a Fat Man device), r is the distance in km and λ is the attenuation length ($\approx$ 300 m for fission neutrons in air at sea-level). The attenuation length will be larger for neutrons generated by a fusion device due to the higher energy.

Using the above, for a Fat Man type device, the neutron fluence would be of the order of 10^{16} n/cm^2 at 500 m from detonation, 10^{15} n/cm^2 at 1000m, 10^{13} n/cm^2 at 2000 m and 10^{10} n/cm^2 at 5 km. For fusion neutrons these values may be orders of magnitude higher due to higher neutron yields and longer free paths in air. It should be noted that neutrons generated at higher altitudes will travel farther due to there being less scattering and absorption in air at higher altitudes.

Behaviour of neutrons in air

The neutrons generated by either a fission or fusion weapon undergo a series of interactions with the constituents of the atmosphere, primarily nitrogen (^{14}N) and oxygen (^{16}O), which dictates to a large extent their spatial and temporal distribution. The initial neutron energy spectrum from fission weapons, typically spans an energy range from approximately 0.1 MeV to over 10 MeV, with a most probable energy around 1-2 MeV. Fusion reactions produce neutrons with a significantly higher characteristic energy of approximately 14.1 MeV which undergo a series of scattering events with atmospheric nuclei. The dominant interaction mechanism for these fast neutrons in the atmosphere is inelastic scattering where a neutron interacts with a target nucleus and transfers a portion of its kinetic energy to excite the nucleus to a higher energy level. The excited nucleus subsequently de-excites by the emission of one or more gamma rays. This interaction can be described as:

$$E' = E - E_{excitation} - \Delta E_{kinetic}$$

Where E is the energy of the incident neutron, E' is the final energy of the neutron, $E_{excitation}$ is the excitation energy of the target nucleus and $\Delta E_{kinetic}$ is the energy lost to recoil motion.

The energy threshold for inelastic scattering depends on the target nucleus and for ^{14}N the threshold is approximately 2.3 MeV. Inelastic scattering serves as the main mechanism for the rapid reduction of the initial neutron energies where a significant fraction of the energy is deposited directly into the atmosphere as the kinetic energy of the recoil nuclei and the emitted gamma radiation. The probability of inelastic scattering is energy-dependent and is characterized by the inelastic scattering cross-section. As the neutrons undergo multiple inelastic scattering events, their average kinetic energy decreases and eventually falls into the keV range where elastic scattering becomes more and more significant. In this interaction, kinetic energy and momentum are conserved and while the energy transfer per elastic collision with light nuclei like nitrogen and oxygen can be significant, the cumulative effect of many elastic collisions leads to further moderation of the neutron energy. The probability of elastic scattering is described by the elastic scattering cross-section.

The energy of one neutron after one elastic collision interaction is given by:

$$\left(\frac{A^2 + 1 + 2A\ cos\ cos\ \theta}{(A+1)^2}\right)$$

where E is the incident neutron energy, E' is the neutron energy after the scattering interaction, A is the mass number of the target nucleus and θ is the scattering angle.

Upon reaching a thermal equilibrium with the surrounding air molecules (average kinetic energy ~0.025 eV at standard temperature), neutrons are classed as thermal neutrons and at these energies, the probability of neutron capture reactions becomes significant. In atmospheric air, the dominant thermal neutron capture reaction involves ^{14}N via the *(n, p)* reaction:

$$n + {}^{14}N \rightarrow {}^{14}C + p$$

Nitrogen may also undergo capture via the less prevalent *(n, γ)* reaction:

$${}^{14}N + n \rightarrow {}^{15}N + \gamma$$

The main neutron capture reaction of atmospheric oxygen is the *(n, γ)* reaction:

$${}^{16}O + n \rightarrow {}^{17}O + \gamma$$

This reaction is relatively rare given oxygens low neutron capture cross section. For higher neutron energies, oxygen may undergo *(n, p)* and *(n, α)* reactions with the former resulting in the formation of ^{16}N which is a strong emitter of beta and gamma radiation.

The mean free path (λ) refers to the average distance a neutron will travel before undergoing an interaction such as those described above. It is described by:

$$\lambda = \frac{1}{n \cdot \sigma}$$

where n is the density of the target atoms (atoms/cm^3), σ is the total interaction cross section (cm^2) and λ is the mean free path (cm). The σ term is dependent on the interaction type.

The altitude of the detonation has a significant impact on neutron behavior, at higher altitudes, the lower density of the atmosphere diminishes the probability of neutron interactions per unit path length resulting in a larger mean free path and a wider spatial distribution of the neutron flux. Conversely, detonations at lower altitudes with higher atmospheric densities result in more rapid neutron attenuation over distance due to the higher density of nuclei available for interaction.

APPENDIX 2

Projection of a Cuboid on a Plane Perpendicular to a Particle Beam

The projection of a 3D object onto a plane perpendicular to an incident beam of particles is a crucial problem in radiation physics where there are at least two applications: low-energy photons (< 60 keV) and thermal neutrons in materials of high (*n,g*) cross section, such as lithium (940 barn). This section provides a rigorous mathematical approach to computing the shadow cast by a box, or cuboid, when it is irradiated in a parallel beam of particles which are stopped when hitting the target. The projection is derived by computing the shadow formed by the eight vertices of the cuboid and then constructing the convex hull. The method is valid for any convex object with known vertices.

Defining the Cuboid and the Projection Plane

Consider a cuboid defined in three-dimensional space with dimensions *A* (width along the x-axis), *B* (height along the y-axis) and *C* (depth along the z-axis). The eight vertices of the cuboid are:

P_1= (0, 0, 0) P_2 = (A, 0, 0) P_3 = (0, B, 0) P_4 = (A, B, 0)
P_5 = (0, 0, C) P_6 = (A, 0, C) P_7 = (0, B, C) P_8 = (A, B, C)

The particle beam direction is defined by a unit vector (viewing direction):

$$v(\theta, \varphi) = (cos(\theta)cos\,(\varphi)\,, cos\,(\theta)\,sin\,(\varphi)\,, sin\,(\theta))$$

where ϕ is the azimuth angle, i.e., rotation around the z-axis, and θ is the elevation angle.

Computing the Projection of Each Vertex

A point *P* is projected onto the plane perpendicular to the viewing vector $\boldsymbol{v}$ as

$$\boldsymbol{P'} = \boldsymbol{P} - (\boldsymbol{v} \cdot \boldsymbol{P})\boldsymbol{v}$$

This equation ensures that the projected point lies in the plane orthogonal to the unit vector $\boldsymbol{v}$. The dot product and vector $\boldsymbol{v}$ remove the component which is parallel to $\boldsymbol{v}$, leaving only the component which lies in the perpendicular plane.

Constructing the 2D Projection Coordinates

To analyze the projection in a 2D coordinate system, two basis vectors are defined spanning the projection plane.

The first basis vector is chosen to be orthogonal to $\boldsymbol{v}$:

$$\boldsymbol{b}_1 = (-v_y, v_x, 0)$$

The vectors $\boldsymbol{b_1}$ and $\boldsymbol{v}$ are indeed orthogonal because their dot product is zero. If v_x and v_y are both zero, i.e., $\boldsymbol{v}$ is parallel to z axis, then simply $\boldsymbol{b_1}$ = (1, 0,0).

The second basis vector is obtained using the cross-product:

$$\boldsymbol{b}_2 = \boldsymbol{v} \times \boldsymbol{b}_1$$

These two vectors form an orthonormal basis for the projection plane. Now, the projected 3D points are mapped to 2D coordinates:

$$x' = \boldsymbol{P'} \cdot \boldsymbol{b}_1 \text{ and } y' = \boldsymbol{P'} \cdot \boldsymbol{b}_2$$

Computing the Shadow Area

Once all eight projected vertices have been determined in 2D, the convex hull of these points can be calculated. The area of the convex hull represents the shadow area of the cuboid:

$$A_{shadow} = \frac{1}{2}\sum_{i=1}^{n-1}(x_i y_{i+1} - x_{i+1} y_i)$$

This formula is known as the shoelace formula, and it computes the area of a polygon given its ordered vertices. The shoelace formula itself does not inherently account for whether some vertices are inside the shadow**.** However, the convex hull computation automatically eliminates interior points before applying the shoelace formula. Figure A2.1 is an example of the shadow calculation.

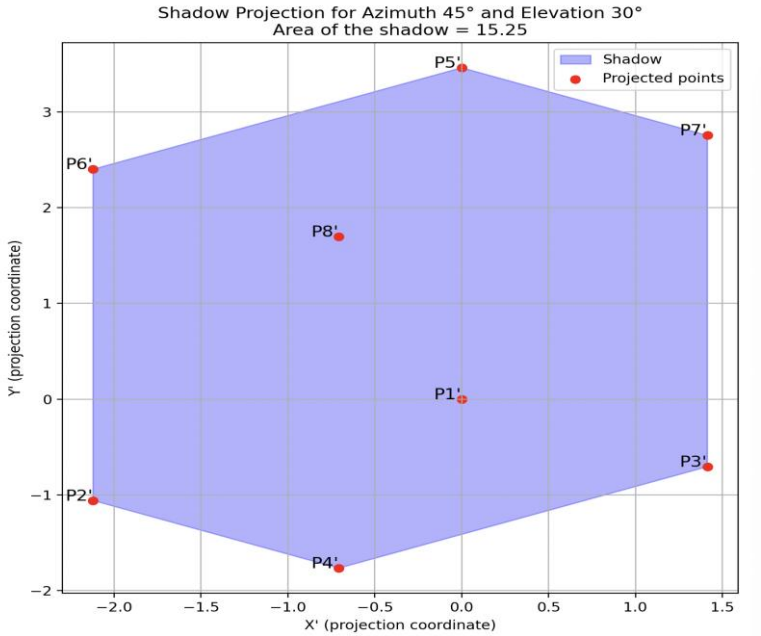

Figure A2.1. A box with dimensions of A, B, C = 3, 2, 4 projected to a direction having azimuth of 45 degrees and elevation angle of 30 degrees. Points P_1' and P_8' are eliminated by the convex hull, making the other projection points ready for the area calculation.

The shadow of a flat object is shown in Figure A2.2 as a function of the elevation angle. The projection area is dominated for the angles near the top view; the side direction has a projection area of 7 % for the azimuth of 0 degree and 10 % for the azimuth of 45 degrees relative to the top view.

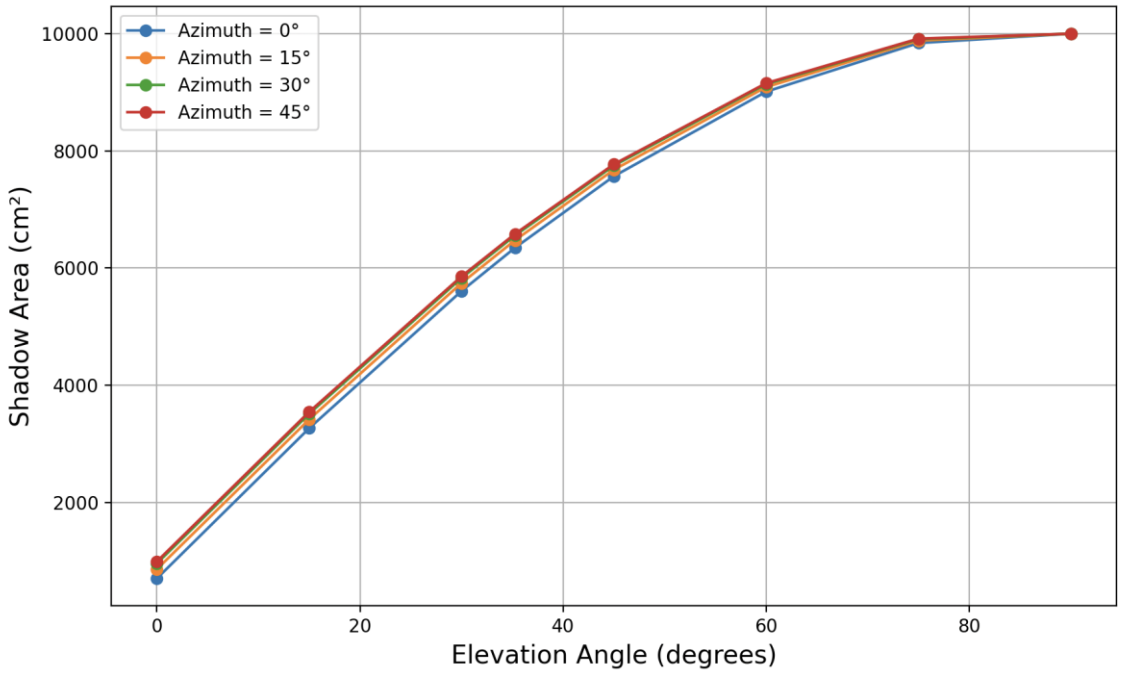

Figure A2.2. Projection area of a box with dimensions of (100 cm, 100 cm, 7 cm) on a plane perpendicular to the viewing direction.

The cells in a battery are packed in a form of cuboid. The neutrons can enter this rectangular box from different directions. If the object size is small compared with the mean free path of the neutrons, all target atoms are in the same position relative to the neutron flux. This means that the number of neutron reactions depends only on the mass of the target. However, when the object dimensions are much larger than the mean free path, the cross section – or the shadow opposite to the beam direction of neutrons – is of vital importance. Then the number of neutron reactions depends not only on the mass of the target but also on its surface area. The bigger the shadow, the more neutron reactions.

The batteries are mainly irradiated with neutrons arriving from the angles above the array. In a uniform irradiation of a flat large target, the cells on the edges receive more neutrons than the cells inside the array, and most of the neutrons hitting the outer cells are absorbed there. There is, however, another phenomenon which reduces the number of neutron interactions in the outer cells. The cells inside the array get more benefit from the scattered neutrons; the cells on the edges have less neighbors as a source of scattered neutrons. In brief, for radiation safety studies, it is fully justified that the cells in a battery are evenly exposed in a thermal neutron flux.

APPENDIX 3

Activities Induced in Battery Packs in Thermal Neutron Fluence

Isotope	0 h	0.5 h	1 h	2 h	3 h	10 h	24 h	168 h
^{60m}Co	3x10^{11}	4.1x10^{10}	5.6x10^{9}	1.05x10^{8}	2x10^{6}	-	-	-
^{60}Co	1.1x10^{6}	2.1x10^{6}	2.2x10^{6}	2.3x10^{6}	2.2x10^{6}	2.3 x10^{6}	2.2x10^{6}	2.2x10^{6}
^{56}Mn	1.5x10^{10}	1.3x10^{10}	1.1x10^{10}	8.6x10^{9}	6.6x10^{9}	1.0 x10^{9}	2.3x10^{7}	-
^{65}Ni	1.2x10^{8}	1.1x10^{8}	9.4x10^{7}	7.1x10^{7}	5.4x10^{7}	7.9x10^{6}	1.7x10^{5}	-
^{64}Cu	2.9x10^{9}	2.8x10^{9}	2.8x10^{9}	2.6x10^{9}	2.5x10^{9}	1.7x10^{9}	7.9x10^{8}	3.0x10^{5}
^{66}Cu	9.2x10^{10}	1.6x10^{9}	2.7x10^{7}	8.1x10^{3}	2.4x10^{0}	-	-	-
^{28}Al	2.7x10^{11}	2.5x10^{7}	2.4x10^{3}	-	-	-	-	-

Table A3.1 Activities induced in a 4000 cell array composed of NCM811 cells for an incident fluence of 1x10^{12} n/cm^{2}.

Isotope	0 h	0.5 h	1 h	2 h	3 h	10 h	24 h	168 h
^{60m}Co	4.4x10^{11}	6.0x10^{10}	8.3x10^{9}	1.6x10^{8}	2.9x10^{6}	-	-	-
^{60}Co	1.7x10^{6}	3.1x10^{6}	3.3x10^{6}	3.3x10^{6}	3.3x10^{6}	3.3x10^{6}	3.3x10^{6}	3.3x10^{6}
^{65}Ni	1.2x10^{8}	1.1x10^{8}	9.4x10^{7}	7.2x10^{7}	5.4x10^{7}	7.9x10^{6}	1.7x10^{5}	-
^{64}Cu	2.9x10^{9}	2.8x10^{9}	2.7x10^{9}	2.6x10^{9}	2.5x10^{9}	1.7x10^{9}	7.8x10^{8}	3.0x10^{5}
^{66}Cu	9.4x10^{10}	1.6x10^{9}	2.8x10^{7}	8.3x10^{3}	2.5x10^{0}	-	-	-
^{28}Al	2.6x10^{11}	2.4x10^{7}	2.3x10^{3}	-	-	-	-	-

Table A3.2 Activities induced in a 4000 cell array composed of NCA cells for an incident ffluence of 1x10^{12} n/cm^{2}.

Isotope	0 h	0.5 h	1 h	2 h	3 h	10 h	24 h	168 h
^{59}Fe	8.5x10^{4}	8.5x10^{4}	8.5x10^{4}	8.5x10^{4}	8.5x10^{4}	8.4x10^{4}	8.3x10^{4}	7.6x10^{4}
^{32}P	1.4x10^{7}	1.4x10^{7}	1.4x10^{7}	1.4x10^{7}	1.4x10^{7}	1.4x10^{7}	1.3x10^{7}	9.9x10^{6}
^{64}Cu	4.56x10^{9}	4.4x10^{9}	4.3x10^{9}	4.1x10^{9}	3.9x10^{9}	2.6x10^{9}	1.2x10^{9}	4.7x10^{5}
^{66}Cu	1.5x10^{11}	2.5x10^{9}	4.3x10^{7}	1.3x10^{4}	3.8x10^{0}	-	-	-
^{28}Al	3.2x10^{11}	3.0x10^{7}	2.8x10^{3}	-	-	-	-	-

Table A3.3 Activities induced in a 4000 cell array composed of LFP cells for an incident fluence of 1x10^{12} n/cm^{2}.

APPENDIX 4

Dose rate Induced by Battery Packs, Gy/h

Isotope	0 h	0.5 h	1 h	2 h	3 h	10 h	24 h	168 h
^{60m}Co	$7.2x10^{-4}$	$9.9x10^{-5}$	$1.3x10^{-5}$	$2.5x10^{-7}$	$4.8x10^{-9}$	-	-	-
^{60}Co	$1.9x10^{-6}$	$3.5x10^{-6}$	$3.8x10^{-6}$	$3.8x10^{-6}$	$3.8x10^{-6}$	$3.8x10^{-6}$	$3.8x10^{-6}$	$3.8x10^{-6}$
^{56}Mn	$1.6x10^{-2}$	$1.4x10^{-2}$	$1.3x10^{-2}$	$9.6x10^{-3}$	$7.3x10^{-3}$	$1.1x10^{-3}$	$2.6x10^{-5}$	-
^{65}Ni	$4.6x10^{-5}$	$4.0x10^{-5}$	$3.5x10^{-5}$	$2.6x10^{-5}$	$2.0x10^{-5}$	$2.9x10^{-6}$	$6.2x10^{-8}$	-
^{64}Cu	$3.5x10^{-4}$	$3.5x10^{-4}$	$3.4x10^{-4}$	$3.2x10^{-4}$	$3.0x10^{-4}$	$2.1x10^{-4}$	$9.6x10^{-5}$	$3.7x10^{-8}$
^{66}Cu	$6.1x10^{-3}$	$1.1x10^{-4}$	$1.8x10^{-6}$	-	-	-	-	-
^{28}Al	$3.1x10^{-1}$	$2.9x10^{-5}$	$2.7x10^{-9}$	-	-	-	-	-
Total	$3.3x10^{-1}$	$1.5x10^{-2}$	$1.3x10^{-2}$	$9.9x10^{-3}$	$7.6x10^{-3}$	$1.3x10^{-3}$	$1.3x10^{-4}$	$3.8x10^{-6}$

Table A4.1 Dose rates at the surface a 4000 cell array composed of NCM811 cells exposed to an incident fluence of $1x10^{12}$ n/cm^2. Activity distributed through the outermost 1 cm of the battery pack.

Isotope	0 h	0.5 h	1 h	2 h	3 h	10 h	24 h	168 h
^{60m}Co	$8.6x10^{-5}$	$1.2x10^{-5}$	$1.6x10^{-6}$	$3.x10^{-8}$	-	-	-	-
^{60}Co	$2.2x10^{-7}$	$4.1x10^{-7}$	$4.4x10^{-7}$	$4.4x10^{-7}$	$4.4x10^{-7}$	$4.4x10^{-7}$	$4.4x10^{-7}$	$4.4x10^{-7}$
^{56}Mn	$1.9x10^{-3}$	$1.7x10^{-3}$	$1.5x10^{-3}$	$1.1x10^{-3}$	$8.5x10^{-4}$	$1.3x10^{-4}$	$3.0x10^{-6}$	-
^{65}Ni	$5.4x10^{-6}$	$4.7x10^{-6}$	$4.1x10^{-6}$	$3.1x10^{-6}$	$2.4x10^{-6}$	$3.4x10^{-7}$	$7.3x10^{-9}$	-
^{64}Cu	$4.3x10^{-5}$	$4.2x10^{-5}$	$4.1x10^{-5}$	$3.8x10^{-5}$	$3.7x10^{-5}$	$2.5x10^{-5}$	$1.2x10^{-5}$	$4.5x10^{-9}$
^{66}Cu	$7.2x10^{-4}$	$1.3x10^{-5}$	$2.1x10^{-7}$	-	-	-	-	-
^{28}Al	$3.5x10^{-2}$	$3.3x10^{-6}$	-	-	-	-	-	-
Total	$3.8x10^{-2}$	$1.7x10^{-3}$	$1.5x10^{-3}$	$1.2x10^{-3}$	$8.9x10^{-4}$	$1.6x10^{-4}$	$1.5x10^{-5}$	$4.4x10^{-7}$

Table A4.2 Dose rates at 1 m from the surface a 4000 cell array composed of NCM811 cells exposed to an incident fluence of $1x10^{12}$ n/cm^2. Activity distributed through the outermost 1 cm of the battery pack.

Isotope	0 h	0.5 h	1 h	2 h	3 h	10 h	24 h	168 h
^{60m}Co	$3.7x10^{-4}$	$5.1x10^{-5}$	$7.0x10^{-6}$	$1.3x10^{-7}$	$2.5x10^{-9}$	-	-	-
^{60}Co	$1.0x10^{-6}$	$1.8x10^{-6}$	$2.0x10^{-6}$	$2.0x10^{-6}$	$2.0x10^{-6}$	$2.0x10^{-6}$	$2.0x10^{-6}$	$2.0x10^{-6}$
^{56}Mn	$8.6x10^{-3}$	$7.5x10^{-3}$	$6.6x10^{-3}$	$5.0x10^{-3}$	$3.8x10^{-3}$	$5.8x10^{-4}$	$1.4x10^{-5}$	-
^{65}Ni	$2.4x10^{-5}$	$2.1x10^{-5}$	$1.8x10^{-5}$	$1.4x10^{-5}$	$1.1x10^{-5}$	$1.5x10^{-6}$	$3.3x10^{-8}$	-
^{64}Cu	$1.6x10^{-4}$	$1.6x10^{-4}$	$1.5x10^{-4}$	$1.4x10^{-4}$	$1.4x10^{-4}$	$9.3x10^{-5}$	$4.3x10^{-5}$	$1.7x10^{-8}$
^{66}Cu	$3.1x10^{-3}$	$5.4x10^{-5}$	$9.2x10^{-7}$	-	-	-	-	-
^{28}Al	$1.7x10^{-1}$	$1.6x10^{-5}$	$1.5x10^{-9}$	-	-	-	-	-
Total	$1.8x10^{-1}$	$7.8x10^{-3}$	$6.8x10^{-3}$	$5.2x10^{-3}$	$4.0x10^{-3}$	$6.8x10^{-4}$	$5.9x10^{-5}$	$2.0x10^{-6}$

Table A.4.3 Dose rates at the surface a 4000 cell array composed of NCM811 cells exposed to an incident fluence of $1x10^{12}$ n/cm^2. Activity distributed homogenously throughout the battery pack.

Isotope	0 h	0.5 h	1 h	2 h	3 h	10 h	24 h	168 h
^{60m}Co	$5.4x10^{-5}$	$7.4x10^{-6}$	$1.0x10^{-6}$	$1.9x10^{-8}$	-	-	-	-
^{60}Co	$1.5x10^{-7}$	$2.7x10^{-7}$	$2.8x10^{-7}$	$2.9x10^{-7}$	$2.9x10^{-7}$	$2.9x10^{-7}$	$2.9x10^{-7}$	$2.9x10^{-7}$
^{56}Mn	$1.2x10^{-3}$	$1.1x10^{-3}$	$9.4x10^{-4}$	$7.2x10^{-4}$	$5.5x10^{-4}$	$8.4x10^{-5}$	$1.9x10^{-6}$	-
^{65}Ni	$3.5x10^{-6}$	$3.1x10^{-6}$	$2.6x10^{-6}$	$2.0x10^{-6}$	$1.5x10^{-6}$	$2.2x10^{-7}$	$4.7x10^{-9}$	-
^{64}Cu	$2.3x10^{-5}$	$2.2x10^{-5}$	$2.2x10^{-5}$	$2.1x10^{-5}$	$1.9x10^{-5}$	$1.3x10^{-5}$	$6.2x10^{-6}$	$2.4x10^{-9}$
^{66}Cu	$4.5x10^{-4}$	$7.7x10^{-6}$	$1.3x10^{-7}$	-	-	-	-	-
^{28}Al	$2.5x10^{-2}$	$2.3x10^{-6}$	-	-	-	-	-	-
Total	2.6x10-2	$1.1x10^{-3}$	$9.7x10^{-4}$	$7.4x10^{-4}$	$5.7x10^{-4}$	$9.7x10^{-5}$	$8.4x10^{-6}$	$2.9x10^{-7}$

Table A4.4 Dose rates 1m from the surface of a 4000 cell array composed of NCM811 cells exposed to an incident fluence of $1x10^{12}$ n/cm^2. Activity distributed homogenously throughout the battery pack.

Isotope	**0 h**	**0.5 h**	**1 h**	**2 h**	**3 h**	**10 h**	**24 h**	**168 h**
^{60m}Co	$1.1x10^{-3}$	$1.5x10^{-4}$	$2.0x10^{-5}$	$3.7x10^{-7}$	$7.0x10^{-9}$	-	-	-
^{60}Co	$2.8x10^{-6}$	$5.2x10^{-6}$	$5.5x10^{-6}$	$5.6x10^{-6}$	$5.6x10^{-6}$	$5.6x10^{-6}$	$5.6x10^{-6}$	$5.6x10^{-6}$
^{65}Ni	$4.6x10^{-5}$	$4.0x10^{-5}$	$3.5x10^{-5}$	$2.7x10^{-5}$	$2.0x10^{-5}$	$2.9x10^{-6}$	$6.3x10^{-8}$	-
^{64}Cu	$3.6x10^{-4}$	$3.5x10^{-4}$	$3.4x10^{-4}$	$3.2x10^{-4}$	$3.0x10^{-4}$	$2.1x10^{-4}$	$9.6x10^{-5}$	$3.7x10^{-8}$
^{66}Cu	$6.3x10^{-3}$	$1.1x10^{-4}$	$1.9x10^{-6}$	-	-	-	-	-
^{28}Al	$2.9x10^{-1}$	$2.8x10^{-5}$	$2.6x10^{-9}$	-	-	-	-	-
Total	$3.0x10^{-1}$	$6.7x10^{-4}$	$4.0x10^{-4}$	$3.5x10^{-4}$	$3.3x10^{-4}$	$2.1x10^{-4}$	$1.0x10^{-4}$	$5.6x10^{-6}$

Table A4.5 Dose rates at the surface a 4000 cell array composed of NCA cells exposed to an incident fluence of $1x10^{12}$ n/cm^2. Activity distributed through the outermost 1 cm of the battery pack.

Isotope	**0 h**	**0.5 h**	**1 h**	**2 h**	**3 h**	**10 h**	**24 h**	**168 h**
^{60m}Co	$1.3x10^{-4}$	$1.7x10^{-5}$	$2.4x10^{-6}$	$4.5x10^{-8}$	-	-	-	-
^{60}Co	$3.3x10^{-7}$	$6.1x10^{-7}$	$6.5x10^{-7}$	$6.5x10^{-7}$	$6.5x10^{-7}$	$6.5x10^{-7}$	$6.5x10^{-7}$	$6.5x10^{-7}$
^{65}Ni	$5.4x10^{-6}$	$4.7x10^{-6}$	$4.1x10^{-6}$	$3.1x10^{-6}$	$2.4x10^{-6}$	$3.4x10^{-7}$	$7.3x10^{-9}$	-
^{64}Cu	$4.3x10^{-5}$	$4.2x10^{-5}$	$4.0x10^{-5}$	$3.8x10^{-5}$	$3.6x10^{-5}$	$2.5x10^{-5}$	$1.2x10^{-5}$	$4.5x10^{-9}$
^{66}Cu	$7.4x10^{-4}$	$1.3x10^{-5}$	$2.2x10^{-7}$	-	-	-	-	-
^{28}Al	$3.4x10^{-2}$	$3.2x10^{-6}$	-	-	-	-	-	-
Total	$3.5x10^{-2}$	$8.0x10^{-5}$	$4.8x10^{-5}$	$4.2x10^{-5}$	$3.9x10^{-5}$	$2.6x10^{-5}$	$1.2x10^{-5}$	$6.5x10^{-7}$

Table A4.6 Dose rates at 1 m from the surface a 4000 cell array composed of NCA cells exposed to an incident fluence of $1x10^{12}$ n/cm^2. Activity distributed through the outermost 1 cm of the battery pack.

Isotope	0 h	0.5 h	1 h	2 h	3 h	10 h	24 h	168 h
^{60m}Co	$5.7x10^{-4}$	$7.7x10^{-5}$	$1.1x10^{-5}$	$2.0x10^{-7}$	$3.8x10^{-9}$	-	-	-
^{60}Co	$1.5x10^{-6}$	$2.9x10^{-6}$	$3.0x10^{-6}$	$3.1x10^{-6}$	$3.1x10^{-6}$	$3.1x10^{-6}$	$3.1x10^{-6}$	$3.1x10^{-6}$
^{65}Ni	$2.6x10^{-5}$	$2.2x10^{-5}$	$1.9x10^{-5}$	$1.5x10^{-5}$	$1.1x10^{-5}$	$1.6x10^{-6}$	$3.5x10^{-8}$	-
^{64}Cu	$1.7x10^{-4}$	$1.6x10^{-4}$	$1.6x10^{-4}$	$1.5x10^{-4}$	$1.4x10^{-4}$	$9.6x10^{-5}$	$4.5x10^{-5}$	$1.7x10^{-8}$
^{66}Cu	$3.3x10^{-3}$	$5.7x10^{-5}$	$9.9x10^{-7}$	-	-	-	-	-
^{28}Al	$1.7x10^{-1}$	$1.6x10^{-5}$	$1.5x10^{-9}$	-	-	-	-	-
Total	$1.8x10^{-1}$	$3.4x10^{-4}$	$1.9x10^{-4}$	$1.7x10^{-4}$	$1.5x10^{-4}$	$1.0x10^{-4}$	$4.8x10^{-5}$	$3.1x10^{-6}$

Table A4.7 Dose rates at the surface a 4000 cell array composed of NCA cells exposed to an incident fluence of $1x10^{12}$ n/cm^2. Activity distributed homogenously throughout the battery pack.

Isotopes	**0 h**	**0.5 h**	**1 h**	**2 h**	**3 h**	**10 h**	**24 h**	**168 h**
^{60m}Co	$8.3x10^{-5}$	$1.1x10^{-5}$	$1.6x10^{-6}$	$2.9x10^{-8}$	-	-	-	-
^{60}Co	$2.2x10^{-7}$	$4.1x10^{-7}$	$4.4x10^{-7}$	$4.4x10^{-7}$	$4.4x10^{-7}$	$4.4x10^{-7}$	$4.4x10^{-7}$	$4.4x10^{-7}$
^{65}Ni	$3.7x10^{-6}$	$3.2x10^{-6}$	$2.8x10^{-6}$	$2.1x10^{-6}$	$1.6x10^{-6}$	$2.3x10^{-7}$	$5.0x10^{-9}$	-
^{64}Cu	$2.4x10^{-5}$	$2.3x10^{-5}$	$2.2x10^{-5}$	$2.1x10^{-5}$	$2.0x10^{-5}$	$1.4x10^{-5}$	$6.4x10^{-6}$	$2.5x10^{-9}$
^{66}Cu	$4.8x10^{-4}$	$8.3x10^{-6}$	$1.4x10^{-7}$	-	-	-	-	-
^{28}Al	$2.4x10^{-2}$	$2.3x10^{-6}$	-	-	-	-	-	-
Total	$2.5x10^{-2}$	$4.9x10^{-5}$	$2.7x10^{-5}$	$2.4x10^{-5}$	$2.2x10^{-5}$	$1.4x10^{-5}$	$6.8x10^{-6}$	$4.4x10^{-7}$

Table A4.8 Dose rates 1m from the surface of a 4000 cell array composed of NCA cells exposed to an incident fluence of $1x10^{12}$ n/cm^2. Activity distributed homogenously throughout the battery pack.

Isotope	0 h	0.5 h	1 h	2 h	3 h	10 h	24 h	168 h
^{59}Fe	$6.7x10^{-8}$	$6.7x10^{-8}$	$6.7x10^{-8}$	$6.7x10^{-8}$	$6.7x10^{-8}$	$6.7x10^{-8}$	$6.6x10^{-8}$	$6.0x10^{-8}$
^{32}P	-	-	-	-	-	-	-	-
^{64}Cu	$5.5x10^{-4}$	$5.4x10^{-4}$	$5.2x10^{-4}$	$4.9x10^{-4}$	$4.7x10^{-4}$	$3.2x10^{-4}$	$1.5x10^{-4}$	$5.7x10^{-8}$
^{66}Cu	$9.5x10^{-3}$	$1.6x10^{-4}$	$2.8x10^{-6}$	-	-	-	-	-
^{28}Al	$3.7x10^{-1}$	$3.5x10^{-5}$	$3.3x10^{-9}$	-	-	-	-	-
Total	$3.8x10^{-1}$	$7.4x10^{-4}$	$5.3x10^{-4}$	$4.9x10^{-4}$	$4.7x10^{-4}$	$3.2x10^{-4}$	$1.5x10^{-4}$	$1.2x10^{-7}$

Table A4.9 Dose rates at the surface a 4000 cell array composed of LFP cells exposed to an incident fluence of $1x10^{12}$ n/cm^2. Activity distributed through the outermost 1 cm of the battery pack.

Isotope	0 h	0.5 h	1 h	2 h	3 h	10 h	24 h	168 h
^{59}Fe	$7.8x10^{-9}$	$7.8x10^{-9}$	$7.8x10^{-9}$	$7.8x10^{-9}$	$7.8x10^{-9}$	$7.8x10^{-9}$	$7.7x10^{-9}$	$7.0x10^{-9}$
^{32}P	-	-	-	-	-	-	-	-
^{64}Cu	$6.6x10^{-5}$	$6.4x10^{-5}$	$6.3x10^{-5}$	$5.9x10^{-5}$	$5.6x10^{-5}$	$3.8x10^{-5}$	$1.8x10^{-5}$	$6.9x10^{-9}$
^{66}Cu	$1.1x10^{-3}$	$1.9x10^{-5}$	$3.3x10^{-7}$	-	-	-	-	-
^{28}Al	$4.2x10^{-2}$	$3.9x10^{-6}$	-	-	-	-	-	-
Total	$4.3x10^{-2}$	$8.8x10^{-5}$	$6.3x10^{-5}$	$5.9x10^{-5}$	$5.6x10^{-5}$	$3.8x10^{-5}$	$1.8x10^{-5}$	$1.4x10^{-8}$

Table A4.10 Dose rates 1 m from the surface of a 4000 cell array composed of LFP cells exposed to an incident fluence of $1x10^{12}$ n/cm^2. Activity distributed through the outermost 1 cm of the battery pack.

Isotope	0 h	0.5 h	1 h	2 h	3 h	10 h	24 h	168 h
^{59}Fe	$3.4x10^{-8}$	$3.4x10^{-8}$	$3.4x10^{-8}$	$3.4x10^{-8}$	$3.4x10^{-8}$	$3.3x10^{-8}$	$3.3x10^{-8}$	$3.0x10^{-8}$
^{32}P	-	-	-	-	-	-	-	-
^{64}Cu	$2.6x10^{-4}$	$2.5x10^{-4}$	$2.4x10^{-4}$	$2.3x10^{-4}$	$2.2x10^{-4}$	$1.5x10^{-4}$	$6.9x10^{-5}$	$2.7x10^{-8}$
^{66}Cu	$4.9x10^{-3}$	$8.5x10^{-5}$	$1.5x10^{-6}$	-	-	-	-	-
^{28}Al	$2.1x10^{-1}$	$1.9x10^{-5}$	$1.8x10^{-9}$	-	-	-	-	-
Total	$2.1x10^{-1}$	$3.5x10^{-4}$	$2.4x10^{-4}$	$2.3x10^{-4}$	$2.2x10^{-4}$	$1.5x10^{-4}$	$6.9x10^{-5}$	$5.7x10^{-8}$

Table A4.11 Dose rates at the surface a of 4000 cell array composed of LFP cells exposed to an incident fluence of $1x10^{12}$ n/cm^2. Activity distributed homogenously throughout the battery pack.

Isotope	0 h	0.5 h	1 h	2 h	3 h	10 h	24 h	168 h
^{59}Fe	$5.1x10^{-9}$	$5.1x10^{-9}$	$5.1x10^{-9}$	$5.1x10^{-9}$	5.8x10-9	$5.5x10^{-9}$	$5.0x10^{-9}$	$4.6x10^{-9}$
^{32}P	-	-	-	-	-	-	-	-
^{64}Cu	$3.6x10^{-5}$	$3.5x10^{-5}$	$3.4x10^{-5}$	$3.2x10^{-5}$	$3.1x10^{-5}$	$2.1x10^{-5}$	$9.7x10^{-6}$	$3.7x10^{-9}$
^{66}Cu	$7.1x10^{-4}$	$1.2x10^{-5}$	$2.1x10^{-7}$	-	-	-	-	-
^{28}Al	$2.9x10^{-2}$	$2.7x10^{-6}$	-	-	-	-	-	-
Total	$3.0x10^{-2}$	$5.0x10^{-5}$	$3.4x10^{-5}$	$3.2x10^{-5}$	$3.1x10^{-5}$	$2.1x10^{-5}$	$9.7x10^{-6}$	$8.3x10^{-9}$

Table A4.12 Dose rates 1 m from the surface a of 4000 cell array composed of LFP cells exposed to an incident fluence of $1x10^{12}$ n/cm^2. Activity distributed homogenously throughout the battery pack.

APPENDIX 5

Neutron Irradiation of Disk Sources

When an object of interest has large dimensions, it may be impossible to use it as such for a Geant4 input. A typical such case is a neutron exposure of ground over large distances. The computational burden of this geometry may be too heavy. Then the following approximative approach may be useful.

Let us first consider a small object exposed to a neutron beam. This creates an activity of a Bq for a nuclide of interest. The doserate is calculated simply by multiplication, if we know the doserate conversion factor CF in units of $Gy.h^{-1}$ per Bq. Such factors are tabulated for radiation protection purposes for many point sources, but these are not relevant for complex geometries. However, they may still be useful for estimating the upper or lower limit of the true dose rate. Geant4 provides means to calculate CF factors for complex geometries. The software takes care of nuclide properties, such as the yield of certain gamma lines.

The doserate estimation process is slightly more complex if we have a very large area of interest. Let A be the area of a disk with thickness w. Instead of simulating the total area we decide to shoot the target with a beam of neutrons having a unit area (1 m^2). The simulation geometry should contain the total area A, or if it is very large, a relevant fraction of it. This arrangement takes care of the scattering of the neutrons, i.e., some atoms are formed outside the beam. Let a_u be the total activity of the atoms of interest generated by the unit area beam. Then the total activity a_A in the disk is

$$a_A = A a_u$$

This activity is slightly too large because escape scattering from the edges is omitted. However, the overestimation is typically small, a few percentages.

For each nuclide of interest, it is useful to calculate a geometry-specific dose conversion factor, CF, in units of $Gy.h^{-1}$ per Bq. In practice the Geant4 input could be an activity of 1 MBq for t seconds in a geometry where we have a tissue-equivalent sphere (1 kg) in location of interest, typically in the centre of the disk at a distance of 1 m from the surface. Then the doserate is

$$D = a_A CF \quad [\mathrm{Bq}][\mathrm{Gy.h^{-1}.Bq^{-1}}] = [\mathrm{Gy.h^{-1}}]$$

For unit exposure of the target

$$D = A a_u CF \quad [\mathrm{m^2}][\mathrm{Bq.m^{-2}}][\mathrm{Gy.h^{-1}.Bq^{-1}}] = [\mathrm{Gy.h^{-1}}]$$

The doserate simulation is a two-step Geant4 process and is thus vulnerable to mistakes. To avoid errors, great care must be taken in reporting the relevant quantities.

The computation of CF must consider the depth distribution of the atoms in the ground. The Geant4 simulations provide the coordinates of every neutron capture reaction. This information allows to calculate the depth distribution which then can be discretized for further simulation purposes. For example, a continuous atom distribution in sand (w = 40 cm) can be approximated with a few layers having a constant number of atoms (Figure A5.1).

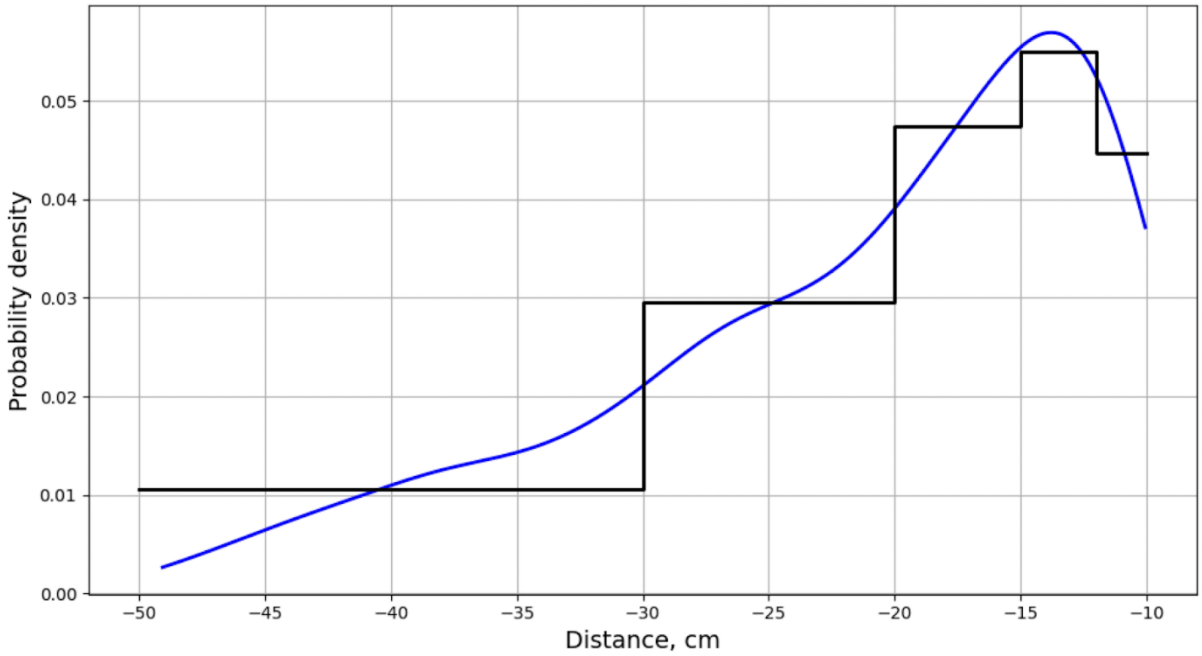

Figure A5.1. Depth distribution and its approximation of ^{24}Na atoms in a sand layer of 10 – 50 cm under an asphalt road of 10 cm in thickness. Na concentration is 1.7 % (PNNL material 306).

When the distribution of Na atoms in the ground is known, the dose rate conversion factor can be calculated. The simulations were performed for a disk having a radius of 5 m containing 10 cm asphalt and 40 cm sand. The dose rate conversion factors were [7.89, 8.01, 8.68] x10^{-13} Gy/h per Bq/m^2 for Na concentrations of [0.3, 1.7, 3] %. For comparison, another road structure was analyzed having 2 cm asphalt and 10 cm sand. In this geometry the dose rate conversion factor is 1.63 x10^{-12} Gy/h per Bq/m^2.

APPENDIX 6

Bremsstrahlung of High-energy Beta Emitters

Bremsstrahlung (BS) is slowing-down radiation being electromagnetic radiation produced by fast electrons when they interact with the Coulomb field of the nucleus. The electron energy loss is transformed to a continuum of photons (Figure A6.1). In a gamma spectrum BS raises the general background making the peak analysis more difficult.

Bremsstrahlung yield

Bremsstrahlung yield is defined as the fraction of an electron's kinetic energy that is converted into BS photons as the electron slows down to rest in a material. For a low-Z material like aluminium (Z=13), this radiative yield is small at low electron energies but increases with electron energy, being significant above 1 MeV. BS is very important in high-Z materials, such as Pb (Z=82).

The Bremsstrahlung yield can be estimated roughly by "Turner" equation

$$\mathrm{Y} = \frac{kZT}{1 + kZT} \approx kZT$$

where Z is the atomic number of the shielding material, T is the kinetic energy of a beta particle in MeV and k is a constant of $6\text{x}10^{-4}$. Therefore, the response is linear in our domain of interest (3 MeV). The NMC811, NCA and LFP batteries contain materials, such as Ni, Mn, Co, Cu, and Fe which have Z in the range of 25 – 29. See Figure A6.2 for the expected BS yield.

The BS yield is very low for low energy electrons in the battery materials (Figure A6.2). Monoenergetic electrons convert only a small fraction of their energy into BS X-rays at 100 keV (about 0.1% or less), but the BS fraction increases with energy, reaching about 1 - 2 % at 1 MeV and a 2 - 5 % at 3 MeV.

The battery materials contain four beta emitters - ^{28}Al, ^{65}Ni, ^{66}Cu, and ^{32}P - which decay by emitting high-energy electrons (for the nuclide data, see Appendix 7). Only the LFP battery contains phosphorus. In thermal neutron flux the main isotope ^{31}P is converted into ^{32}P which is a pure beta emitter.

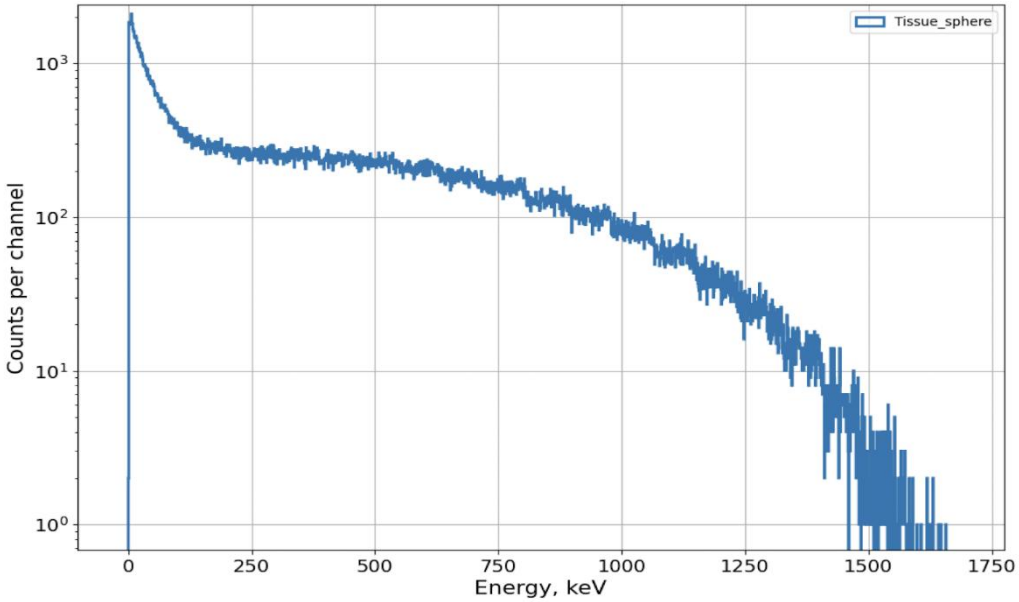

Figure A6.1. ^{32}P Bremsstrahlung energy spectrum in tissue which is in contact with an LFP battery (Geant4 simulation).

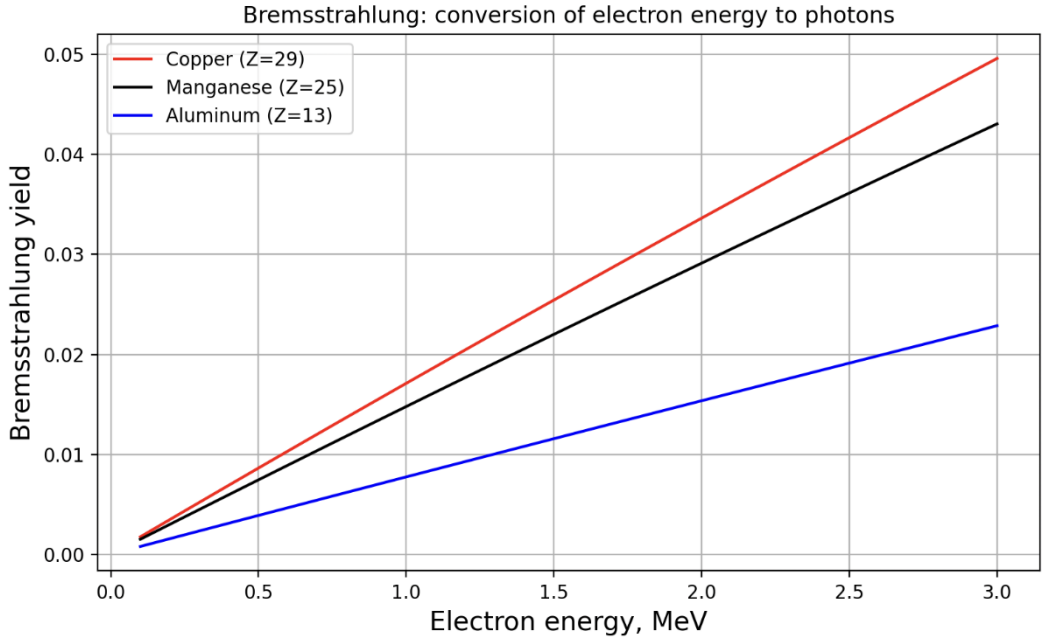

Figure A6.2. Bremsstrahlung yield in some materials contained in batteries.

Bremsstrahlung simulations for testing Geant4

For testing the capability of Geant4 to track electrons and BS generated in the slowing-down process, a simple geometry was used for the simulations. A source emitting mono-energetic electrons was placed in the origo, and it was surrounded by hollow spheres containing aluminium, PE and a thick NaI detector stopping all photons. The thickness of the aluminium layer was chosen to match the electron range in aluminium (10 % larger); this range varies much depending on the energy of the electron. The purpose of PE was to stop any remaining electron to pass through towards the NaI detector. Therefore, in this design the NaI detector records BS only. The drawback of this test is that a tiny fraction of BS photons is captured by aluminium.

The simulation results are shown in Figures A6.3 and A6.4. Most of the events take place in the detector “inner Aluminium”. The role of PE is negligible showing that almost all electrons were stopped in aluminium. As expected, the results of the yield test are an underestimation as compared with the NIST Estar data but nevertheless they give confidence on the BS simulation capability of Geant4.

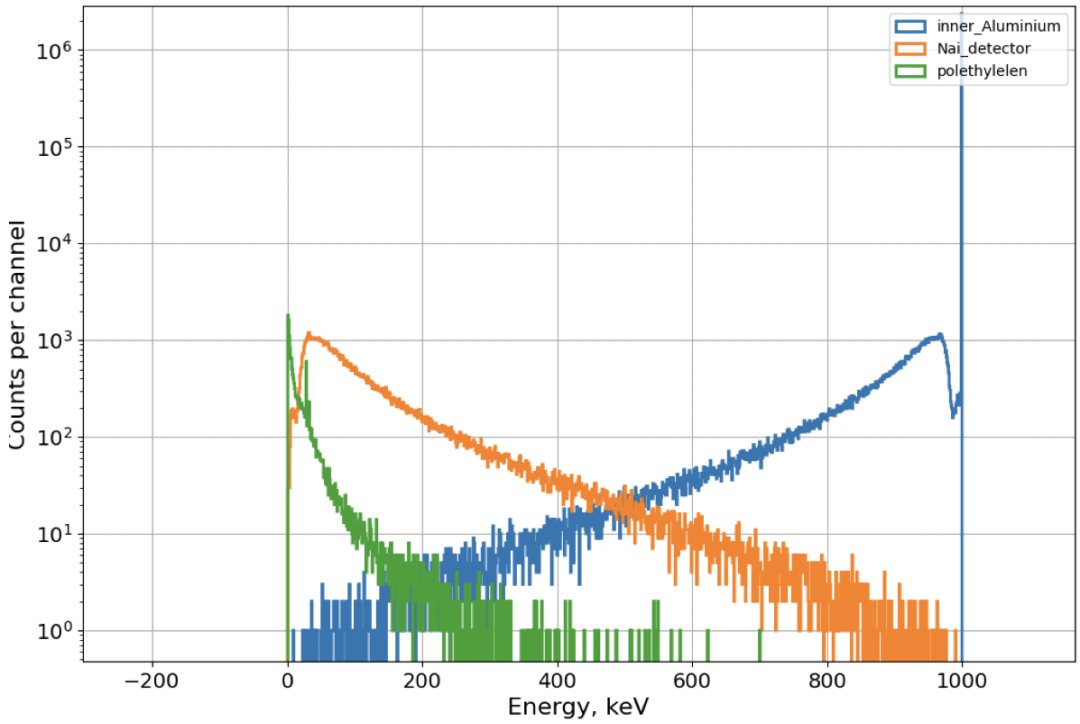

Figure A6.3. Energy spectra generated by 1 MeV electrons moving in aluminium (point source in a sphere).

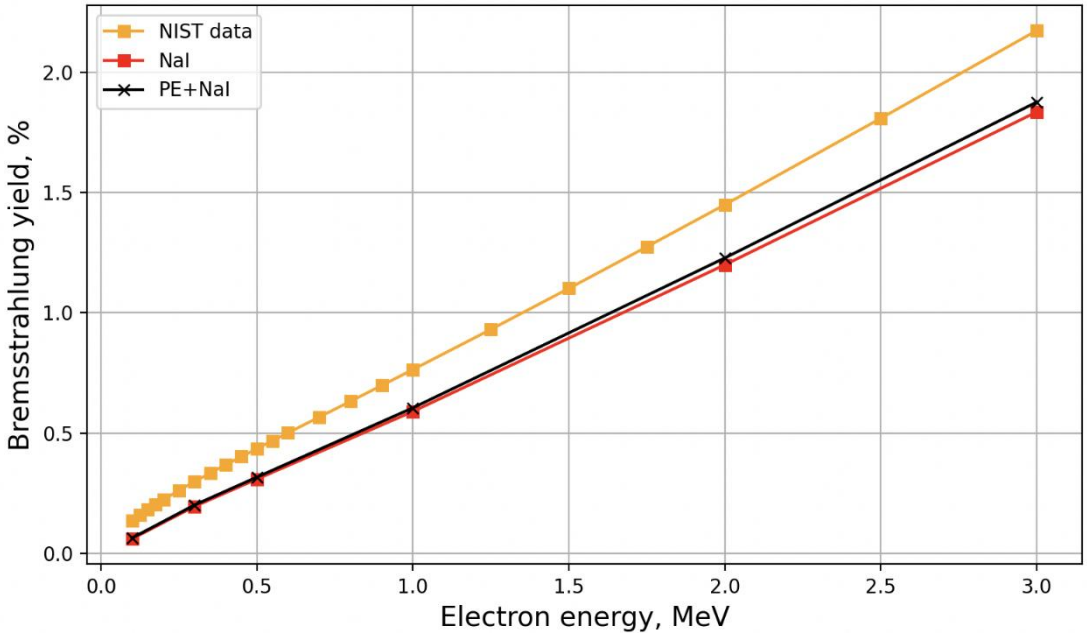

Figure A6.4. Conversion of electron energy to Bremsstrahlung; comparison of Geant4 simulations with NIST data in aluminium (point source in a sphere).

Geant4 simulations for battery packs

Geant4 simulations were performed to assess the dose contribution of gamma emitters created in NCM, NCA and LFP batteries after a thermal neutron exposure to fluence of 10^{12} n/cm2. After one hour, in the NCM battery the doserate is dominated by the gamma emitters of ^{56}Mn, ^{64}Cu and ^{60}Co, in the NCA battery by ^{64}Cu and ^{60}Co and in LFP battery by ^{64}Cu and BS from ^{32}P. After one week, ^{60}Co is the most significant nuclide in NCM and NCA batteries whereas in LFP it is ^{32}P.

Aluminium-28 is in important radionuclide during the first half an hour in all batteries. Nickel-65 and ^{66}Cu have no significant dose contribution. These three nuclides are strong beta emitters. Therefore, it is worthwhile to study in detail their BS contribution. For ^{32}P this is mandatory, because it is a pure beta emitter.

Further Geant4 simulations were performed to understand the BS dose contribution of the high-energy beta emitters. Appendix 8 contains dose conversion factors in units of Gy/h per Bq for gamma radiation and BS. Below is a summary of these results. It turns out that the nuclide-specific dose conversion factors are almost constant between different batteries for a given measurement geometry. The BS dose fraction varies between 5 – 23 % for ^{28}Al and 3 – 12 % for ^{65}Ni. These values are small as compared with other uncertainties in dose assessment, and it is fully justified to ignore them. For ^{66}Cu the BS dose fractions are large, 41 – 76 %. However, ^{66}Cu is a short-lived nuclide (half-life 5.1 min); thus, neither the gamma radiation nor the BS of ^{66}Cu is of importance in a time scale of hours.

The percentage of Bremsstrahlung from total doserate in different batteries and measurement geometries is listed below.

Case 1	All activity in the top 1 cm layer of the battery
Case 2	All activity evenly distributed in the battery
1 m	Tissue-equivalent detector 1 m away from the battery
contact	Tissue-equivalent detector in contact with the battery

BS % in Case 1 – 1m

Isotope	NCM811	NCA	LFP
^{28}Al	22.5	22.8	23.1
^{66}Cu	75.2	75.6	76.0
^{65}Ni	12.3	12.6	-

BS % in Case 1 – contact

Isotope	NCM811	NCA	LFP
^{28}Al	15.4	15.5	15.6
^{66}Cu	67.1	67.3	67.8
^{65}Ni	9.7	9.8	-

BS % in Case 2 – 1m

Isotope	NCM811	NCA	LFP
^{28}Al	7.2	7.1	7.4
^{66}Cu	47.3	47.1	47.6
^{65}Ni	3.9	3.8	-

BS % in Case 2 – contact

Isotope	NCM811	NCA	LFP
^{28}Al	5.5	5.4	5.7
^{66}Cu	41.7	41.2	42.1
^{65}Ni	3.5	3.4	-

APPENDIX 7

Nuclide Data of High-energy Beta Emitters

The key nuclear data of relevant beta emitters for the battery packs are listed below (data from IAEA Nuclear Data Section). The continuous energy distribution of the emitted beta particles is discretized to create a probability density function (pdf) for Geant4 input to calculate the dose rate caused by Bremsstrahlung.

13-Al-28 Aluminium

Half-life 2.245(2) m
Decay constant 5.146 E-3 (4) 1/s
Specific activity 1.1075 E20 (9) Bq/g

Decay radiations

β-

Avg En. [keV]	Intensity %	Decay En. [keV] %	
1241.80	99.99 (1)	(2863.22)	(CA)

γ

Energy [keV]	Intensity %
1778.987 (15)	100 (0)

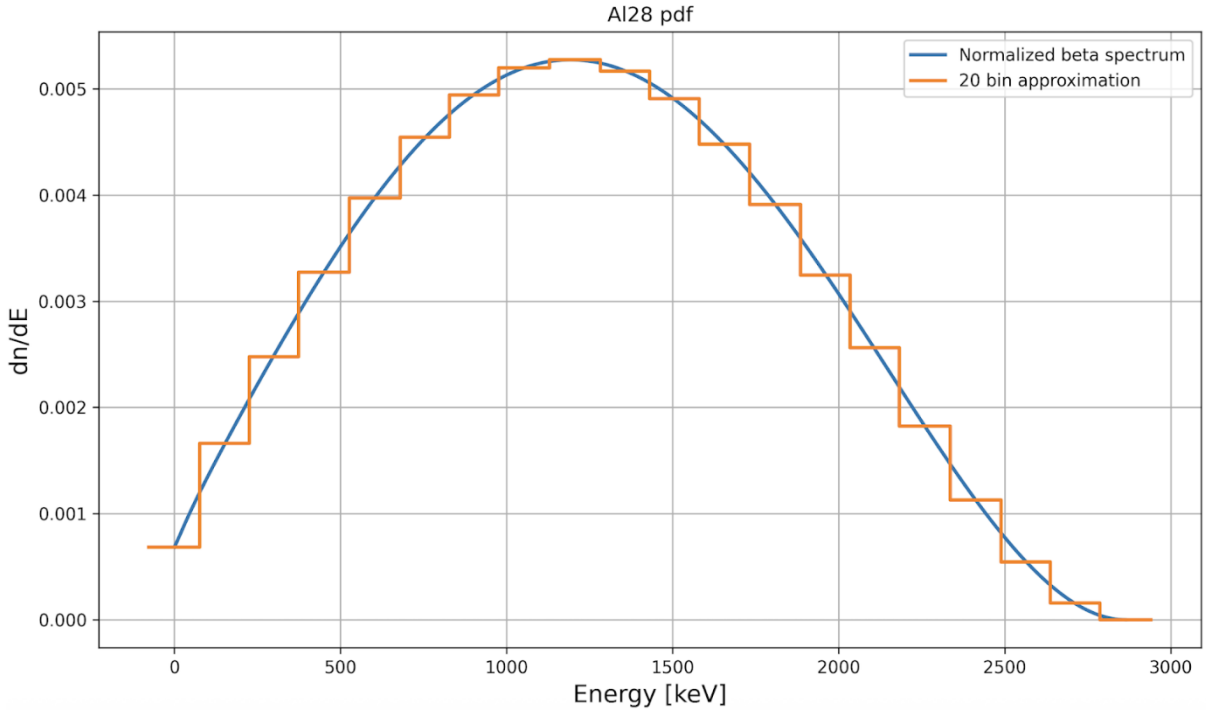

29-Cu-66 Copper

Half-life 5.120(14) m
Decay constant 2.256 E-3 (6) 1/s
Specific activity 2.061 E19 (5) Bq/g

Decay radiations

β-

Avg En. [keV]	Intensity %	Decay En. [keV] %
1112.1 (6)	90.77 (9)	2630 (20)
628.1 (6)	9.01 (9)	1590 (30)

γ

Energy [keV]	Intensity %
1039.2 (2)	9.23 (9)
833.0 (10)	0.220 (4)

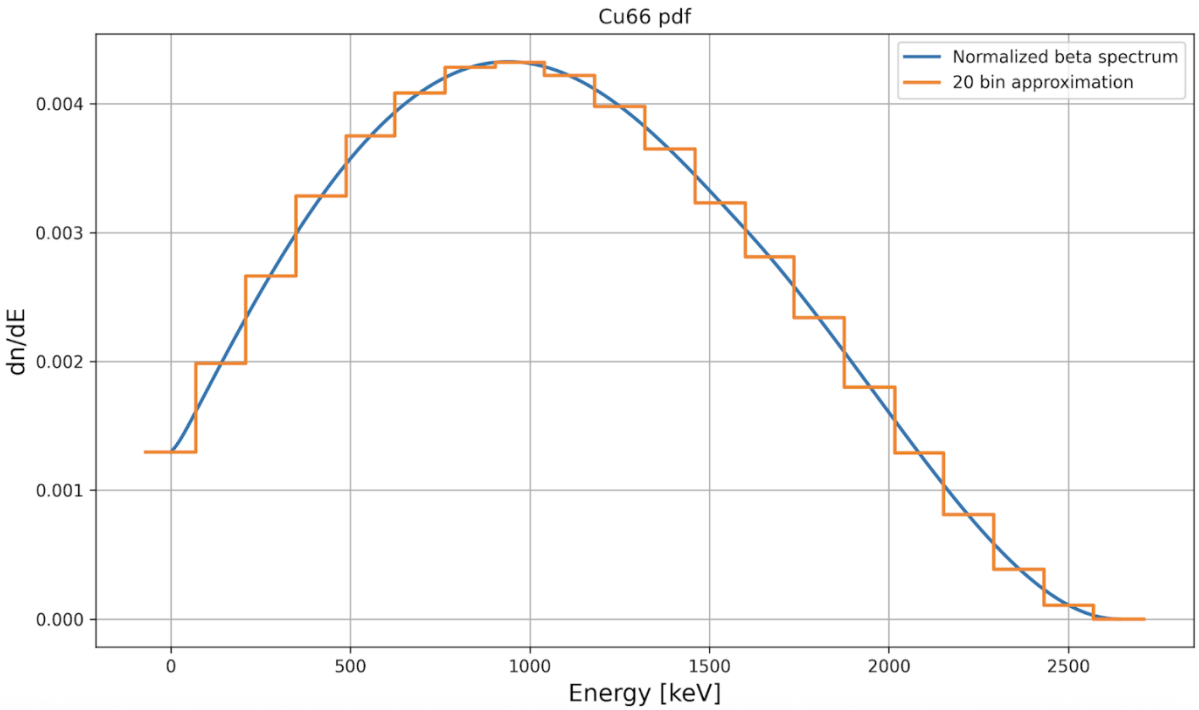

28-Ni-65 Nickel

Half-life 2.5175(5) h
Decay constant 7.6481 E-5 (15) 1/s
Specific activity 7.0935 E17 (14) Bq/g

Decay radiations

β-

Avg En. [keV]	Intensity %	Decay En. [keV] %
875.4 (6)	60.0 (3)	2140 (10)
220.5 (5)	28.4 (2)	650 (30)
371.7 (5)	10.18 (13)	1020 (25)
165.8 (5)	0.89 (2)	(514.5) (CA)

γ

Energy [keV]	Intensity %
1481.84 (5)	23.59 (14)
1115.53. (4)	15.43 (13)
366.27 (3)	4.81 (6)
1623.42. (6)	0.498 (14)
1724.92. (6)	0.399 (12)
507.9 (1)	0.293 (5)

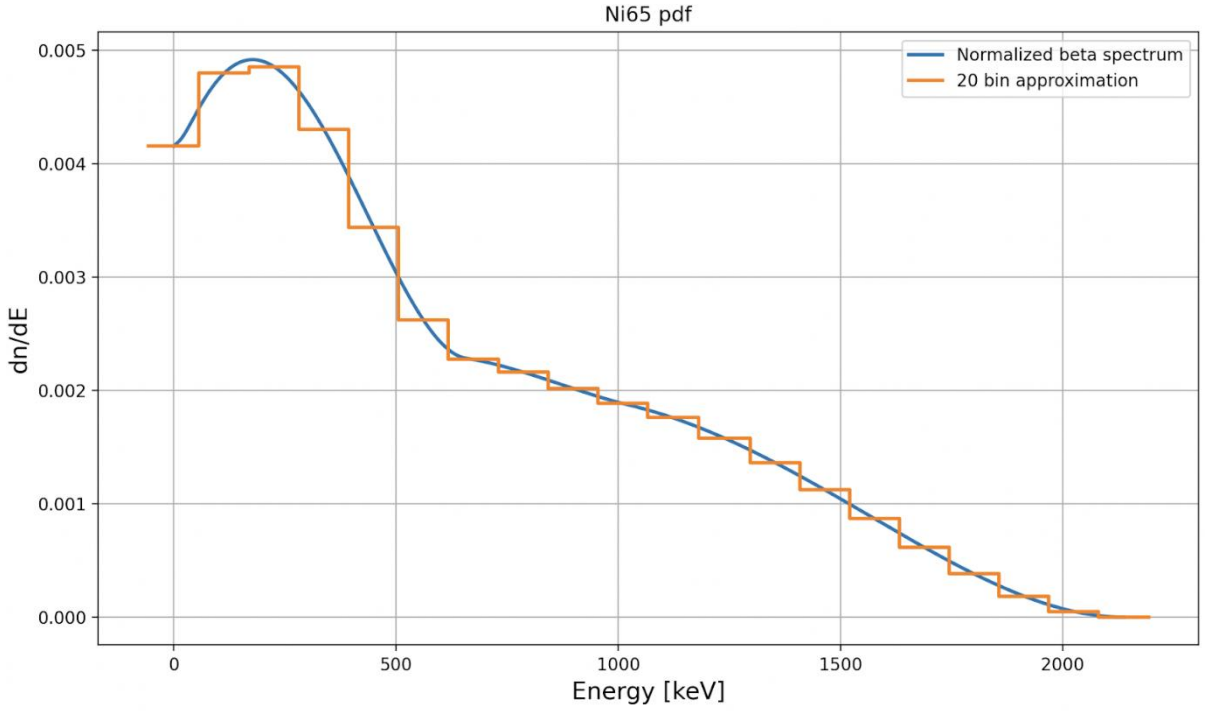

15-P-32 Phosphorus

Half-life 14.268(5) d
Decay constant 5.6227 E-7 (19) 1/s
Specific activity 1.0590 E16 (3) Bq/g

Decay radiations

β-

Avg En. [keV]	Intensity %	Decay En. [keV] %	
695.03	100. (0)	(1710.63)	(CA)

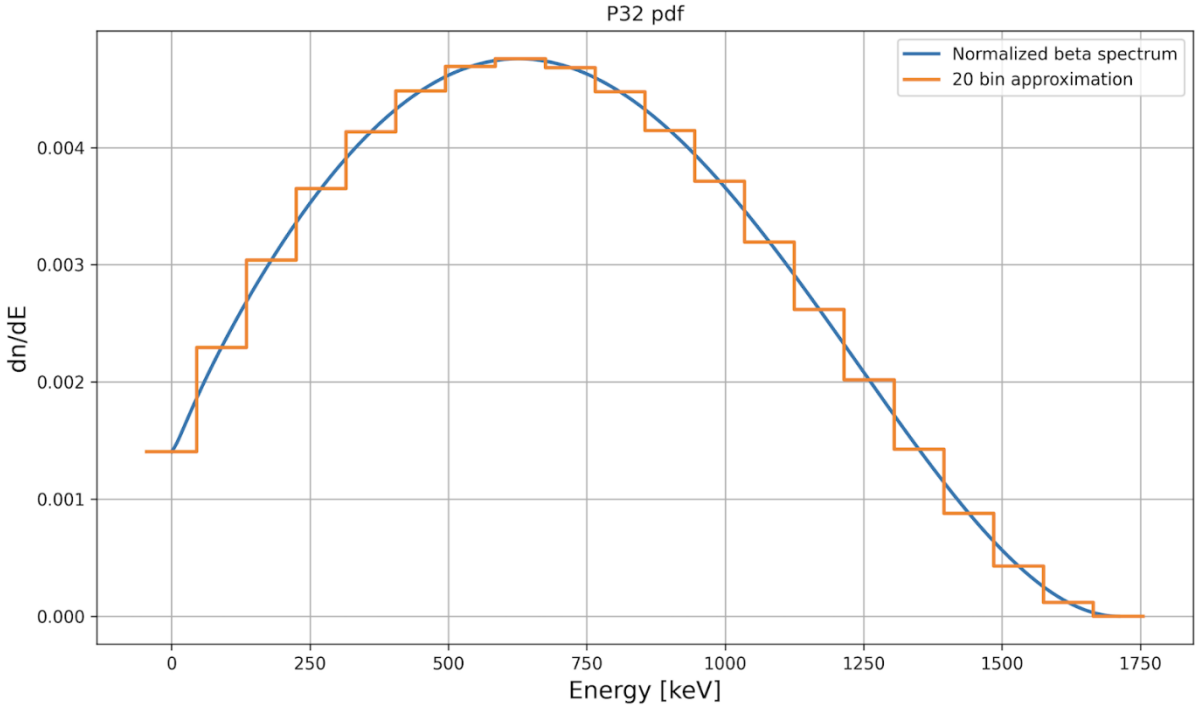

APPENDIX 8

Dose Conversion Factors of High-energy Beta Emitters - Geant4 Simulation Results

Case 1 All activity in the top 1 cm layer of the battery
Case 2 All activity evenly distributed in the battery
1 m Tissue-equivalent detector 1 m away from the battery
contact Tissue-equivalent detector in contact with the battery

Table A8.1 NCM811 battery. Dose conversion factors, Gy/h per Bq.

Case1 – 1 m

Isotope	Gamma radiation	Bremsstrahlung	Percentage B/(B+G)
^{28}Al	1.31e-13	3.80e-14	22.5
^{66}Cu	7.82e-15	2.37e-14	75.2
^{65}Ni	4.35e-14	6.10e-15	12.3

Case1 – contact

Isotope	Gamma radiation	Bremsstrahlung	Percentage B/(B+G)
^{28}Al	1.14e-12	2.07e-13	15.4
^{66}Cu	6.63e-14	1.35e-13	67.1
^{65}Ni	3.71e-13	3.97e-14	9.7

Case2 – 1 m

Isotope	Gamma radiation	Bremsstrahlung	Percentage B/(B+G)
^{28}Al	9.12e-14	7.10e-15	7.2
^{66}Cu	4.86e-15	4.36e-15	47.3
^{65}Ni	2.82e-14	1.14e-15	3.9

Case2 – contact

Isotope	Gamma radiation	Bremsstrahlung	Percentage B/(B+G)
^{28}Al	6.40e-13	3.75e-14	5.5
^{66}Cu	3.38e-14	2.42e-14	41.7
^{65}Ni	1.97e-13	7.10e-15	3.5

Table A8.2 NCA battery. Dose conversion factors, Gy/h per Bq.

Case1 - 1 m

Isotope	Gamma radiation	Bremsstrahlung	Percentage B/(B+G)
^{28}Al	1.32e-13	3.89e-14	22.8
^{66}Cu	7.89e-15	2.44e-14	75.6
^{65}Ni	4.34e-14	6.28e-15	12.6

Case1 – Contact

Isotope	Gamma radiation	Bremsstrahlung	Percentage B/(B+G)
^{28}Al	1.15e-12	2.11e-13	15.5
^{66}Cu	6.71e-14	1.38e-13	67.3
^{65}Ni	3.72e-13	4.06e-14	9.8

Case2 – 1 m

Isotope	Gamma radiation	Bremsstrahlung	Percentage B/(B+G)
^{28}Al	9.52e-14	7.24e-15	7.1
^{66}Cu	5.12e-15	4.56e-15	47.1
^{65}Ni	2.96e-14	1.18e-15	3.8

Case2 – contact

Isotope	Gamma radiation	Bremsstrahlung	Percentage B/(B+G)
^{28}Al	6.69e-13	3.83e-14	5.4
^{66}Cu	3.54e-14	2.48e-14	41.2
^{65}Ni	2.06e-13	7.30e-15	3.4

Table A8.3. LFP battery. Dose conversion factors, Gy/h per Bq.

Case1 - 1 m

Isotope	Gamma radiation	Bremsstrahlung	Percentage B/(B+G)
^{28}Al	1.30e-13	3.90e-14	23.1
^{66}Cu	7.74e-15	2.45e-14	76.0
^{32}P	0	8.57e-15	100

Case1 – Contact

Isotope	Gamma radiation	Bremsstrahlung	Percentage B/(B+G)
^{28}Al	1.15e-12	2.13e-13	15.6
^{66}Cu	6.58e-14	1.39e-13	67.8
^{32}P	0	6.31e-14	100

Case2 – 1 m

Isotope	Gamma radiation	Bremsstrahlung	Percentage B/(B+G)
^{28}Al	9.06e-14	7.23e-15	7.4
^{66}Cu	4.88e-15	4.44e-15	47.6
^{32}P	0	1.58e-15	100

Case2 – contact

Isotope	Gamma radiation	Bremsstrahlung	Percentage B/(B+G)
^{28}Al	6.40e-13	3.84e-14	5.7
^{66}Cu	3.41e-14	2.48e-14	42.1
^{32}P	0	1.12e-14	100

APPENDIX 9

Production of ^{60m}Co and ^{60}Co by Thermal Neutrons

Cobalt-60 is a common radionuclide with a long half-life 5.27 y. When it is produced in thermal neutron flux, also ^{60m}Co is produced. It has a half-life of 10.47 min. The isomeric state of ^{60m}Co decays in two ways: IT and β- (Figure A9.1). The former emits 58.6 keV photons (2.07 %) whereas the latter gives mainly 1332.5 keV photons (0.25 %); two other photons are generated with even smaller yield. We tend to assume that the branch is not significant, and indeed this is so in long time scale. But during the first hour, decay of ^{60m}Co is dominating the high-energy radiation exposure. The reason is the short half-life. Cobalt-60 is responsible for the long-term contamination, but ^{60m}Co is more dangerous at the early phase after a nuclear blast. The following analysis is intended to quantify this statement.

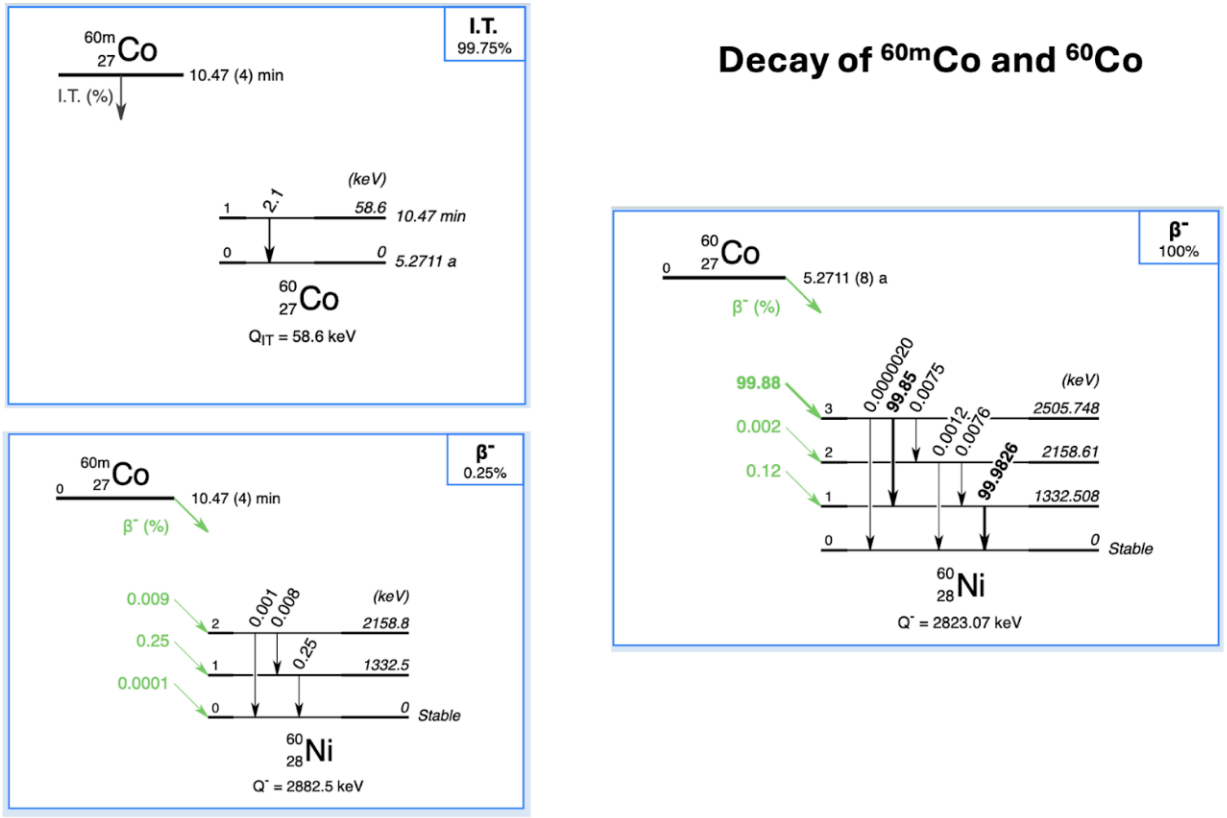

Figure A9.1. Decay scheme of ^{60}Co and its isomeric state ^{60m}Co.
(http://www.lnhb.fr/Laraweb/index.php)

Cobalt in thermal neutron flux

Bombarding ^{59}Co atoms with slow neutrons, the following reactions occur:

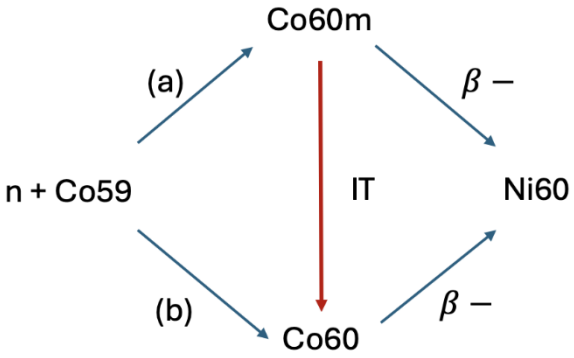

Figure A9.2. Production of ^{60}Co. ENSDF probabilities for the branches are: (a) = 48 % and (b) = 52 %.

NIST web calculator can be used to estimate the activities of ^{60m}Co and ^{60}Co in the neutron exposure of a small amount of cobalt (Table A9.1).

				Activity (µCi) above 5.0000e-4 µCi				
element	reaction	product	half life	0 hrs	1 hr	24 hrs	15 days	1 yrs
Co-59	act	Co-60m+	10.5 m	5.7029e+3	1.0862e+2	---	---	---
Co-59	act	Co-60	5.272 y	4.3072e-2	4.3071e-2	4.3056e-2	4.2839e-2	3.7762e-2
total activity				5.7030e+3	1.0867e+2	4.3056e-2	4.2839e-2	3.7762e-2

Table A9.1. Activation of 1 g of ^{59}Co in neutron irradiation with flux of 10^{12} n/cm2/s for 1 s (NIST).

Data in Table A9.1 allow to calculate the initial number of nuclides produced: NIST nuclide ratio = N(^{60m}Co) / N(^{60}Co) = 0.5. This ratio should be near 1, based on ENSDF data (see Figure A9.2).

Geant4 analyses

Our Geant4 analysis results are handled by counting nuclides in the generated xml result file. More precisely, a tag *<process>RadioactiveDecay</process>* is searched and then the number of nuclei attached is counted. The result can look like this:

^{60}Co 40351
^{60}Ni[2505.766] 40305
^{60}Ni 40351
^{60}Ni[1332.518] 46

where the bare nuclide name refers to the number of nuclides decayed to the ground state and the nuclide name and energy in brackets (keV) refer to the number of populated isomeric states. Note that the ratio 46/40351 = 0.11%, which is about half from the ^{60m}Co branching yield of 0.25% for the 1332.5 keV state.

The number 40351 above refers to the sum of ^{60m}Co and ^{60}Co nuclides. Namely, in the postprocessing of the xml files produced by Geant4, the time stamp of interaction events is omitted, and simply the total number of ^{60}Co nuclides is counted. Therefore, for the radiation exposure analysis during the first hours after the blast, the number of ^{60m}Co and ^{60}Co nuclides should be calculated from a model taking into account the true process of formation of these two nuclides.

Decay of ^{60m}Co to ^{60}Co.

The decay of nuclide A to nuclide B, which is also radioactive, is described as

$$N_A = N_{A0} e^{-\lambda_A t}$$

$$N_B(t) = N_{B0} e^{-\lambda_B t} + N_{A0} b \frac{\lambda_A}{\lambda_B - \lambda_A} \left[e^{-\lambda_A t} - e^{-\lambda_B t} \right]$$

where

N_{A0} and N_{B0} are initial number of atoms A and B
λ_A and λ_B are decay constants
b branching ratio from A to b

When the time behaviour of the atoms is known, it is easy to calculate the activities of the nuclides involved. Figure A9.3 shows the result for ^{60m}Co and ^{60}Co assuming that at time zero there are equal number of ^{60m}Co and ^{60}Co atoms. The time frame of ^{60m} Co domination is three hours: the activities of the two nuclides are the same at t = 178 min (see Figure A9.1). However, from the radiological point of view it is more relevant to compare the emission rate of 1332.5 keV photons. These curves cross each other at t = 88 min.

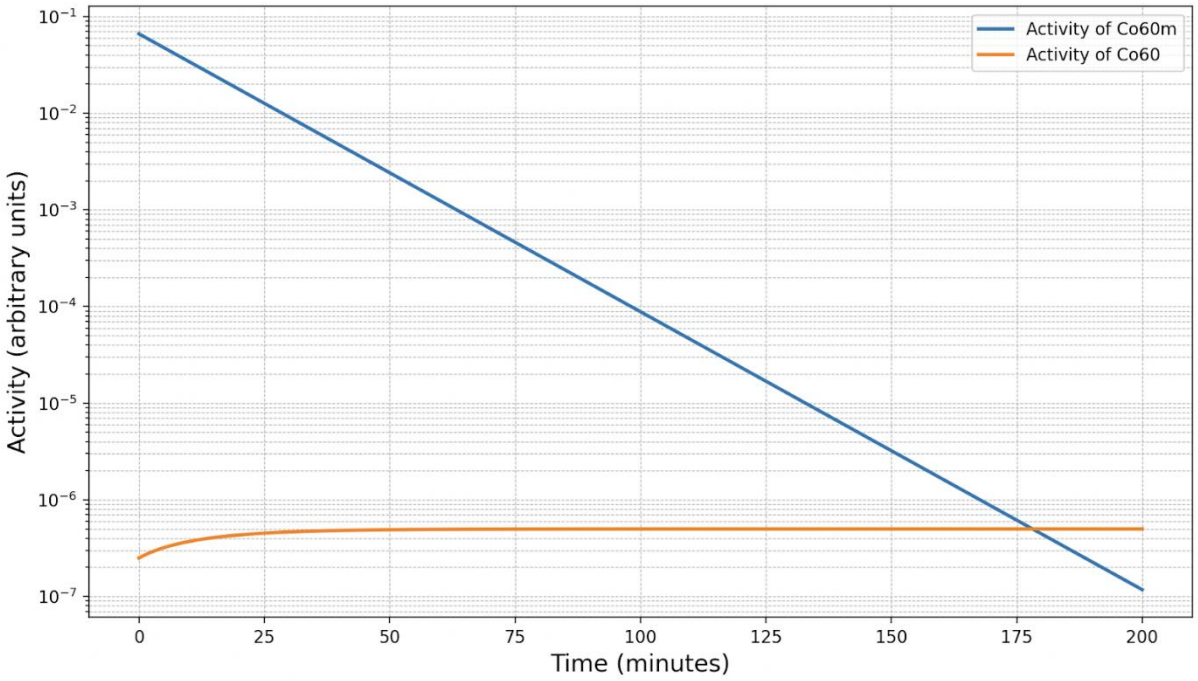

Figure A9.3. Activity of ^{60m}Co and ^{60}Co assuming equal number of atoms at time zero.

Summary on ^{60m}Co

Irradiating cobalt in a thermal neutron flux creates about equal number of ^{60m}Co and ^{60}Co nuclides. The commonly used thermal neutron cross-section of cobalt is 37 barns. This is the total cross-section, including production of ^{60m}Co and ^{60}Co. The total cross-section is valid for long-term analyses of ^{60}Co. Due to short half-life of 10.47 min, ^{60m}Co emits initially much more photons than ^{60}Co with half-life of 5.27 y. ^{60m}Co is dominating the radiation exposure during the first 1.5 hours emitting 1332.5 keV (0.0025 %) and 58.6 keV (2.07 %) photons.

Bibliographic Data Sheet **NKS-513**

Title	Electric Vehicle Batteries as Components of a Post Nuclear Detonation Radiological Environment (EVNUDET)
Author(s)	Harri Toivonen[1], Mark Dowdall[2], Sakari Ihantola[3], Hannes Vainionpaa[4], Gísli Jónsson[5], Pernille Ahlmann Jensen[5], Mikko Voutilainen[6], Kari Perajarvi[6,] Henrik Ramebäck[7]
Affiliation(s)	[1]HT Nuclear Oy, 05880 Hyvinkää, Finland, [2]Norwegian Radiation and Nuclear Safety Authority, 1361, Østerås, Norway, [3]Radis Technologies Oy, Finland, [4]Neutrongate Ltd., Sepänkatu 5H, Riihimäki, Finland, [5]Icelandic Radiation safety Authority, 105 Reykjavík, Iceland, [6]Radiation and Nuclear Safety Authority, 01370 Vantaa, Finland, [7]Swedish Defence Research Agency (FOI), 164 90 Stockholm
ISBN	978-87-7893-613-4
Date	April 2026
Project	NKS-B / AFT/B(25)6
No. of pages	70
No. of tables	41
No. of illustrations	33
No. of references	7

Abstract

EVNUDET focused on assessing radiological consequences of neutron activation in modern EV batteries and surrounding materials following a nuclear detonation. The study integrated Geant4 neutron-transport simulations, analytical activation calculations, and targeted irradiation experiments to validate models and quantify activation products, dose rates, and environmental impacts. Simulations assumed a thermal neutron fluence of 10^{12} n/cm². Activation is highly chemistry-dependent: NMC-811 and NCA chemistries produce substantial short-lived gamma-emitting isotopes, notably ^{56}Mn and ^{64}Cu, while long-lived isotopes such as ^{60}Co and ^{59}Fe occur at much lower activities. LFP batteries, lacking cobalt and nickel, generate minimal gamma activation but form ^{32}P, a strong beta emitter and the most significant long-term nuclide for this chemistry. Total induced activity in NMC/NCA packs reaches ~10^{9}–10^{10} Bq, whereas LFP packs are one to two orders of magnitude lower. Dose rates near activated packs are transient and localized: NMC/NCA surfaces may exhibit tens of mSv/h immediately post-exposure, while LFP remains far lower; at one meter, even high-cobalt chemistries typically fall below a few mSv/h. Activation of sodium-bearing soils and pavement dominates the radiation field in post-detonation environments. EV batteries can create localized short-lived gamma radiation fields, increasing exposure near the vehicle, but their overall contribution is

minor compared to widespread activation of urban materials. Importantly, outside the vehicle, batteries do not present persistent radiological hazards.

Key words Neutron activation, nuclear detonation, electric vehicle battery, dose rates

---

Available on request from the NKS Secretariat, P.O.Box 49, DK-4000 Roskilde, Denmark.
Phone (+45) 4677 4041, e-mail nks@nks.org, www.nks.org